GOLD NANOROD-BASED SHAPE-SHIFTING PROBE FOR THE DETECTION OF HUMAN TELOMERIC G-QUADRUPLEX DNA STRUCTURE

A THESIS SUBMITTED TO
THE GRADUATE SCHOOL OF NATURAL AND APPLIED SCIENCES
OF
MIDDLE EAST TECHNICAL UNIVERSITY

BY

SELİN ÖZKAN

IN PARTIAL FULFILLMENT OF THE REQUIREMENTS
FOR
THE DEGREE OF MASTER OF SCIENCE
IN
CHEMISTRY

JANUARY 2024

Approval of the thesis:

GOLD NANOROD-BASED SHAPE-SHIFTING PROBE FOR THE DETECTION OF HUMAN TELOMERIC G-QUADRUPLEX DNA STRUCTURE

submitted by **Selin Özkan** in partial fulfillment of the requirements for the degree of **Master of Science** i**n Chemistry, Middle East Technical University** by,

Prof. Dr. Halil Kalıpçılar
Dean, **Graduate School of Natural and Applied Sciences** _____

Prof. Dr. Özdemir Doğan
Head of the Department, **Chemistry** _____

Assoc. Prof. Dr. Özgül Persil Çetinkol
Supervisor, **Chemistry, METU** _____

Examining Committee Members:

Prof. Dr. Emren Nalbant
Chemistry, METU _____

Assoc. Prof. Dr. Özgül Persil Çetinkol
Chemistry, METU _____

Assoc. Prof. Dr. Ezel Boyacı
Chemistry, METU _____

Prof. Dr. Mesut Muyan
Biology, METU _____

Assoc. Prof. Dr. Urartu Özgür Şafak Şeker
Materials Science and Nanotechnology, Bilkent University _____

Date: 17.01.2024

I hereby declare that all information in this document has been obtained and presented in accordance with academic rules and ethical conduct. I also declare that, as required by these rules and conduct, I have fully cited and referenced all material and results that are not original to this work.

Name Last name : Selin Özkan

Signature :

ABSTRACT

GOLD NANOROD-BASED SHAPE-SHIFTING PROBE FOR THE DETECTION OF HUMAN TELOMERIC G-QUADRUPLEX DNA STRUCTURE

Özkan, Selin
Master of Science, Chemistry
Assoc. Prof. Dr. Özgül Persil Çetinkol

January 2024, 134 pages

Colorimetric detection methods became one of the indispensable tools in biomedical research since they offer simple, rapid, visual, and often cost-effective means to identify specific biomolecular interactions. In this thesis, a novel colorimetric detection platform using gold nanorods (GNRs) for the detection of human telomeric G-quadruplex (Tel24 G4) DNA was introduced. The detection of Tel24 G4 is important due to the involvement of human telomeric DNA in vital cellular processes.

The unique properties of longitudinal and transverse localized surface plasmon resonance (LSPR) exhibited by unmodified GNRs in cetyltrimethylammonium bromide (CTAB) solution serve as the foundation of the developed platform. Changes observed in the intensity and location of the longitudinal and transverse LSPR peaks of GNRs with increasing concentration of Tel24 G4 DNA suggested the aggregation and the etching as plausible mechanisms.

Under the optimum conditions ([CTAB]=0.01 M, [HCl]=28 mM, 10 min incubation at 60℃), a linear dynamic range of 0.371 to 0.909 μM, with a detection limit of approximately 0.03 μM was determined. The platform was found to be highly specific to Tel24 G4 upon evaluation of its response to diverse oligonucleotide structures, encompassing other available G4 DNA configurations, single, double, and triple-stranded oligonucleotides. In brief, the developed platform has proven to be highly

specific and selective to Tel24 G4 in addition to its simplicity, rapidity, and cost-effectiveness. We believe that the research conducted within this thesis not only advances the application potential of GNRs but also paves the way for their integration into the field of nucleic acid detection.

Keywords: Gold nanorods, Probe, Human telomeric DNA, G-quadruplex DNA, Detection

ÖZ

İNSAN TELOMERİK G-QUADRUPLEX DNA YAPISININ TESPİTİ İÇİN ALTIN NANOROD TABANLI ŞEKİL DEĞİŞTİRME PROBU

Özkan, Selin
Yüksek Lisans, Kimya
Tez Yöneticisi: Doç. Dr. Özgül Persil Çetinkol

Ocak 2024, 134 sayfa

Kolorimetrik tespit yöntemleri, spesifik biyomoleküler etkileşimlerini tanımlamak için basit, hızlı, görsel ve genellikle uygun maliyetli olduklarından biyomedikal araştırmalarda vazgeçilmez araçlardan biri haline gelmiştir. Bu tezde, insan telomerik G-dörtlü (Tel24 G4) DNA'sının tespiti için altın nanoçubuklar (GNR'ler) kullanan yeni bir kolorimetrik tespit platformu sunulmaktadır. Tel24 G4'ün tespiti, insan temolerik DNA'sının hayati hücresel süreçlere dahil olması nedeniyle önemlidir.

Setiltrimetilamonyum bromür (CTAB) çözeltisi içindeki değiştirilmemiş GNR'ler tarafından sergilenen uzunlamasına ve enine lokalize yüzey plazmon rezonansının (LSPR) benzersiz özellikleri, geliştirilen platformun temelini oluşturmaktadır. Artan Tel24 G4 DNA derişimiyle birlikte GNR'lerin uzunlamasına ve enine LSPR piklerinin intensitesinde ve konumunda gözlemlenen değişiklikler, toplanmanın ve aşındırmanın olası mekanizmalar olduğunu öne sürmüştür.

Optimum koşullar altında ([CTAB]=0,01 M, [HCl]=28 mM, 60°C'de 10 dakikalık inkübasyon), yaklaşık 0,03 μM tespit limitiyle 0,371 ile 0,909 μM doğrusal dinamik aralık belirlenmiştir. Platformun, diğer mevcut G4 DNA konfigürasyonlarını, tek, çift ve üç sarmallı oligonükleotidleri kapsayan çeşitli oligonükleotid yapılarına verdiği yanıtın değerlendirilmesi üzerine, Tel24 G4'e oldukça spesifik olduğu belirlenmiştir.

Kısaca geliştirilen platformun basitliği, hızlılığı ve uygun maliyetli olmasının yanı sıra Tel24 G4'e son derece spesifik ve seçici olduğu da tespit edilmiştir. Bu tez kapsamında yürütülen araştırmanın yalnızca GNR'lerin uygulama potansiyelini geliştirmekle kalmayıp aynı zamanda onların nükleik asit tespiti alanına entegrasyonunun da önünü açtığına inanıyoruz.

Anahtar Kelimeler: Altın nanoçubuklar, Prob, İnsan telomerik DNA'sı, G-dörtlü DNA, Tespit

To my friends and family and husband...

ACKNOWLEDGMENTS

I would like to express my deepest gratitude to Assoc. Prof. Dr. Özgül Persil Çetinkol for her guidance, advice, criticism, and insight throughout the research.

This endeavor would not have been possible without Assoc. Prof. Dr. Merhrdad Forough. I thank him for his guidance, suggestions, comments, understanding, patience, and being a wonderful friend along with tutorship.

I could not have undertaken this journey without the support of my friends, Zeynep İrem Bulut, Gamze Buket Çetin and Merve İrem Tokgöz. Additionally, I am extremely grateful to my best friend and husband Kamil Emre Özkan for his patience and being always there for me. Many thanks should also go to my parents for their moral and material support throughout this experience.

I would like to thank my committee members, Prof. Dr. Emren Nalbant, Assoc. Prof. Dr. Ezel Boyacı, Prof. Dr. Mesut Muyan, Assoc. Prof. Dr. Urartu Özgür Şafak Şeker for their valuable presence at my thesis defense and their valuable feedback.

I am also grateful to Prof. Dr. İrem Erel Göktepe and her group members for their help in using Zetasizer Nano-ZS equipment for DLS and Zeta potential analyses.

I would like to thank METU Central Laboratory for CTEM analysis.

I'd like to acknowledge the Department of Chemistry and its employees for their kind assistance during the project as well as for providing an environment and infrastructure that allowed me to conduct research.

This work has been supported by Middle East Technical University Scientific Research Projects Coordination Unit under grant number TEZ-YL-103-2023-11348.

TABLE OF CONTENTS

ABSTRACT v
ÖZ vii
ACKNOWLEDGMENTS x
TABLE OF CONTENTS xi
LIST OF TABLES xiv
LIST OF FIGURES xv
LIST OF ABBREVIATIONS xxi
CHAPTERS
INTRODUCTION 1
1.1. Sensors 1
1.1.1. Biosensor 2
1.1.1.1. Nanobiosensor 4
1.2. Gold Nanorods 7
1.2.1. Synthesis of GNRs 8
1.2.1.1. Template Method 8
1.2.1.2. Electrochemical Method 10
1.2.1.3. Seed-mediated Synthesis 11
1.2.1.4. Other Methods 15
1.2.2. Properties and Applications of GNRs 16
1.2.2.1. Optical Properties 16
1.2.2.1.1 LSPR 16
1.2.2.2. Cytotoxicity and Biocompatibility of CTAB-coated GNRs 21
1.2.3. GNRs as Biosensor 24
1.2.3.1. LSPR-based GNR Biosensors 24
1.2.3.1.1. Assembly-based Biosensor 25

1.2.3.1.1.1. End-to-end Assembly 26
1.2.3.1.1.2. Side-by-side Assembly 26
1.2.3.1.2. Morphology Change-based Biosensor 27
1.2.3.1.1.1. Growth-based Biosensor 27
1.2.3.1.1.2. Etching-based Biosensor 28
1.2.3.1.1.2.1. Direct Etching-based Biosensor 29
1.2.3.1.1.2.2. Complex-promoted Etching-based Biosensor 30
1.2.3.1.1.2.3. Intermediate-mediated Etching-based Biosensor 31
1.2.3.1.1.2.3.1. Halide Ions-mediated Biosensor 32
1.2.3.1.1.2.3.2. Fenton and Fenton-like Reactions-mediated Biosensor 34
1.2.3.1.1.2.3.3. Mercury-mediated Etching-based Biosensor 35
1.3. Nucleic Acid Detection Platforms 36
1.3.1. Nucleic acids 36
1.3.1.1. Structures of DNA 37
1.3.1.1.1. G-quadruplexes 38
1.3.1.1.1.1. Telomeric G-quadruplexes 40
1.3.2. Physiological Importance of Telomeric G4s and Their Detection 42
1.3.3. Optical Detection Platforms Telomeric DNA and Telomerase Activity Detection 45
1.3.3.1. Fluorometric Detection Platforms 45
1.3.3.2. Colorimetric Detection Platforms 47
1.4. Aim of the Thesis 49
MATERIALS AND METHODS 51
2.1. Reagents and Chemicals 51
2.2. Instrumentation 52
2.3. Synthesis of GNRs 53
2.4. Preparation and Characterization of Nucleic Acid Solutions 54
2.5. Colorimetric Detection of Tel24 55
RESULTS AND DISCUSSION 57
3.1. Colorimetric Detection of Tel24 57
3.2. Characterization 58

3.3. Optimization of the Detection Platform 65
3.4. Selectivity 68
3.5. Sensitivity 70
3.6. Proposed Mechanism 71
CONCLUSION 77
REFERENCES 81
APPENDICIES 117
A. Reduction Reactions of Gold 117
A1. Reaction of Seed Solution 117
A2. Reactions of Growth Solution 117
B. DLS Experiment Analyses 118
C. Thermal Denaturation Studies 121
D. Circular Dichroism Studies 127
E. UV-Vis Spectra 131

LIST OF TABLES

TABLES

Table 1. Fluorometric detection platforms for human telomeric DNA and telomerase activity. 46
Table 2. Previously reported colorimetric detection platforms for human telomeric DNA 48
Table 3. Previously reported colorimetric detection platforms for human telomeric DNA and telomerase activity. 48
Table 4. Sequences used in this study and their extinction coefficients. 51
Table 5. Results of DLS and Zeta potential measurements of 0, 6 and 10 min of incubations..... 63
Table 6. Melting temperatures of several oligonucleotides. 74
Table 7. Wavelengths of maxima and minima peaks and topologies of several oligonucleotides according to CD studies. 74
Table B 1. Size distribution of GNRs by intensity of 0 min, 6 min and 10 min of incubation under optimized conditions..... 120
Table C 1. Melting temperatures of Tel24, Tel24+HCl and Tel24+HCl+CTAB. ... 122

LIST OF FIGURES

FIGURES

Figure 1. Classification of sensors [4]. 2
Figure 2. Schematic representation of a biosensor. Adopted and modified from [7] reproduced with permission from Portland Press. 4
Figure 3. Schematic representation of SPR of metal nanoparticles [57]. 8
Figure 4. Schematic diagram GNRs template synthetic methods [70]. 9
Figure 5. Schematic diagram of electrochemical synthesis [70]. 10
Figure 6. Idealized three-dimensional morphology with {111} end faces and {100} side faces. The common five-fold axis of elongation is [110] [84]. 15
Figure 7. (A) Schematic illustration of LSPR excitation for GNRs and (B) LSPR absorption bands of GNRs. Reprinted from [43] with permission form Elsevier. (C) Change in the LSPR wavelength of GNRs in accordance with their aspect ratios and (D) Color change of GNR solutions varying with aspect ratios [97]. 18
Figure 8. (A) Simulated LSPR absorption spectra of GNRs with a range of aspect ratios in a medium with a fixed dielectric constant (inset: peak wavelength of longitudinal plasmon band increases linearly with aspect ratio of GNRs); (B) Simulated LSPR absorption spectra of GNRs with a constant aspect ratio in the medium with a variable dielectric constant (inset: peak wavelength of LPB increases linearly with dielectric constant of the surrounding medium). Reprinted with permission from [101]. Copyright 1999 American Chemical Society. 20
Figure 9. An illustration of several common techniques for functionalizing and detoxifying CTAB-GNRs [123]. 23
Figure 10. Schematic representation of (A) side-by-side and (B) end-to-end assembly of GNRs. Adopted from [146] with permission RSC Publishing. 25
Figure 11. Schematic illustration of direct etching of GNRs. Reprinted from [168] with permission form Elsevier. 30
Figure 12. Schematic representation of complex-promoted etching-based sensors. Reprinted from [168] with permission form Elsevier. 31

Figure 13. Diagrammatic representation of different approaches of development of biosensors based on intermediate-mediated etching of GNRs. Reprinted from [168] with permission form Elsevier. 32
Figure 14. Structural unit of nucleic acids and nitrogenous bases. Reprinted from [248] with permission John Wiley and Sons. 37
Figure 15. Different types of non-B DNAs (A) G4, (B) H-DNA, (C) Z-DNA, (D) Cruciform, (E) Slipped strands, (F) A-tract bending. Reprinted from [261] with permission Oxford University Press..... 38
Figure 16. (A) Structure of a G-quartet, (B) different G4 topologies, where M^+ is a monovalent cation [269]..... 39
Figure 17. UV-Vis absorption spectra of GNRs probe (black line), GNRs + HCl (green dotted line), GNRs + Tel24 (blue dotted line), GNRs + Tel24+ HCl (reaction mixture upon the addition of Tel24 in the presence of HCl after 10 min incubation (red line)); Experimental conditions: [HCl]=28 mM, [Tel24]=0.64 μM, Temperature: 60°C. Inset: The digital photographs of the step-by-step color change of GNRs after the addition of Tel24 under the optimized conditions. (A): Before incubation, (B): 6 min of incubation, (C): 10 min of incubation. 58
Figure 18. TEM micrographs of GNRs (A, B and C), GNRs after 6 min (D, E and F) and 10 (G, H and I) min of incubation at 60°C after the addition of Tel24 and HCl at different magnifications. Experimental conditions: [HCl]=28 mM, [Tel24]=0.64 μM. 61
Figure 19. Dynamic Light Scattering and Zeta Potential measurements of GNRs (A and B), GNRs after 6 min of incubation (C and D) and10 min of incubation (E and F) at 60°C after the addition of Tel24 and HCl. Experimental conditions: [HCl]=28 mM, [Tel24]=0.64 μM. 62
Figure 20. The effect of (A): CTAB concentration, (B): HCl concentration, (C): incubation temperature, and (D): reaction time on the response of GNRs to Tel24. The error bars indicate SD (n= 3). 67
Figure 21. (A) Selectivity studies for unmodified GNRs probe based on the addition of each nucleic acid structure. (B) Bar graph depicting the peak shift vs. various under-examined nucleic acid structures for selectivity studies of unmodified GNRs probe,

based on the addition of each nucleic acid structure under the specified experimental conditions: [CTAB]=0.01 M, [HCl]=28 mM, [DNA]=0.64 μM, Temperature: 60°C, Time: 10 min. The error bars indicate SD (n= 3). 69
Figure 22. (A): UV-Vis absorption spectra of GNRs with increasing concentration of Tel24 under the optimized conditions. (B): Plot of peak shift vs. Tel24 concentration, Experimental conditions: [CTAB]=0.01 M, [HCl]=28 mM, Temperature: 60°C. The error bars indicate SD (n= 3). 71
Figure B 1. Size distribution of GNRs by intensity. (Same sample recorded 3 times .) A: the first peak of Record 1, B: the second peak of Record 2, C: the first peak of Record 2, D: the second peak of Record 2, E: the first peak of Record 3, F: the second peak of Record 3. 118
Figure B 2. Size distribution of GNRs by intensity after 6 min incubation under optimized conditions. (Same sample recorded 3 times.) A: the first peak of Record 1, B: the second peak of Record 2, C: the first peak of Record 2, D: the second peak of Record 2, E: the first peak of Record 3, F: the second peak of Record 3. 119
Figure B 3. Size distribution of GNRs by intensity after 10 min incubation under optimized conditions. (Same sample recorded 3 times.) A: the first peak of Record 1, B: the second peak of Record 2, C: the first peak of Record 2, D: the second peak of Record 2, E: the first peak of Record 3, F: the second peak of Record 3. 120
Figure C 1. UV-Vis thermal denaturation profile of 2.0 μM of Tel24. 121
Figure C 2. UV-Vis thermal denaturation profile of 2.0 μM of Tel24 in the presence of 28 mM HCl. 121
Figure C 3. UV-Vis thermal denaturation profile of 2.0 μM of Tel24 in the presence of 28 mM HCl and 0.01 M CTAB. 122
Figure C 4. UV-Vis thermal denaturation profile of 2.0 μM of VEGF. 123
Figure C 5. UV-Vis thermal denaturation profile of 2.0 μM of VEGF in the presence of 28 mM HCl and 0.01 M CTAB. 123
Figure C 6. UV-Vis thermal denaturation profile of 2.0 μM of Tel24m1. 124
Figure C 7. UV-Vis thermal denaturation profile of 2.0 μM of Tel24m1 in the presence of 28 mM HCl and 0.01 M CTAB. 124
Figure C 8. UV-Vis thermal denaturation profile of 2.0 μM of Pu_{22} 125

Figure C 9. UV-Vis thermal denaturation profile of 2.0 μM of Pu_{22} in the presence of 28 mM HCl and 0.01 M CTAB. 125
Figure C 10. UV-Vis thermal denaturation profile of 2.0 μM of Tel24m1. 126
Figure C 11. UV-Vis thermal denaturation profile of 2.0 μM of Tel24m3 in the presence of 28 mM HCl and 0.01 M CTAB. 126
Figure D 1. CD spectra of Tel24, Tel24 + HCl and Tel24 + HCl + CTAB. Experimental conditions: [Tel24]=2.0 μM, [HCl]=28 mM, [CTAB]=0.01 M. 127
Figure D 2. CD spectra of Tel24 at 15°C, 60°C and 80°C. 127
Figure D 3. CD spectra of 2 μM Tel24 in the presence of HCl and CTAB at 15°C, 60°C and 80°C. Experimental conditions: [Tel24]=2.0 μM, [HCl]=28 mM, [CTAB]=0.01 M. 128
Figure D 4. CD spectra of VEGF, VEGF + HCl and VEGF + HCl + CTAB. Experimental conditions: [VEGF]=2.0 μM, [HCl]=28 mM, [CTAB]=0.01 M. 128
Figure D 5. CD spectra of Tel24m1, Tel24m1 + HCl and Tel24m1 + HCl + CTAB. Experimental conditions: [Tel24m1]=2.0 μM, [HCl]=28 mM, [CTAB]=0.01 M and Measurement temperature=15°C. 129
Figure D 6. CD spectra of Pu_{22}, Pu_{22} + HCl and Pu_{22} + HCl + CTAB. Experimental conditions: [Pu_{22}]=2.0 μM, [HCl]=28 mM, [CTAB]=0.01 M and Measurement temperature=15°C. 129
Figure D 7. CD spectra of Tel24m3, Tel24m3 + HCl and Tel24m3 + HCl + CTAB. Experimental conditions: [Tel24m3]=2.0 μM, [HCl]=28 mM, [CTAB]=0.01 M and Measurement temperature=15°C. 130
Figure E 1. UV-Vis absorption spectra of the GNRs upon the addition of Tel24 with different concentrations of CTAB (0 – 0.14 M). Experimental conditions: [HCl]=28 mM, [Tel24]=0.64 μM, Temperature: 60°C, after 10 min of mixing. 131
Figure E 2. UV-Vis absorption spectra of the GNRs upon the addition of Tel24 with different concentrations of HCl (0 – 33 mM). Experimental conditions: [CTAB]=0.01 M, [Tel24]=0.64 μM, Temperature: 60°C, after 10 min of mixing. 132
Figure E 3. UV-Vis absorption spectra of the GNRs upon the addition of Tel24 at different temperatures (30.0-80.0°C) Experimental conditions: [Tel24]=0.64 μM, after 10 min. 133

Figure E 4. UV-Vis absorption spectra of the GNRs upon the addition of the target analyte for 0-60 min. Experimental conditions: [CTAB]=0.01 M, [HCl]=28 mM, [Tel24]=0.64 μM, Temperature: 60°C. 134

LIST OF SCHEMES

SCHEMES

Scheme 1. Schematic representation of the synthesis of GNRs. 54

LIST OF ABBREVIATIONS

ABBREVIATIONS

AA	L-Ascorbic Acid
BDAC	Benzyldimethylhexadecylammoniumchloride
CD	Circular Dichroism
CN^-	Cyanide
CNTs	Carbon Nanotubes
CTA^+	Cetyltrimethylammonium Ion
CTAB	Cetyltrimethylammonium Bromide
CTAC	Cetyltrimethylammonium Chloride
CTEM	High Contrast Transmission Electron Microscopy
DI	Deionized
DLS	Dynamic Light Scattering
DNA	Deoxyribonucleic Acid
DTAB	Dodecyltrimethylammonium Bromide
EXPAR	Exponential Amplification Reaction Assays
GNPs	Gold Nanoparticles
GNRs	Gold Nanorods
HRTEM	High Resolution Transmission Electron Microscopy
LDR	Linear Dynamic Range
LOD	Limit of Detection
LOQ	Limit of Quantitation

LSPR	Localized Surface Plasmon Resonance
MNP	Metal Nanoparticles
NWs	Nanowires
OH•	Hydroxyl Radical
RM	Reverse Micelles
RNA	Ribonucleic Acid
SD	Standard Deviation
SEF	Surface-Enhanced Fluorescence
SERS	Surface-Enhanced Raman Spectroscopy
SH	Thiol
SPR	Surface Plasmon Resonance
TEM	Transmission Electron Microscopy
TER	Telomerase RNA
TERT	Telomerase Reverse Transcriptase
TMB	3,3’,5,5’-Tetramethylbenzidine
UV-Vis	Ultraviolet-Visible

CHAPTER 1

INTRODUCTION

1.1. Sensors

A sensor is a device that transforms physical quantity inputs into functionally related outputs, typically in the form of electrical or optical signals that may be read or recognized by electronic devices or by humans [1]. It is a tool that transforms a signal from a physical phenomenon [2]. Temperature, pH, force, odor, pressure, the presence of particular chemicals, flow, position, and light interactions are just a few examples of the various physical and chemical properties of compounds that can be detected and measured using sensors and the associated interface [1]. A sensor may go through multiple conversion stages between the input and the output before it generates a signal. In the case of a fiber-optic sensor, for example, pressure applied to the sensor first causes the fiber to strain, which consequently causes the fiber's refractive index to deflect, producing an overall alteration in optical transmission and modulation of photon density. The last step is to detect and convert photon flux into electric current [3].

Sensors can be classified into various categories (Figure 1) based on their measurand, output signal, sensor material, physical contact, energy source, comparability, application, specification, and signal conversion [4].

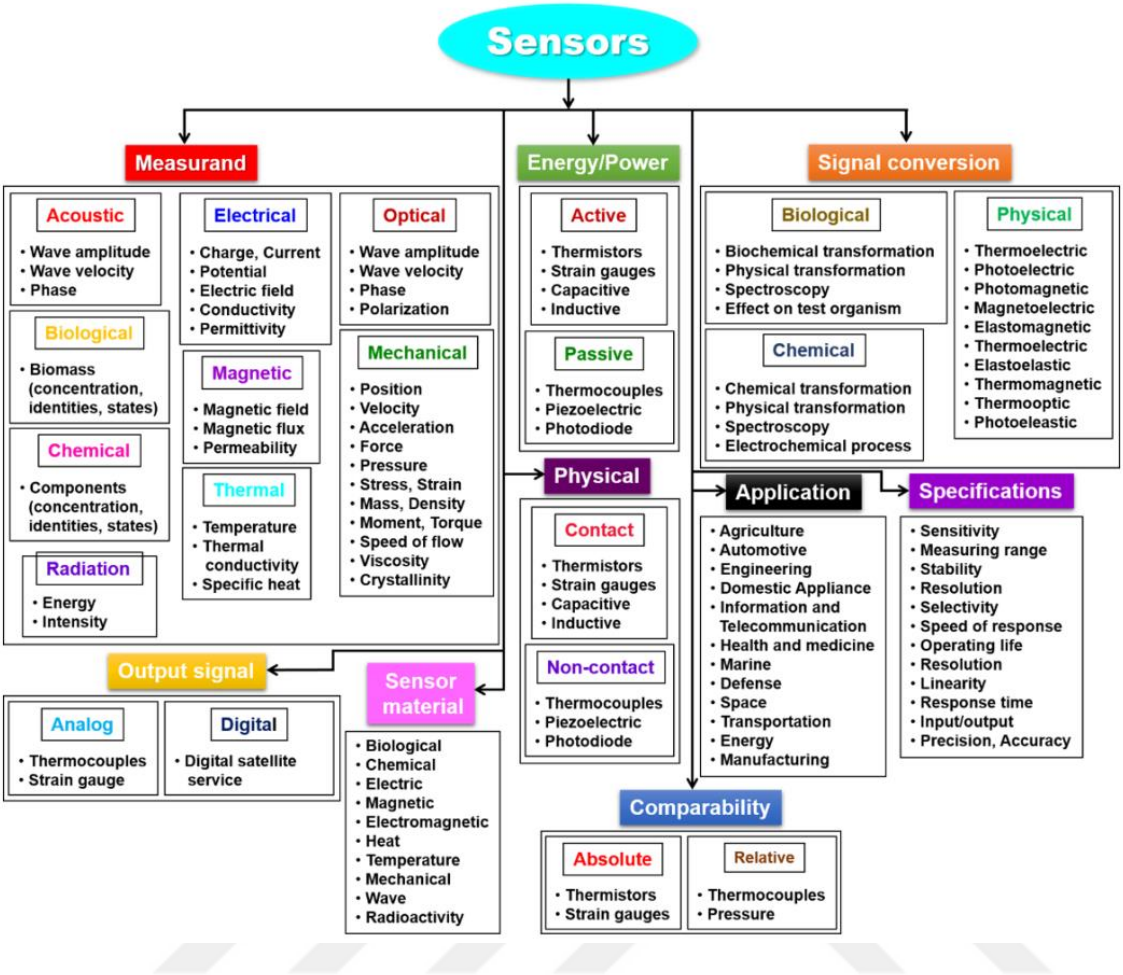


Figure 1. Classification of sensors [4].

A combined receptor-transducer device that can transform a biological reaction into a signal is called a biosensor. Due to numerous applications for biosensors in the last years, including drug delivery, environmental monitoring, water and food quality monitoring, health care, and disease diagnosis, biosensor design and development have gained significant attention of scientists and researchers [4].

1.1.1. Biosensor

A biosensor is a system or probe which incorporates a biological element, like a biomolecule, an enzyme or an antibody, with a sensing component to produce a detectable signal. This device detects the presence of a biological analyte in a biological or chemical reaction via the produced signals corresponding to the concentration of the target biological element [4]. The first biosensor was initially

introduced by Clark and Lyons [5] in 1962. It was a glucose-detecting amperometric oxygen electrochemical sensor that used the enzyme glucose oxidase (GOx) as a recognition element. The word "biosensor" was created as the abbreviation for the so-called "bioselective sensor" that Rechnitz and his colleagues [6] suggested for an arginine selective electrode that utilized living organisms as recognizing components.

Today, biosensors are utilized for various purposes such as disease monitoring, drug discovery, and detection of pollutants, disease-causing microorganisms, and disease markers in physiological fluids (blood, urine, saliva, sweat) [7].

Figure 2 depicts a conventional biosensor, which includes an analyte, a receptor, a transducer, electronics, and a display. The analyte is the substance desired to be detected. The receptor is a molecule, biomolecule, or biological element that recognizes the target analyte specifically. The component that transforms one type of energy into another is called a transducer. The transducer is responsible for converting the biorecognition process into a measurable signal in a biosensor. The majority of transducers generate optical or electrical signals, which are typically proportional to the number of interactions between the analyte and bioreceptor. The transduced signal is processed and prepared for display by electronics. The display frequently consists of a hardware and software combination that generates the biosensor's results in a user-friendly way. Depending on the needs of the end user, the output signal on the display may be numerical, visual, tabular, or an image [7].

These sensors have benefits as excellent selectivity to the target analyte due to bio-recognition, which is the unique interaction of the receptor found in their structure with the target analyte [8].

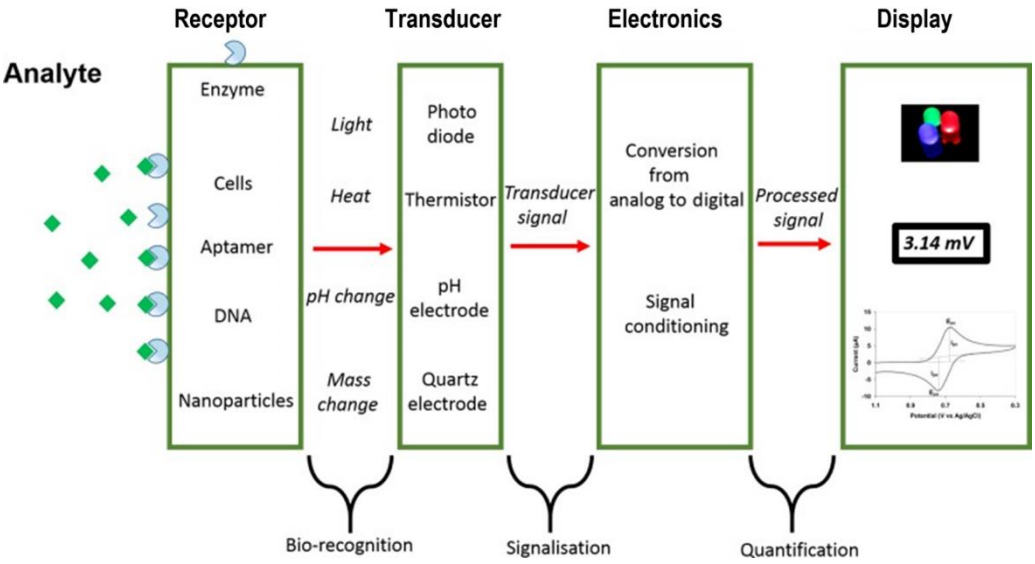


Figure 2. Schematic representation of a biosensor. Adopted and modified from [7] reproduced with permission from Portland Press.

1.1.1.1. Nanobiosensor

A nanobiosensor is a biosensor that consists of a nanomaterial in the range between 1 and 100 nm in size [9]. Numerous benefits of nanobiosensers over conventional biosensors make them an appealing research area. First, the design of nanobiosensors is generally more compact than the conventional biosensors due to the use of nanoscale constituents in their constructions. And their compact design reduces the amount of lab space needed and enables the implanted monitoring. Second, the detection sensitivity of nanobiosensors is frequently higher than the conventional biosensors again due to the use of nanoscale constituents which led to higher surface-to-volume ratio, unique optical and electrical properties. They also generally have an extended range of higher and lower limits of detection that allows the expansion of the working range for the detection. Finally, the production costs of these nanosensors can be reduced by the use of advanced technology, which can reduce the expenses associated with clinical healthcare testing for the detection and diagnosis of illnesses [10].

At the nanoscale, fundamental changes in material behavior can be attributed to two main factors. First, there are the quantum effects, which begin to emerge at very small scales and alter the material's chemical and physical characteristics due to a similarity

between the size of the material and the wavelengths that are being used for its excitation. The extremely high surface-to-volume ratio is the second distinguishing characteristic of materials at the nanoscale. There is no atom that exists away from a surface or an interface of the nanomaterial, and how atoms behave at these higher-energy sites has a big impact on the properties of the materials [11]. For instance, as the size of a metal catalyst decreases, its reactivity increases noticeably. While gold is chemically inert at the macroscopic level, it becomes exceedingly reactive and catalytic at the level of the nanoscale and even melts at lower temperatures. Consequently, material qualities depend on and vary with size, and additionally with composition and structure, at the nanoscale scale [12].

In order to develop enhanced biological signaling and transduction systems, many different types of nanomaterials have been investigated so far based on their electrical and mechanical properties. Nanotubes, nanowires, nanoparticles, and nanorods comprised of nanocrystalline matter are some of these materials that are commonly utilized [13].

Carbon nanotubes (CNTs) are highly advantageous for chemical and biological sensing applications due to their distinctive structure and nanoscale size. Large aspect ratios, outstanding electrical conductivities, a high degree of chemical stability, and fluorescent features are only a few of these characteristics [14]. The use of carbon nanotubes in biosensors has been mainly focused on electrochemical [15], optical [16], and field-effect devices [17]. Purification and functionalization of CNTs with biorecognition components are required in order to make effective use of this nanomaterial's features in the development of biosensors [14]. Several studies have been conducted using CNTs as biosensors to detect xanthine [18], ethanol [19], dopamine and uric acid [20], thrombin [21], heavy metal ions [22], peroxidase activity [23] and DNA [24].

Nanowires (NWs) are another class of nanomaterials that provide innovative and distinctive possibilities for the development of novel bionanosensors. The size of the nanowires is similar to the detected chemical and biological species generally in the range of 10 to 100 nm [25]. As a result, they are great primary transducers to generate

signals and connect with macroscopic equipment. Particularly, the electrical and optical properties of inorganic NWs are very reproducible. Robust emission characteristics of semiconductor nanocrystals and size-tunable shades provide advantages for biological species tagging and optical-based detection. Direct, label-free electrical reading can also be produced by the combination of the tunable conducting capabilities of semiconducting NWs and the capacity to bind analytes on their surface, which is highly attractive for numerous uses. These detectors are designed as field effect transistors, which change their conductivity in response to changes in the electric field or surface potential [26]. So far, nanowire systems have been used to sense many biological analytes including H_2O_2 and cysteine [27], uric acid [28], enzymes [29], RNA [30], protein [31] and, DNA [32].

There are several different types of nanoparticles that have been used in biosensors, including metallic nanoparticles (MNPs), metal oxide nanoparticles, and semiconductor nanoparticles, along with nanodimensional conducting polymers. Because of their distinct features, different types of nanoparticles always have different functions in different detection systems. Typically, electronic wires are made out of metal nanoparticles. While semiconductor nanoparticles are frequently utilized as labels or tracers, metal oxide nanoparticles are commonly used to immobilize biomolecules [33]. Nucleic acids [34], heavy metal ions [35], nucleotide bases [36], glucose [37] and cancer cells [38] are a few examples of analytes that can be detected by nanoparticle-based biosensors.

Nanorods are also utilized as nanobiosensors due to their analyte binding efficiency and specificity [39]. Several metal oxides and noble metals, including CuO [40], ZnO [41], and Au [42], have been used to create nanorods, and each of these materials has unique advantages for detecting particular analytes. Metal oxide nanorods benefit from the metal oxides' electrocatalytic characteristics in combination with the typical high surface-area-to-volume ratio of nanorods [39]. Whereas noble metal nanorods, such as gold nanorods (GNRs), have received special attention for the fabrication of sensitive LSPR biosensors due to their distinctive and remarkable optical characteristics [43]. They are used to detect many biological analytes from antibodies [44], antibiotics [45],

toxins [46] to pathogens [47]. And, within this thesis, GNRs that are explained in detail below, have been utilized in the detection of telomeric DNA.

1.2. Gold Nanorods

GNRs, an essential type of the noble-metal nanoparticles (Au, Ag, Cu), are garnering intense scientific interest for their distinctive features and possible uses that include biosensing [48], photothermal therapy [49], molecular imaging [50], and gene delivery for cancer treatment [51]. GNRs exhibit significantly improved light absorption and Rayleigh scattering due to surface plasmon resonance. GNRs may be considered as elongated gold nanoparticles (GNPs) that have distinct optical characteristics that depend on their size and morphology [52]. In brief, the formation of plasmon resonances on the surface of GNRs, like spherical GNPs and other noble metal nanoparticles, enables them to absorb light of different wavelengths. The intensity and wavelength of these surface plasmon resonances (SPR), which are collective oscillations of the electrons surrounding the nanoparticles, are shape and size-dependent, which is represented in Figure 3. GNRs have an anisotropic form and exhibit transverse localized surface plasmon resonance and longitudinal localized surface plasmon resonance bands that are distinct from one another. As opposed to the longitudinal LSPR, which varies greatly depending on the size and aspect ratio of the nanorods, the transverse LSPR is found at a wavelength of just over 500 nm (explained within section 1.2.2.1.1 in detail) [53].

Since the first discovery of GNRs in 1991, their preparation and characterization have been intensively studied due to their potential applications in optical devices, biochemical sensors, and nanomedicine [54]. Numerous synthesis methods have been developed throughout the last two decades to improve GNRs' yield, aspect ratio, shape, and uniformity [55]. In addition, considerable efforts have been made to investigate the physical and chemical properties of GNRs to develop applications in photonics, electronics, catalysis, and biology [56].

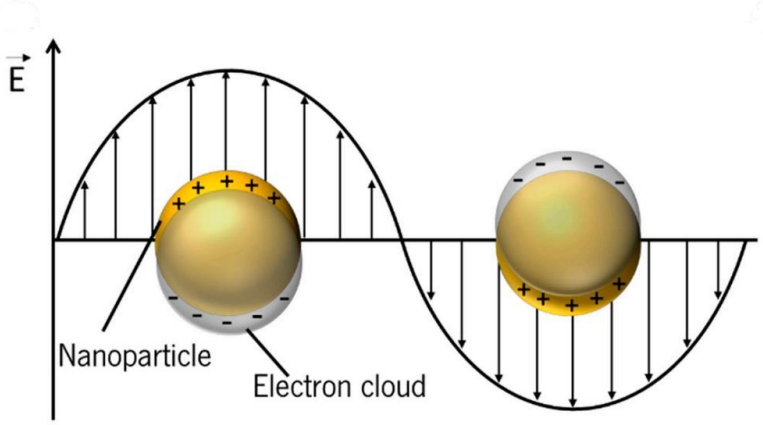


Figure 3. Schematic representation of SPR of metal nanoparticles [57].

1.2.1. Synthesis of GNRs

So far, several studies on the synthesis of GNRs have been reported, including a porous aluminum oxide membrane method [58], an electrochemical method with surfactant molecules as directing agents [59], a seed-mediated growth method using cetyltrimethylammonium bromide (CTAB) [60], photochemical method [61], and so forth. Extensive research has been conducted especially on the seed-mediated route among these techniques [62–65]. However, because the reaction system for particle elongation appears to be quite sophisticated, the mechanism of rod formation is still unknown [56]. A small change in the content of any reactant, such as $AuCl_4$, $AgNO_3$, reducing agents (L-ascorbic acid, $NaBH_4$), surfactant (benzyldimethylhexadecylammoniumchloride (BDAC), dodecyltrimethylammonium bromide (DTAB), CTAB), or seed, was found to lead to a significant alteration in the nanorods' shape/morphology and size. Several publications reported similar syntheses for the preparation of different forms of GNRs [62–65].

1.2.1.1. Template Method

Martin and colleagues were the first to propose the template method to produce GNRs [66–68]. In this approach, gold is electrochemically deposited into the pores of nanoporous polycarbonate or alumina template membranes. The rods can be dispersed into organic solvents by dissolving the appropriate membrane, followed by polymer stabilization. The process works as follows: To form a conductive coating for

electrodeposition, a small quantity of Ag or Cu is sputtered onto the alumina template membrane. This serves as a template for the electrochemical growth of GNRs. Following that, Au is electrodeposited into the alumina nanopores. The alumina membrane and Ag or Cu films are then selectively dissolved in the presence of a polymeric stabilizer such as poly(vinylpyrrolidone). The overall scheme of the template method is illustrated in Figure 4. The rods are then dispersed using sonication or agitation in either water or organic solvents. The amount of Au deposited inside the membrane pores can be used to adjust the length of the nanorods. The pore diameter of the alumina membrane aligns with the diameter of the GNRs produced. Consequently, by changing the pore diameter of the template, GNRs with different diameters can be fabricated. The main limitation of the template method is its yield. The fabrication of rods in the milligram range is difficult because only monolayers of rods are produced. Nevertheless, many fundamental optical effects can be demonstrated by these initial pioneering studies [69].

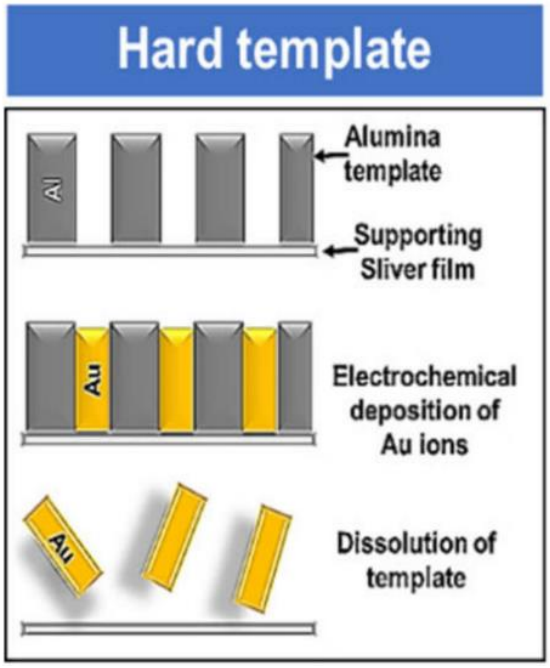


Figure 4. Schematic diagram GNRs template synthetic methods [70].

1.2.1.2. Electrochemical Method

The earliest report of relatively high-quality GNRs synthesis by electrochemical method, which was a pioneer in the most commonly encountered seed-mediated procedure, was described by Wang and colleagues [59,71]. An electrochemical cell with two electrodes is used for the synthesis (Figure 5). The gold plate operates as the anode, while the platinum electrode serves as the cathode. Both of the electrodes are submerged in a solution containing the cationic surfactant CTAB and a small quantity of the more hydrophobic tetradodecylammonium bromide (TDTAB), which favors the evolution of elongated micelles. In this situation, CTAB serves as both an electrolyte and a stabilizer of GNRs, preventing their aggregation. The electrochemical cell also contains acetone and cyclohexane. TDTAB is more easily incorporated into the CTAB micelles as a result of acetone's ability to loosen the micellar frameworks. Enhancing the development of long, rod-like micelles was reported to require cyclohexane usage [72].

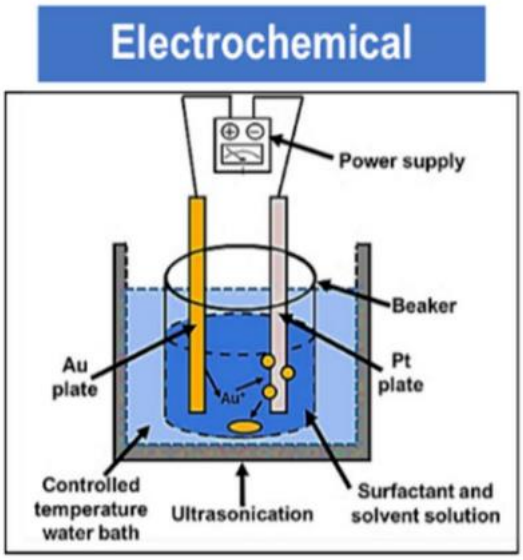


Figure 5. Schematic diagram of electrochemical synthesis [70].

The amount of silver ions present in the electrolytic solution was shown to have an impact on the length of the GNRs that were produced. An electrolytic solution was used to dissolve a silver plate. Silver ions were created as a result of a redox interaction between the surface of the silver plate and gold ions which were created at the anode.

The presence of silver electrodes in the solution affected the length of GNRs. This phenomenon may be explained by the creation of a silver layer on the longitudinal faces of GNRs, which hinders transverse growth [71]. Using this method, nanorods can be produced with aspect ratios ranging from 1 to 7, with rod diameters of roughly 10 nm and a longitudinal plasmon of about 1050 nm. Despite the fact the precise mechanisms are unknown, it is theorized that TDTAB was the rod-directing agent and that rod growth happened on the electrode's surface and sonication liberated the rods into solution [53]. El-Sayed and colleagues [53] used crystallography to identify that the major portion of the rods was single-crystalline and grew in the longitudinal direction, the same structure as that produced by silver-assisted seed-mediated synthesis.

1.2.1.3. Seed-mediated Synthesis

The seed-mediated growth approach is the most common technique for synthesizing colloidal GNRs because of its ease of use, excellent quality and high yield of the synthesized nanorods, simplicity of particle size control, and versatility for structural modifications [54]. Wiesner and Wokaun [73] described the production of the first anisometric gold colloids by introducing gold nuclei into $HAuCl_4$ growth solutions in 1989. The nuclei were produced by reducing $HAuCl_4$ with phosphorus, and GNR growth was triggered by the addition of H_2O_2.

In 2001, Jana et al. [74] developed the currently-in-use approach of seed-mediated chemical growth by adding citrate-capped small gold nanospheres to a bulk $HAuCl_2$ growth solution obtained by reducing $HAuCl_4$ with ascorbic acid in the presence of CTAB surfactant and silver ions. In the presence of MNPs which catalyze the reduction process, ascorbic acid can only reduce gold ions to gold atoms. Another group [75] extended and developed an approach, with a three-step procedure for long rod synthesis with an aspect ratio up to 23, in the absence of silver nitrate. In this procedure, the synthesized GNRs at the first stage are utilized as seeds for the second growth, which are then used as seeds for the third growth. The addition of nitric acid to the third seed growth medium promotes the formation of GNRs with a high aspect ratio, higher monodispersity and yield. Nitric acid not only decreased the pH but also

nitrate ions promoted the formation of GNRs with high aspect ratio. The disadvantage of this technique is that the production of a significant amount of gold nanospheres (which is necessary to separate the rods from the spheres) requires a long centrifugation process [76].

Nikoobakht and El-Sayed [63] modified a procedure in 2003 by replacing sodium citrate in the seed generation process with a stronger stabilizer, CTAB, and silver ions to adjust the aspect ratio of GNRs. This protocol consists of two steps: First, preparation of the seed solution by reduction of $HAuCl_4$ in the presence of CTAB with ice-cold sodium borohydride, $NaBH_4$ reduces Au^{3+} ions to Au^0 [77] (reaction given in Appendix A1); and second, the addition of the seed solution to the Au^+ stock solution prepared by reduction of $HAuCl_4$ with ascorbic acid in the presence of CTAB [63], ascorbic acid reduces Au^{3+} ions to Au^+ ions [78] (corresponding reactions given in Appendix A2). Before seed addition, silver nitrate is added to the gold solution to promote rod growth and regulate the aspect ratio. This approach results in high-yield GNRs (99%) with aspect ratios ranging from 1.5 to 4.5 without the need to reiterate centrifugation steps for nanosphere separation. Simple centrifugation or the addition of sodium sulfide can block the overgrowth. BDAC is added as a cosurfactant, to the initial growth solution to support the development of nanorods with higher aspect ratios. By altering the silver ion concentration in this binary surfactant system, nanorods with aspect ratios up to 10 can be produced. With the Pluronic F-127 co-surfactant system, the aspect ratio can be increased to 20 with acceptable monodispersity. To produce nanorods with a specific aspect ratio, following the first stage of nanorod growth, the gold growth solution can be gradually added to the nanorod solution at a rate of 1.0 mL every 20 min to stimulate continuous rod growth. The fourth addition of growth medium with larger volumes, followed by shape changes from fusiform to 1D rods, have resulted in aspect ratios as high as 70 [63]. In both of the aforementioned methods, the monodispersity, size, and fine shape of the prepared GNRs were reported to be affected by many parameters, including the concentration, size, and structure of the seed, the concentration of ascorbic acid, temperature, pH, the concentration of gold precursor and surfactant, use of other surfactants, additives, solvent(s), and even aging time. Furthermore, the impurity of

CTAB was found to play a crucial role in the growth of nanorods. Due to the presence of impurities, CTAB from different suppliers and catalog numbers was reported to affect not only the nanorods' aspect ratio but also their yield and monodispersity. For instance, iodide contamination has been discovered to selectively attach to the Au {111} facet, and induce the production of GNRs, as an essential shape-giving component [79].

The growth of GNRs has been explained using two different mechanisms. Murphy and coworkers [76,80] hypothesized surfactant-preferential-binding-directed growth based on high-resolution transmission electron microscope (HRTEM) images and selective area electron diffraction (SEAD) analysis, demonstrating the rod structure and numerous parameters impacting the rod formation process. According to HRTEM and electron diffraction patterns, GNRs generated with citrate-capped seeds and no silver ions exhibit pentatetradedral twins morphology. In a pentatwinned structure (Figure 6), the nanorods have side faces of Au {100} or {110} and end faces of Au {111}. They claimed that inherent structural twinning in face centered cubic MNPs leads to symmetrical breakage, resulting in anisotropic nanoparticles. Since the spacing on the gold atom, on the {100} face, is more comparable to the size of the surfactant headgroups than that of the close packaged rod end, the cetyltrimethylammonium ion (CTA^+) headgroup binds preferentially to faceted seed nanoparticles on this face with anisotropic development resulting in nanorods. Meanwhile, Gail and Harmer [81] found twin defect structures on the {110} side surface. This is consistent with the fact that the {110} face has a higher surface energy than the other faces. As a result of CTAB binding's ability to stabilize this face, crystal growth on this side is slowed, and gold is deposited on the end facet, leading to rod growth. The other mechanism is the electric field-controlled growth mechanism described by Pérez-Juste and coworkers [65]. In this mechanism, $AuCl_4^-$ is bound to CTAB micelles and reduced, resulting in the formation of $AuCl_2$–CTAB micelles. The electric double layer between the positively charged seed and the negatively charged $AuCl_2^-$ on the CTAB micelles controls how these complex bonds to the CTAB-capped seed particles. Because collisions occur more rapidly at the tips of the seeds than at the sides, rod-shaped growth is facilitated. The formation of the initial tips of the seed could not be explained

by this mechanism. Previously, the control of silver ions over the aspect ratio was clarified as adsorption of Ag-Br pair to different facets of GNPs which results in restriction of particle growth [74]. According to Nikoobakht and El-Sayed [63], Ag–Br pairings decrease the charge density of bromide ions, which reduces the repulsion of adjacent CTAB headgroups. This repulsive force leads to the elongation of CTAB and consequently rod growth. By analyzing the structural differences between CTAB and citrate-capped seeds, Liu and Guyot-Sionnest [82] investigated the role of silver ions. Their findings revealed that the multiply twinned crystalline citrate-capped seed grows into multiple twinned structures, in particular, into quintuple-twinned while the single-crystalline CTAB-capped seed grows into single-crystalline nanorods with {110} faces on the side and {100} on the flat end. The deposition of gold atoms on the seed surface does not result in a stacking default, therefore the initial seed structures are preserved. Ascorbic acid in an acidic pH cannot convert Ag^+ in the CTAB solution to bulk silver atoms. However, Ag^+ can be reduced to Ag^0 and deposited as a metal monolayer on a metal substrate at a lower potential than bulk reduction, this process is known as underpotential deposition (UPD). Silver deposition on surfaces has a smaller reduction potential than {100} or {111} ends. According to these findings, Liu and Guyot-Sionnest [82] proposed that due to UPD effects, silver deposition on the {110} side of the rods is faster than on the {100} ends, and so the seeds grow into nanorods. Orendorff and Murphy [83] developed a silver UPD mechanism that clearly explains the growth process by combining the UPD, electric-driving-directed, surfactant-preferred binding models, and their quantization analyses of metal contents in silver-assisted nanorod growth. The electric field interactions cause $AuCl_2^-$ on CTAB micelles to diffuse to CTAB-capped seed spheres, and the sphere symmetry is disrupted into different facets, with CTAB preferentially attaching to the {110} facet. Silver ions deposit at a higher rate on the {110} side facet than on the {100} end facet, causing the particle to grow into a rod shape in the [110] direction. The process is limited to producing nanorods no longer than 100 nm due to the complete deposition of silver ions on the {100} end facet, which inhibits particle growth. The fact that silver-assisted nanorods are shorter than those produced without silver ions argues for this mechanism. However, since the end facet of the nanorods is blocked by the

deposition of silver metal, increasing the silver ion concentration above a threshold value cannot further improve the aspect ratio [63].

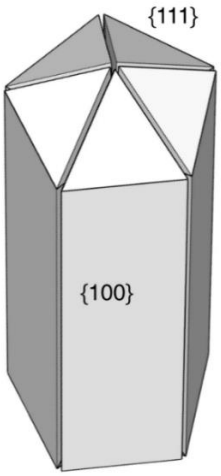


Figure 6. Idealized three-dimensional morphology with {111} end faces and {100} side faces. The common five-fold axis of elongation is [110] [84].

1.2.1.4. Other Methods

A one-step seedless method in which sodium borate is added directly to the growth solution in the presence of silver ions, ascorbic acid, and the surfactant CTAB to induce nucleation and particle growth can also produce GNRs with high yield and desired monodispersity [54,85,86].

X-ray irradiation and proton beam irradiation [87], electrochemical method [55,56], microwave reduction [88], bioreduction [89], and solvothermal reduction [90] are some of the alternative preparation procedures. Despite their lack of popularity, these approaches are valuable contributions to the preparation of colloidal GNRs.

In summary, there are many different methods developed for the synthesis of the GNRs mostly within the last two decades. The choice of the method will depend on the desired properties of GNRs in addition to the ease and the availability of the method. Here, within this thesis study, GNR probes were synthesized using a slightly modified seed-mediated growth method originally proposed by Nikoobakht & El-Sayed due to

the aforementioned advantages including the ease of the seed-mediated growth method and its relatively high yields [63]

1.2.2. Properties and Applications of GNRs

Gold, as a bulk metal, has numerous advantageous features such as high electrical conductivity, reflectivity, malleability, and corrosion/oxidation resistance. When it is finely dispersed down to the nanoscale, new properties and its use in various applications emerge [91].

To use GNRs to their full potential, it is crucial to convert their unique characteristics into practical applications. In particular, a lot of research has been conducted to employ nanorods to sense and detect different analytes in biological as well as other systems. Variations in the optical absorbance of GNRs can serve as sensitive indicators of both their orientation and surface chemistry. Similar to this, platforms with low limits of detection can be designed using the efficient light scattering of rods. It is possible to both detect and analyze the structure of surrounding analytes using surface-enhanced Raman spectroscopy (SERS) of single or multiple rods [53].

1.2.2.1. Optical Properties

GNRs are excellent substrates for SERS [92], surface-enhanced fluorescence (SEF) [93], chemiluminescence [94], and enhanced localized surface plasmon resonance (LSPR) spectroscopy techniques [95]. Among these, the LSPR theory is explained in detail since our developed CTAB-coated GNR probe takes advantage of the changes observed in the LSPR in the presence of the target analyte.

1.2.2.1.1 LSPR

The LSPR occurs when the conduction band electrons of a metal nanoparticle undergo a collective coherent oscillation in resonance with the frequency of light in the presence of an oscillating electromagnetic field. In its simplest form, this oscillation produces charge separation between the ionic metal core and the free electrons, causing the electrons to oscillate back and forth on the particle surface, resulting in a dipole oscillation. As can be observed in a UV–vis spectrum, the LSPR oscillation

leads to a strong absorption of light, which is the cause of the colloidal solution's color (Figure 7) [96].

The LSPR is affected by the size, shape, and structure of the particles, as well as by the dielectric properties of the metal and the surrounding medium since these parameters influence the electron charge density on the particle’s surface. Depending on the polarization of the incident light, electron oscillation can occur in either the short or long axes in GNRs as shown in Figure 7A. The transverse band, which is induced by excitation of the surface plasmon oscillation along the short axis, is an absorption band in the visible region with a wavelength similar to that of gold nanospheres. Excitation of the surface plasmon oscillation along the long axis creates a much stronger absorption band in the longer wavelength area, known as the longitudinal band (Figure 7B) [54].

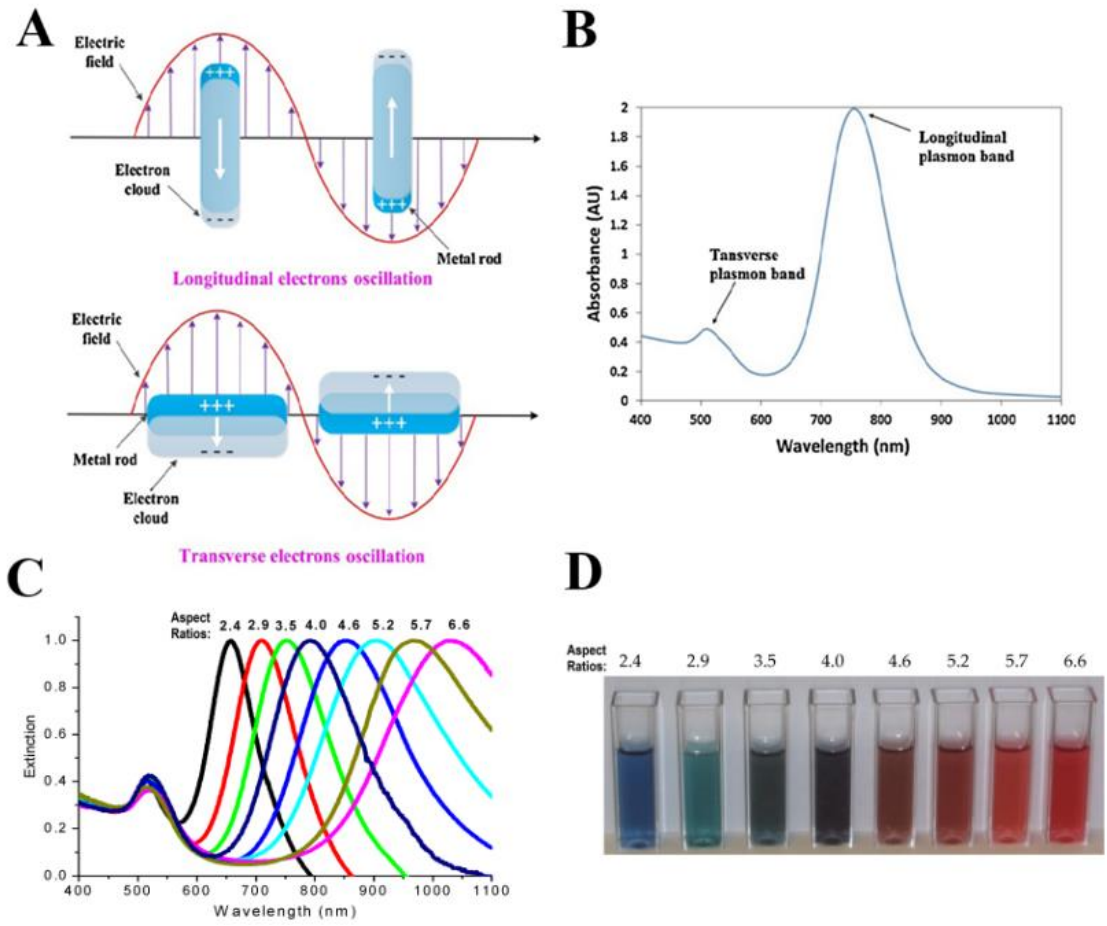


Figure 7. (A) Schematic illustration of LSPR excitation for GNRs and (B) LSPR absorption bands of GNRs. Reprinted from [43] with permission form Elsevier. (C) Change in the LSPR wavelength of GNRs in accordance with their aspect ratios and (D) Color change of GNR solutions varying with aspect ratios [97].

Although the transverse band is not affected by the size of nanorods, the longitudinal band redshifts from the visible to the near-infrared area when the aspect ratio (length/width) increases (Figure 7C) [54]. The Gans [98] theory, was developed using a dipole approximation to explain the optical properties of ellipsoid particles. The LSPR absorption maximum (max) in an aqueous solution is linearly related to the aspect ratio (R) as follows (Eq. 1) [99–101]:

$$\lambda_{max} = 95R + 420 \quad \text{(Eq.1)}$$

Unlike spheres, where the LSPR shifts only slightly with increasing particle size, GNRs can be easily visually adjusted in this way (Figure 7D).

On the basis of Gans theory, Link and colleagues [101] reported simulating the absorption spectra of GNRs as a function of their aspect ratio. The simulated absorption spectra of GNRs with different aspect ratios in a medium with the same value of the dielectric constant are displayed in Figure 8A. With the increasing aspect ratio of the GNRs, it was discovered that the transverse LSPR band has a slight blue shift while the longitudinal LSPR band has a significant redshift. In close agreement with the experimental findings, a linear connection between the peak wavelength of the longitudinal plasmon band and the aspect ratio of the GNRs was also found. They employed Gans theory to model the absorption spectra of the GNRs with a fixed aspect ratio in a medium with a variable dielectric constant, as shown in Figure 8B. Although both the transverse and longitudinal surface plasmon resonance bands exhibit a red shift as the surrounding medium's dielectric constant increases, it can be seen in Figure 8B that the red shift for the longitudinal LSPR band is significantly greater than that for the transverse LSPR band, demonstrating that the longitudinal LSPR band is more sensitive to the change in surrounding medium's dielectric constant [101].

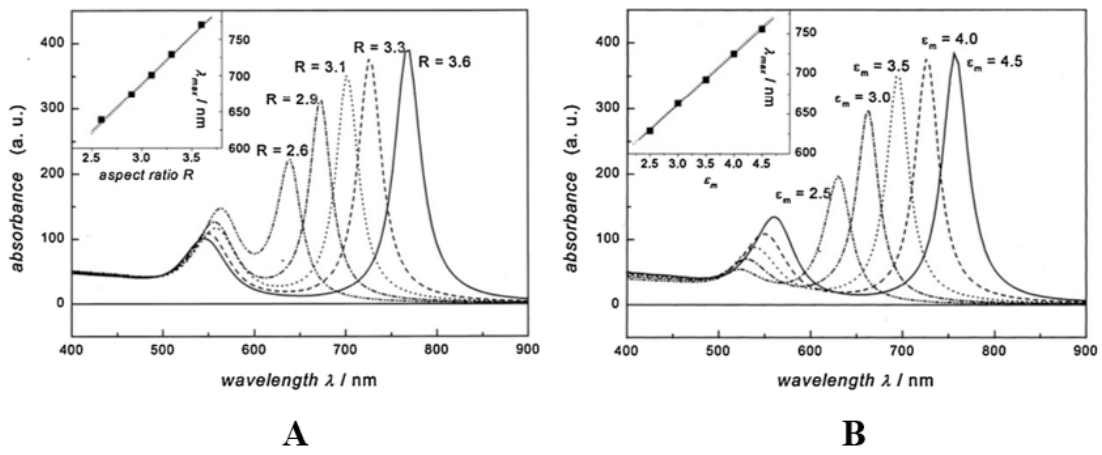


Figure 8. (A) Simulated LSPR absorption spectra of GNRs with a range of aspect ratios in a medium with a fixed dielectric constant (inset: peak wavelength of longitudinal plasmon band increases linearly with aspect ratio of GNRs); **(B)** Simulated LSPR absorption spectra of GNRs with a constant aspect ratio in the medium with a variable dielectric constant (inset: peak wavelength of LPB increases linearly with dielectric constant of the surrounding medium). Reprinted with permission from [101]. Copyright 1999 American Chemical Society.

The Gans theory also allows for the statistical distribution of aspect ratios in a nanorod solution to be determined by fitting the measured inhomogeneously broadened LSPR absorption spectrum of GNRs in solution with a convolution of homogeneously broadened spectra of nanorods, each with various aspect ratio and population contribution [102]. Compared to conventional TEM, this method is a relatively feasible alternative.

The dielectric constant of the surrounding medium affects the LSPR band as well. As the aspect ratio increases, the sensitivity, which is defined as the shift in the SPR wavelength as a function of the refractive index, changes in the surrounding medium and increases linearly. The sensitivity is higher for nanorods with higher aspect ratios, but the resolution may deteriorate as the absorption bandwidth broadens due to the contributions of multipolar electron oscillations [103].

The SPR linewidth is also significantly impacted from the local environmental changes. The narrower the linewidth, the higher the sensitivity to environmental changes. According to Sönnichsen et al. [104], nanorods with a high aspect ratio have the narrowest line widths and thus the longest lifetimes. Since a high aspect ratio is an obvious necessity, researchers investigated the plasmon line widths for nanorods with different widths but identical aspect ratios. As expected, by increasing the width of the nanorod, linewidth broadening was observed. However, surface scattering occurred when the nanorod dimension became much smaller than the electronic mean free path in gold (~20 nm), resulting in increased broadening for small nanorod widths. These two competing processes result in an ideal nanorod width in the 10–20 nm range, where the resonance is sharpest, the lifetime is longest, and the near-fields are greatest [54].

1.2.2.2. Cytotoxicity and Biocompatibility of CTAB-coated GNRs

Due to their excellent qualities, GNRs have become an innovative kind of nanostructure for a variety of biological and biomedical applications [105], such as biosensing [106], biomedical imaging [107], gene [108] and drug [109] delivery, disease detection [110], diagnosis [111], and therapy [112]. Nevertheless, understanding the possible dangers to the environment and human health associated with future clinical trials is crucial [54].

Au^{+} and Au^{3+} are the two common oxidation states for gold. Au^{+} binds to soft ligands like sulfur donors [113], whereas Au^{3+} prefers to group with hard ligands like oxygen or nitrogen donors [114]. Both Au^{+} and Au^{3+} are quickly reduced to yield Au^{0}, frequently in the form of nanoscale colloidal particles. Studies on the biological properties of Au^{+} and Au^{3+} compounds have shown some of them to be beneficial in a medical sense [115]. Gold(I) thiolates, for instance, have been demonstrated to be quite effective in reducing arthritic symptoms [116]. Moreover, due to the chemical inertness of gold, Au^{0} particles are expected to be harmless when they are used in in vivo experiments [117].

However, as previously stated during the synthesis of GNRs, a cationic surfactant, CTAB is frequently used to control the growth of the rods which forms a bilayer structure on the surface and provides dispersity to them [118]. The CTAB compound itself has the ability to directly penetrate across a cell membrane and target mitochondria to induce apoptosis [119]. Contrarily, a CTAB bilayer is adsorbed on the GNRs surface as opposed to dissolved free CTAB molecules or CTAB micelles, thus GNRs should be safe to use in in vivo and clinical research since free CTAB molecules may be isolated using centrifugation or dialysis membrane [54].

Meanwhile, previous studies have shown that CTAB-coated GNRs are toxic to various types of cells [120,121]. Wang and colleagues [122] demonstrated that, as opposed to the surface charge of the quaternary ammonium ions on the surface, the significant cytotoxicity of CTAB-GNRs is caused by the unique CTAB bilayer structure. In a serum-free environment, they found that CTAB-GNRs could enter and penetrate cell membranes, generate defects, and eventually cause damage to the cell membrane. The cell membrane disruption caused by CTAB-GNRs increased lactic acid dehydrogenase release, reduced cell viability, and ultimately resulted in cell death [122]. Therefore, the CTAB bilayer has to be replaced with or entirely enclosed by a more biocompatible coating for utilization in any biological application (Figure 9) [123].

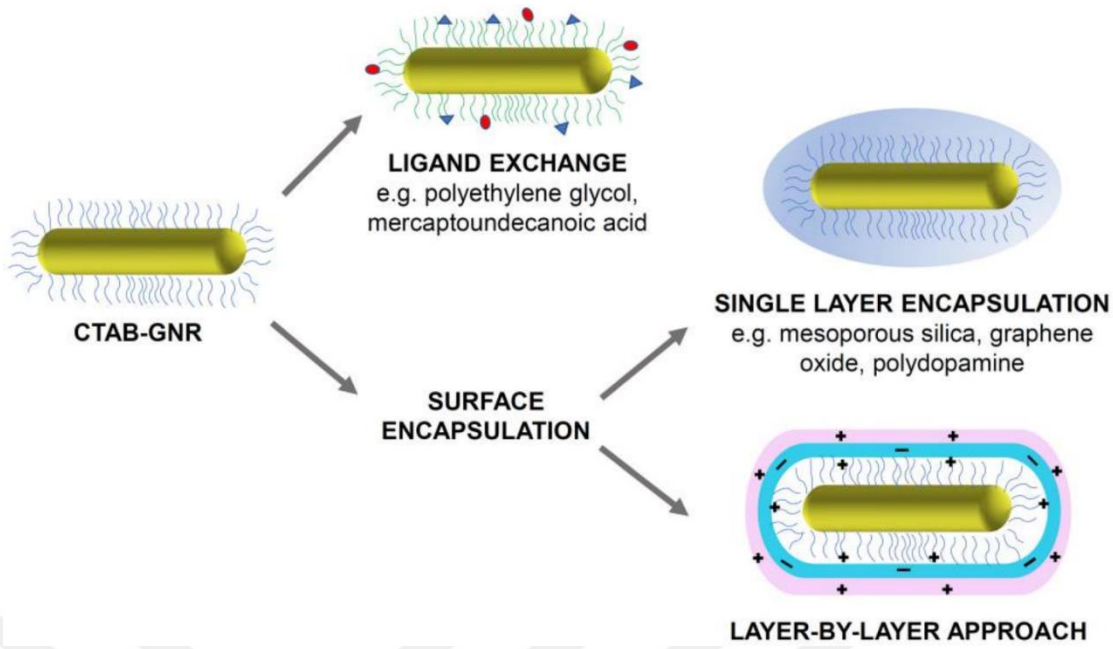


Figure 9. An illustration of several common techniques for functionalizing and detoxifying CTAB-GNRs [123].

One of the most popular techniques for removing CTAB from the surface of GNRs is ligand exchange, which involves the replacement of CTAB with organic ligands or biomolecules (Figure 9). These units improve the GNRs' colloidal stability, prevent them from aggregating, and ensure their biocompatibility. These ligands mostly contain thiol(ate) units because gold has a significant affinity for soft, polarizable sulfur donors and they are made to attach directly to the gold surface rather than covering the CTAB layer [123]. Polyethylene glycol thiols (PEG-SH), or the deprotonated version (thiolates) [124], 11-mercaptoundecanoic acid (MUA) [125], thiolated polyamidoamine (PAMAM) [126] and disulfide polysarcosine (PS) [127] are the some of the ligands that have been investigated in the exchange of CTAB on the surface of GNRs. While great progress has been achieved in this area, it is sometimes difficult to completely replace surfactant units, requiring extra procedures to prevent just partial removal [123].

It has also been possible to improve biocompatibility by encapsulating CTAB-GNRs in inorganic or carbon-based materials to create nanoshells (Figure 9) [123]. These kinds of nanoshells are often constructed of graphene oxide and derivatives [128] or

mesoporous silica [129]. These surface coatings make CTAB-GNRs more chemically stable while also offering a potentially more reliable covering than polymer-based coatings. Additionally, nanoshells can be altered to include surface ligands that may provide extra functionality for targeting and treatment [123]. Moreover, the layer-by-layer method, where the entire positively charged CTAB-GNR surface is covered by numerous, alternating, charged layers, has been shown to be a versatile surface modification strategy. In addition to successfully encapsulating the hazardous CTAB, this straightforward approach for creating multilayers also enables the incorporation of medications, genes, and proteins into the same assembly through electrostatic interactions [130,131]. Despite these approaches offering a relatively simple process to create stable GNRs, the fact that CTAB is still present on the nanorod surface is problematic. The encapsulation of CTAB is thought to be sufficient for eliminating its poisonous impact, however, this has not yet been verified in thorough experiments. To enable the development of these multi-layered nanorods for clinical application, a thorough investigation of the impact of residual CTAB on the toxicity of these materials is necessary [123].

1.2.3. GNRs as Biosensor

The use of GNRs for sensing and detection of diverse analytes in biological and other systems has been the subject of intensive research. The alteration in the optical absorbance of GNRs is a sensitive indictor of changes in GNRs orientation and their surface chemistry [132–134]. In a similar fashion, systems with low detection limits can be created using the effective light scattering of rods. The structure of surrounding analytes can be examined and detected using SERS of single or multiple rods [92,135,136]. Additionally, multiple studies have been reported that use the fluorescence quenching of GNRs for sensing purposes [93,137,138].

1.2.3.1. LSPR-based GNR Biosensors

The LSPR oscillation in GNRs leads to a strong absorption of UV-Visible light, that can be utilized in the development of sensitive optical biosensors. As previously mentioned, GNRs display both transverse and longitudinal LSPR where especially the

longitudinal LSPR band shows response to changes in the size, aspect ratio, orientation, or the morphology of the GNRs, as displayed by the changes in the intensity and its location. [54].

Consequently, there are many GNR-based biosensors developed that are mostly taking advantage of the longitudinal LSPR band. In general, GNR-based LSPR biosensors are categorized in three main groups: assembly-based biosensors, refractive index-based biosensors, and morphology change-based biosensors.

1.2.3.1.1. Assembly-based Biosensor

GNRs may assemble in various types of patterns due to their anisotropic structure, including end-to-end chains[139–141], side-by-side orientation [45,142], rings [143], and other multiple-dimensional assemblies [144]. These patterns are all associated with the coupling of the GNRs surface plasmon bands. The end-to-end and side-by-side forms of these assemblies (demonstrated in Figure 10) have drawn the most interest and have since been further developed as sensors for chemical and biological analysis based on the optical changes caused by the assembly [145].

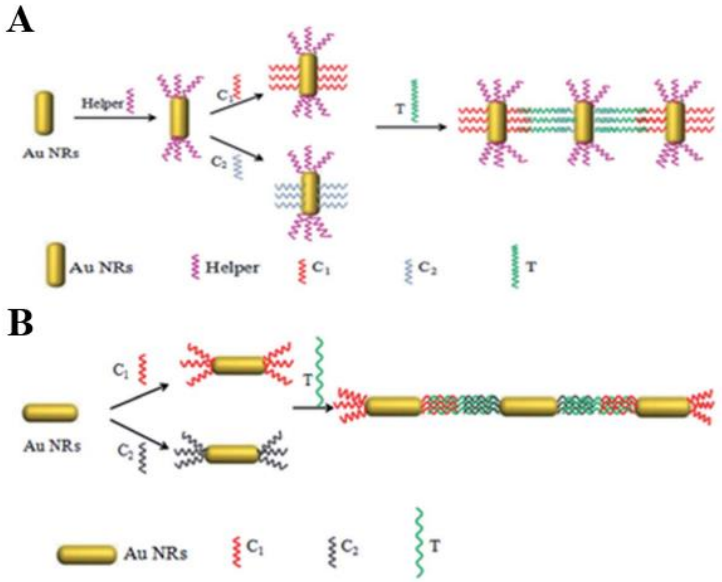


Figure 10. Schematic representation of (A) side-by-side and (B) end-to-end assembly of GNRs. Adopted from [146] with permission RSC Publishing.

1.2.3.1.1.1. End-to-end Assembly

The CTAB bilayer creates structural and chemical anisotropy by coating the {100} and {110} planes of the lateral sides while remaining the {111} facets of the edges less coated [118]. The ends of GNRs show higher chemical sensitivity than the lateral sides due to the lower local density of CTAB at the tips compared to the lateral sides. This makes the ends more preferable to functionalize and results in end-to-end assembly with red shifted longitudinal LSPR [147,148]. As a result, by attaching ligands to the tips of GNRs, particular recognition based end-to-end GNRs assemblies may be generated [149,150].

A red shift in the LSPR, however, should not be taken as absolute evidence of end-to-end assembly. The red shift can also result from random aggregates [151]. A red shift of the transverse LSPR peak that generally is not observable in an end-to-end assembly may also emerge from random aggregation [152]. Even a simple decrease in CTAB concentration during sample drying has been claimed to be able to achieve some degree of end-to-end assembly [153].

The most straightforward assembly of GNRs may be generated simply using the target molecules, that uses a dithiol group [154] or intermolecular interactions such as hydrogen bonds [140] or electrostatic interactions [155] between molecules of the same type. Moreover, the most commonly used ligand-target recognition-based patterning techniques for orienting GNRs in the end-to-end mode include biotin-streptavidin [147], antibody-antigen [156] , aptamer-target [150], ligand-metal [149], and DNA hybridization [157]. The aforementioned assemblages are mostly the result of the chemical interaction between the tips of GNRs and functional groups like thiol-groups. Via the usage of suitable molecular recognition, other, more complex techniques might be created for metal-amino acid [148] and DNAzyme-metal detection [158].

1.2.3.1.1.2. Side-by-side Assembly

The lateral sides of GNRs differ from the chemically active tips in that they are densely capped with CTAB bilayer [118], causing them to be less susceptible to thiol-related

modifications than the tips [159]. In most cases, side-by-side assemblies are the consequence of electrostatic [144] or hydrophobic [160] interactions between CTAB and the adsorbates. These assemblies may also be arranged through hybridizing thiolated DNA to end blocking [157,161]. In side-by-side assembly, a red shift occurs in the transverse LSPR while, a blue shift is observed in longitudinal LSPR [162].

In the literature, selective binding of multivalent species, such as DNA [144], peptides [163], citrates [164], biotin/streptavidin, [165] and antibodies [45], to the sides of rods or all over their surface would also induce side-to-side aggregation.

1.2.3.1.2. Morphology Change-based Biosensor

GNRs' unique optical properties are often incredibly beneficial in their colorimetric applications. According to studies published in the literature, the selective detection of most target analytes by GNR-based sensors results in a sensitive rainbow-like color change, which can be easily detected by the naked eye [166]. As previously stated, the longitudinal band of GNRs is susceptible to their aspect ratio, and as the aspect ratio increases, the longitudinal band shifts to a longer wavelength, often accompanied by an apparent color change [103].

The evolution of the morphology of GNRs, and hence their aspect ratio, may be classified into two categories: growth-based mechanisms and etching-based mechanisms [167]. The surface changes in GNRs caused by these two routes cause a sensitive shift in their LSPR peak as well as a multicolor shift in the detection solution [103].

1.2.3.1.1.1. Growth-based Biosensor

The growth-based approach depends on forming a new metal layer on the original plasmonic nanoparticles by reducing the precursor metal ions by introducing the analyte to the system. In this instance, the analyte may function directly as a reducing agent or indirectly as a reducing agent generator in the medium [168]. The crystal lattice of the deposited metals often matches that of the original plasmonic nanostructures. This kind of colorimetric sensors utilize the reduction of silver salts

because silver and gold are suitable crystal structures. It is also possible to generate methods that alter the shape and size of GNRs by generating analyte-induced gold deposition on nanorods [169].

Overgrowth on the surface of GNRs results in a sharp-contrast multicolor change [170] and it has been used for colorimetric detection of ascorbic acid [171], formaldehyde [172], biogenic amines [173], immunoassay [174], and enzyme activity [175].

1.2.3.1.1.2. Etching-based Biosensor

The interaction between etchants with metal nanoparticles is referred to as etching. The etchant changes the form of the metal nanoparticle by oxidizing the component atoms (such as Au^0) and converting them into ions that are soluble in water (such as Au^+ or Au^{3+}). The aspect ratio of the GNRs directly affects their plasmonic properties. Therefore, the obvious blue shift in LSPR, proportionate to the analyte concentration, makes it simple to study the shortening of the rods along the longitudinal axis. The fluctuation in plasmonic characteristics is caused on by the reduction in GNRs length, which is seen in the different color variations [176,177]. The etching progress can be seen from the solution's color, which changes from dark orange to green, cyan, blue, violet, pink, colorless, and yellow, as the length of GNRs changes [178]. The sensitivity and specificity of the constructed sensor may be improved by the presence of specific etchants and optimization of reaction parameters including ionic strength and pH of the medium, CTAB concentration, temperature, and the ratio of reactive elements. GNRs etching can frequently be promoted by higher temperatures (above 25°C), an acidic pH, and the presence of CTAB in the solution [169].

By regulating the electrostatic interactions, CTAB is essential in determining the size and form of the GNRs. Because the standard electron potential of the Au^+/Au is 1.69 V and they are difficult to oxidize, GNPs have been reported to be highly stable. CTAB lowers the Au^+/Au reduction potential, promotes the redox process, and enhances the etching of GNRs [179,180]. For instance, it has been suggested that Br^- ion in CTAB results in the $AuBr_2^-$-CTA^+ pairing on the surface of GNRs. As a result, it lowers Au^+/Au's reduction potentials [181]. Therefore, in combination with the effects of the

etchants (such as HO•, I_3^-, 3,3',5,5'-tetramethylbenzidine (TMB^{2+}), etc.), the concentration of CTAB has been incorporated with the etching of GNRs. Etching occurs along the longitudinal axis and begins at the tips of the GNRs when a larger concentration of CTAB is present [182,183]. Conversely, when the quantity of CTAB in the solution is decreased, the side facets of the GNRs also react [184,185].

Overall, etching-based detection platforms for GNRs can be classified into five main categories: direct etching, complex-promoted etching, intermediate-mediated etching, inhibitor-mediated etching, and enzyme-mediated etching [186]. Among those, direct etching, complex-promoted etching and intermediate-mediated etching was explained in detail below.

1.2.3.1.1.2.1. Direct Etching-based Biosensor

Gold often exhibits good stability and is difficult to oxidize due to its high reduction potential. But when the bulk material was decreased to nanoparticle size, the active surface increases, resulting in a decrease in the reduction potential [186]. As shown in Figure 11, materials with greater reduction potential than Au^+/Au reduction potential, such as mercury ion [187–189], ferric ion [190,191], chromium ion [192–194], copper ion [195,196], nitrite ion [197,198], and hydrogen peroxide [199,200], can directly etch GNRs. In the majority of situations, additional CTAB is introduced into the medium, which causes Br^- ions to interact with Au atoms and lower their reduction potential (Eq. 2.). The analyte itself also serves as an etchant in these sensors [168].

$$AuBr_2^- + e^- \rightarrow Au + 2Br^- \quad \text{(Eq.2)}$$

Direct etching is a simple and low-cost analytical technique, but its on-site application may be constrained by high working temperatures or highly acidic (low pH) environments. Since the detection signal can be analyzed with the naked eye rather than a complex instrument, the direct etching approach is often appropriate for in-situ detection. The suggested approach showed a substantial sensitivity compared to the traditional optical methods based on the colored complex creation [168].

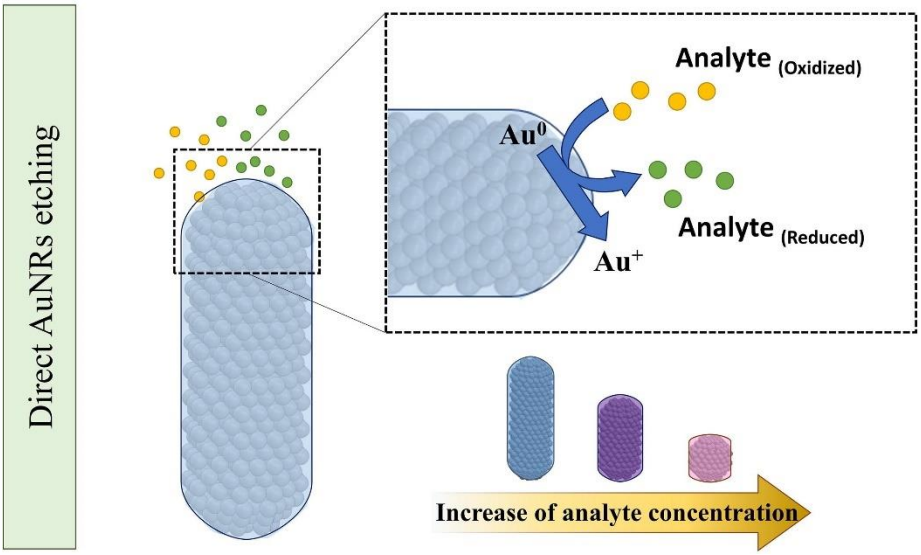


Figure 11. Schematic illustration of direct etching of GNRs. Reprinted from [168] with permission form Elsevier.

1.2.3.1.1.2.2. Complex-promoted Etching-based Biosensor

Thiol (-SH) groups in substances like thiourea [201], and thiosulfate [202], and the cyanide group [203] are known to form stable complexes with gold atoms. The Au^{+}/Au reduction potential is significantly decreased by the complex formation (Figure 12). As a result, analytes can serve as the etchant, removing the gold complex from the surface of the nanoparticle and etching the GNRs. The etching process is facilitated and accelerated by the complex formation.

Due to the electrostatic attraction between thiosulfate ($(S_2O_3)_2^{2-}$) and CTAB on the GNR's surface, it was assumed that thiosulfate would adsorb onto the GNR's surface. As a result, a redox reaction will take place at the solid-liquid interface in the presence of oxygen, resulting in the formation of the $Au(S_2O_3)_2^{3-}$ complex and the partial dissolution of the GNRs [204]. Thiourea ($CS(NH_2)_2$) reduces the reduction potential of Au^{+}/Au to create stable cationic species ($Au(CS(NH_2)_2)_2^{+}$) that speed up the etching process [205]. The standard electron potential of $Au(CN)_2^{-}$ in the absence or weak presence of bromide and chloride anions is substantially lower compared to that of Au^{+}/Au^{0} in the presence of bromide and chloride anions, allowing cyanide(CN^{-}) to successfully oxidize GNRs [203].

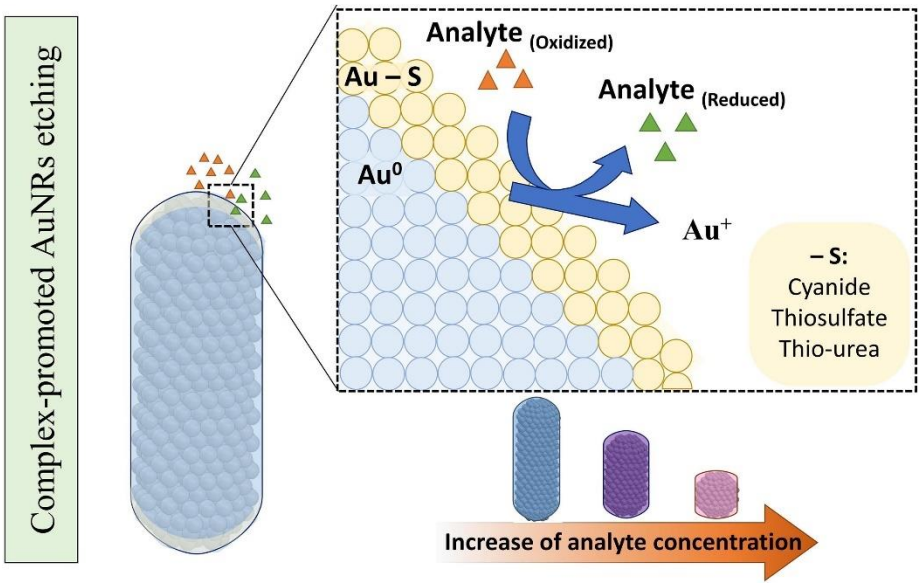


Figure 12. Schematic representation of complex-promoted etching-based sensors. Reprinted from [168] with permission form Elsevier.

Alloy formation is also used to obtain this kind of sensors [169]. Due to the alloy formation taking place more effectively on the ends of the nanorods, which are where the active sites of GNRs are mostly located, the aspect ratio of the nanorods decreases [187]. Mercury-gold amalgam [206] and lead-gold alloy [207] formations are some of the examples of this technique to obtain complex-promoted etching-based sensors.

The user-friendly, economical, and straightforward complex-promoted etching approach frequently exhibits high sensitivity on the nanoscale. However, using cyanide and thiosulfate might put operators of this sensor in danger or cause environmental pollution. Aside from that, this approach might have additional limitations such as high temperature and prolonged etching times [168].

1.2.3.1.1.2.3. Intermediate-mediated Etching-based Biosensor

Iron, cobalt, halide, and mercury ions have all been used as mediators in the intermediate-mediated etching process (Figure 13). Strong oxidants (etchants) are produced as a result of the processes that the mediator starts. As a result, an intermediate would perform etching in proportion to analyte concentration [168]. The high oxidation capacity of reactive intermediates can promote the dissolution of GNPs

once the formation of these intermediates such H_2O_2, •OH, O_2•$^-$, and I_2 is selectively generated by mediators. As a result, the shape of gold nanoparticles changes, which also cause variations in the detecting system's LSPR band and hue [208].

Researchers discovered that H_2O_2 allows for the selective oxidation of GNRs. However, because of its slow reaction rate and prolonged oxidation time, this method of chemically etching GNRs frequently has a significant drawback. The effective oxidation of some target molecules is made possible by the active oxygen radicals, superoxide radical (O_2•$^-$) and hydroxyl radical (•OH), which have high reduction potential and a significantly better oxidizing capacity than H_2O_2 [209].

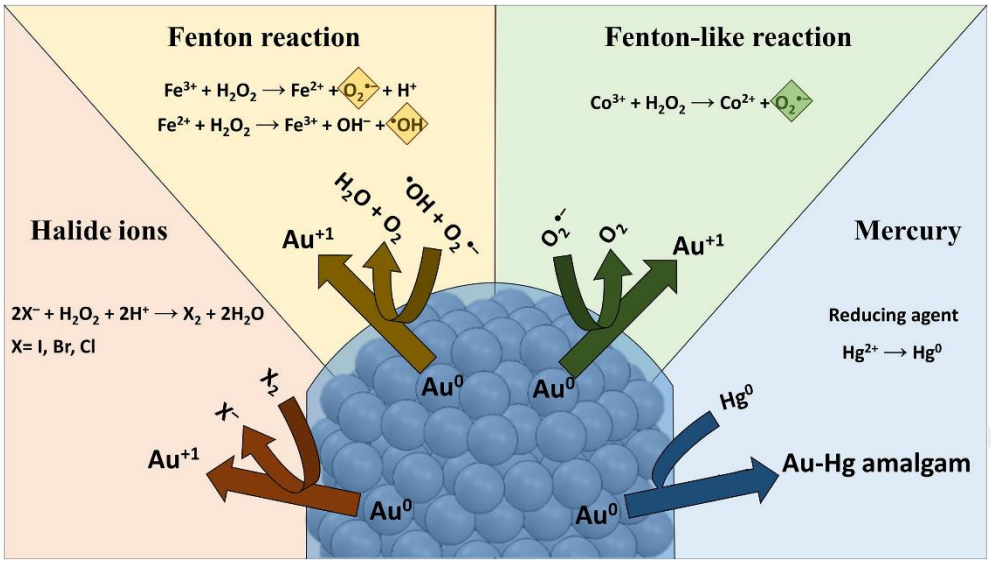


Figure 13. Diagrammatic representation of different approaches of development of biosensors based on intermediate-mediated etching of GNRs. Reprinted from [168] with permission form Elsevier.

1.2.3.1.1.2.3.1. Halide Ions-mediated Biosensor

It has been found that halide ions, such iodide and bromide, have a noticeable impact on GNPs shape-controlled syntheses and plasmonic wavelength tuning [212]. Halide ions have the ability to lower reduction potential of Au^+/Au. On the other hand, halide ions become more powerful etchants than oxidants when they are subjected to an oxidant such as H_2O_2 [213]. Iodine and bromine (X_2, X = I, Br) are the products of the interaction of iodide (I^-) and bromide (Br^-) ions with various oxidants. Subsequently,

X_2 and X^- combine to generate X_3^-, which is essential for etching GNRs as outlined in Eqs. 3-7 [213].

$$2X^- + H_2O_2 + 2H^+ \rightarrow X_2 + 2H_2O \quad \text{(Eq. 3)}$$

$$X_2 + X^- \rightarrow X_3^- \quad \text{(Eq. 4)}$$

$$X_3^- + 2Au \rightarrow 2AuX + X^- \quad \text{(Eq. 5)}$$

$$2AuX + 2Br^- \rightarrow AuBr_2^- + X^- \quad \text{(Eq. 6)}$$

$$AuBr_2^- + 2CTA^+ \rightarrow AuBr_2^- - (CTA^+)_2 \quad \text{(Eq. 7)}$$

Nevertheless, Weng et al. [210], showed that, in three types of halide ions, the binding strength and etching rate of GNRs varied. They investigated how halide ions affected CTAB- and cetyltrimethylammonium chloride (CTAC)-capped GNRs' oxidative etching. The findings demonstrated that the etching speed of GNRs increased with binding strength. As a result, the three different kinds of halide ions had different etching effectiveness, acting in the following order: $Cl^- < Br^- < I^-$ in coherence with their binding affinity. They stated that by means of chemisorption, the iodide ions exhibited a significant affinity for Au surfaces and may cause surface etching on the adsorbed facets. Hence, iodide ions might be used to etch GNRs that had been stabilized using CTAB or CTAC. On the other hand, bromide ions can only be used to etch CTAB stabilized GNRs, since it has relatively low binding strength. In the case of chloride ions, neither of the two types of GNRs could be etched due to the poor binding strength between Au and Cl^-. They also marked that stabilizers like CTAB and CTAC would have an impact on how easily GNRs were etched when halide ions were present. Through the micelle effect, CTAB and CTAC would increase the solubility of X_2, and via strong binding interactions, they would stabilize the X_3^- complex [211].

Since iodide is the most commonly used halide ion to promote the oxidation of GNRs in the literature, thus, halide mediated-etching may also be referred as iodine- or iodide- mediated etching [212–215]. Typically, the etching reaction causes the LSPR of GNRs to blue-shift and give rise to a spectrometric and visual signal change that was used to detect target analytes [166] such as toxins [216,217], dissolved oxygen

[212], glucose [213], dopamine [218], aminotriazole [219], cholesterol [220], uric acid [220], enzyme activities [221,222] and enzymes [214,223,224].

1.2.3.1.1.2.3.2. Fenton and Fenton-like Reactions-mediated Biosensor

In 1894, Fenton discovered that $[Fe(H_2O)_6]^{2+}$ catalyzes the H_2O_2 oxidation of tartaric acid [225]. The reaction between $[Fe(H_2O)_6]^{2+}$ and H_2O_2 is named as the Fenton reaction, while reactions involving different metals, ligands, and/or peroxides are referred as Fenton-like reactions [226].

Researchers discovered that various common oxidants, such as O_2 and H_2O_2, have oxidative etching capacity to etch GNRs in warm water under acidic conditions, which can be used to fabricate colorimetric sensors [178,209]. However, this chemical etching method of GNRs usually has a major drawback due to its slow reaction rate and long oxidation time (more than 12 h) [178]. As a result, expanding the use of H_2O_2-caused or O_2-mediated GNRs plasmonic sensing probes to detect H_2O_2, O_2, and other relevant targets is not feasible [177,209,227].

Initially, it was well understood that Fenton and Fenton-like reactions can effectively generate active oxidants such as the hydroxyl radical (•OH) and superoxide radical (O_2•$^-$) [226]. More crucially, these active oxidants have far better oxidizing abilities than H_2O_2 or O_2 [228], allowing them to successfully oxidize some target molecules, including organic [229] and inorganic compounds [230]. Because most active oxygen species have a high reduction potential, they can etch GNRs and cause a change in the shape dependent longitudinal LSPR of GNRs under certain conditions, usually accompanied by a vivid color change in the visible region [231]. As a result, these Fenton and Fenton-like systems can generate reactive hydroxyl and superoxide radicals, which has inspired a lot of interest in developing GNR etching-based multicolorimetric sensors for visual quantification of a variety of analytes with the naked-eye [166].

In the process known as the Fenton reaction, Fe^{2+} ions are used to reduce hydrogen peroxide and simply produce hydroxyl radicals. Due to the stronger oxidizing ability of the hydroxyl radical than H_2O_2, this reaction system provides strong oxidant species

simply and directly and also enables the etching of GNRs to achieve a multicolor change. As a result of the oxidative etching of GNRs, H_2O_2 or its related compounds can be visually recognized [231]. For example, in 2013, Liu et al. [232], investigated a simple colorimetric assay for blood glucose detection based on the oxidative etching principle of GNRs, which relied on hydroxyl radical-enhanced GNR oxidation etching via a Fenton reaction.

Fenton-like processes, which can yield reactive oxidants, have recently been investigated for the development of GNR etching-based multicolorimetric sensors [167]. These systems usually demonstrate the Fenton reactions. Some metal ions, such as copper [233], aluminum [234], cobalt [230], and silver [235], have been studied because they can produce reactive oxidants in a liquid environment via a Fenton-like reaction. In these target-induced and target-triggered Fenton-like reactions, many active oxidants can be employed to etch GNRs and produce color-based sensors. According to this perspective, targeting relevant Fenton-like processes is critical for constructing and developing GNR etching-based multicolorimetric sensors [166]. Zhang et al. [231], for instance, suggested and effectively implemented a novel Fenton-like reaction-mediated etching of GNRs for the sensitive visual detection of Co^{2+} ions in 2015. In the presence of SCN^-, Co^{2+} analytes were proposed to induce a Fenton-like reaction, resulting in the formation of a large amount of superoxide radicals, which oxidized the GNRs and created Au^+ ions.

Fenton and Fenton-like reactions-mediated etching of GNRs are widely used to detect biological targets including single-nucleotide polymorphisms [236], biomarkers (cholesterol, glucose and uric acid) [220], glucose [213], nucleic acids, proteins, and small molecules [237], telomerase activity [238], ribonucleotides[239], and ascorbic acid [240].

1.2.3.1.1.2.3.3. Mercury-mediated Etching-based Biosensor

The high affinity and specificity of Au and Hg can be employed for detecting particular analytes [188]. When Hg^{2+} is reduced via a reducing agent, Hg^0 is formed. As a result of this reaction and Au and Hg affinity, Au-Hg amalgam is produced [187]. The most

productive locations for the amalgam's creation are the tips of the GNRs, where the CTAB density is the lowest. However, the densely CTAB-covered side faces of the GNRs do not exhibit any activity for the Au-Hg interactions. As a result, the longitudinal LSPR's absorption peak experiences a blue shift, the GNRs' aspect ratio is further decreased, and the size decrease of GNRs becomes apparent along its longitudinal axis (Figure 13) [189]. This type of etching of GNRs as a biosensor is used to detect vitamin C [241] and cysteine [242].

1.3. Nucleic Acid Detection Platforms

1.3.1. Nucleic acids

Nucleic acids are polynucleotides that are responsible for storing, encoding, transmitting, and expressing genetic data. There are two main types of nucleic acids: deoxyribonucleic acid (DNA) and ribonucleic acid (RNA) [243]. The building blocks of nucleic acids are the nucleotides that consist of a phosphate group, a pentose sugar and a nitrogenous base (Figure 14). In RNA, the pentose is D-ribose; in DNA, it is D-2-deoxyribose. By coupling through ester linkages created by the phosphate group between the 5′-OH^- of one nucleotide's pentose and the 3′-OH^- of another nucleotide's pentose, nucleotides form chains. The 5′ of pentose is free at the end of the chain, which is accepted as the chain's beginning. The last nucleotide is considered as the 3′ end of the molecule since its C3′ is nonesterified [244]. The nitrogenous base may be a pyrimidine or purine derivative [245]. While pyrimidines only have one nitrogen-containing ring, purines are made up of two nitrogen-containing rings, pyrimidine and imidazole. There are five main nucleotide bases found in nucleic acids. There are two purines and three pyrimidines. Adenine (A) and guanine (G) are the purine and thymine (T), uracil (U) and cytosine (C) are the pyrimidine bases [246]. DNA contains A, G, C and T, while RNA contains A, G, C and U instead of T [247].

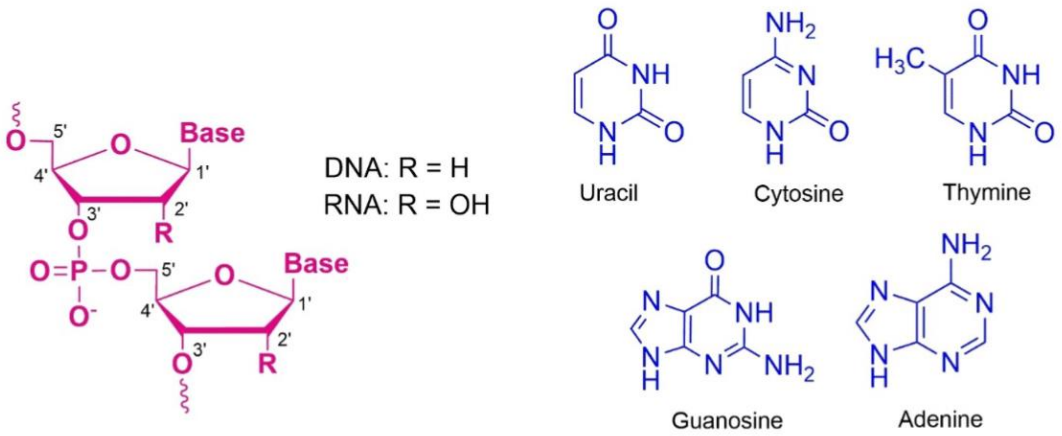


Figure 14. Structural unit of nucleic acids and nitrogenous bases. Reprinted from [248] with permission John Wiley and Sons.

1.3.1.1. Structures of DNA

The main form of DNA in our cells is a right-handed helical duplex, or B-DNA, whose structure was initially proposed by Watson and Crick in 1953 [249]. The genomic DNA often exists in living cells as double stranded. But during DNA metabolic processes like transcription and replication, the double helix becomes partially unpaired into a single-stranded pattern. There are also repeated DNA sequences in a few of the unwounded single-strand sequences [250]. It is well-accepted that less than 3% of the human genome is made up of simple sequence repeats, but repetitive DNA sequences constitute over 50% of the total genomic DNA [251].

The folding of the unique or repeating DNA sequences are known to result in the formation of non-B DNA structures such hairpins, cruciforms, triplexes (H-DNA), left-handed Z-DNA, tetraplexes (G-quadruplex (G4) and i-motif), slipped strand DNA, etc. [250,252–255]. To create these structures, the DNA strands must fold differently from B-DNA or form unique base pairs, such as Hoogsteen base pairs, which are distinct from Watson-Crick base pairings (A–T, G–C) in that they establish unusual hydrogen bonds among nucleic acid bases. Hoogsteen base pairs have a significant impact in the stability of certain non-B DNA conformations [256]. For example, hydrogen bonds between G–G affects stability of G4 [257], C–C affects

stability of i-motif [258], G–G–C impacts stability of triplex [259], and A–A impacts stability of A-motif [260] (Figure 15).

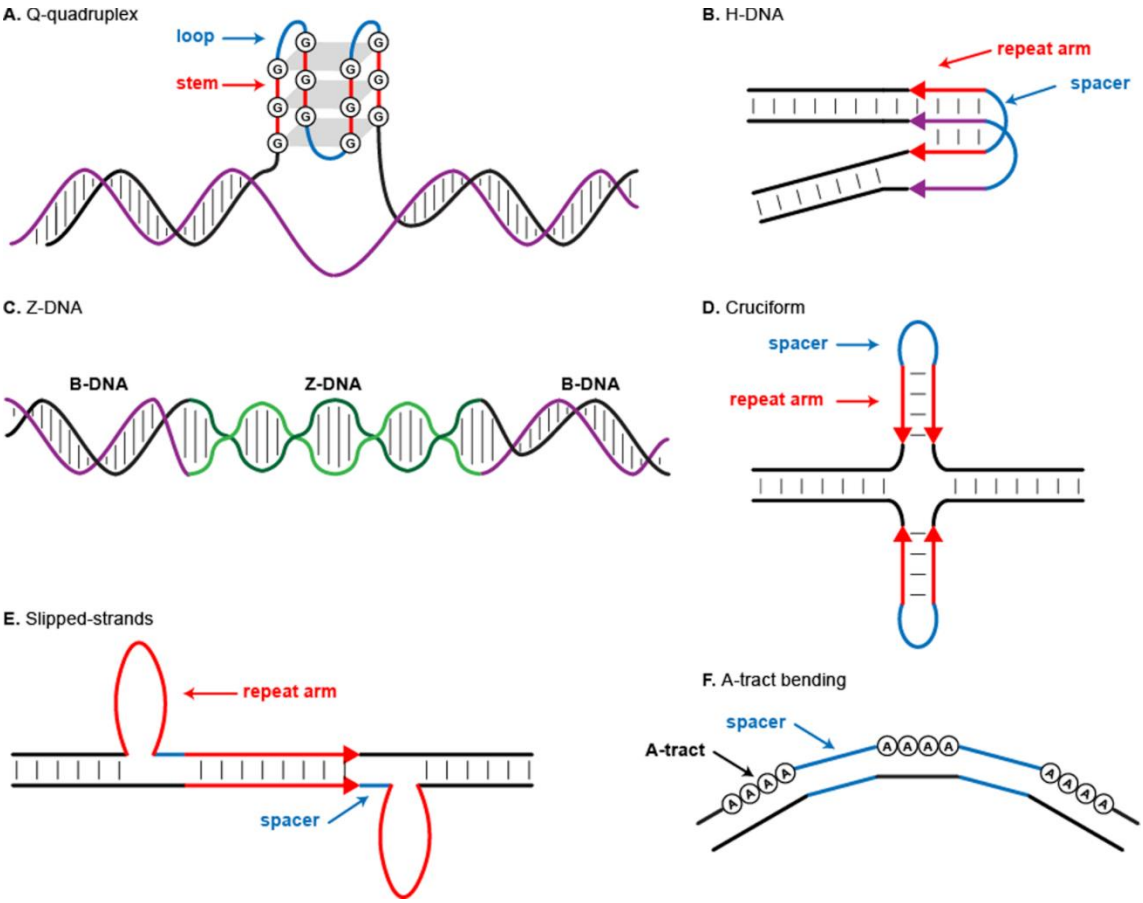


Figure 15. Different types of non-B DNAs (A) G4, (B) H-DNA, (C) Z-DNA, (D) Cruciform, (E) Slipped strands, (F) A-tract bending. Reprinted from [261] with permission Oxford University Press.

1.3.1.1.1. G-quadruplexes

It was initially discovered in the 1960s by Gellert and Davies that guanosine 5'-monophosphate forms helical aggregates of four units in each helical step [262]. Biochemical tests conducted in the late 1980s revealed that oligonucleotides with segments of three or four contiguous guanines (G-tracts), which are present in telomeric DNA, spontaneously generate G4 or G-tetraplexes, which are four-stranded DNA structures [263]. The G-quartets that result from Hoogsteen hydrogen bonding between four guanines are the building blocks of G4s. Four-stranded helical structures

are created by π-π stacking of the planar G-quartets on top of one another [264]. Monovalent cations like K^+ and Na^+ are extremely important for the creation of these structures, which is why physiological buffer conditions are favorable for their production [265] (Figure 16). Several three-dimensional structural investigations have demonstrated the high polymorphism of G4 DNA structures, which may be further classified into several families, such as inter- or intra-molecularly folded, or hybrid, parallel or antiparallel based on strand orientation [266–268]. However, it is necessary to consider the in vitro thermodynamic and kinetic features of G4s when evaluating the possibility of G4 formation and potential functions in biology [268].

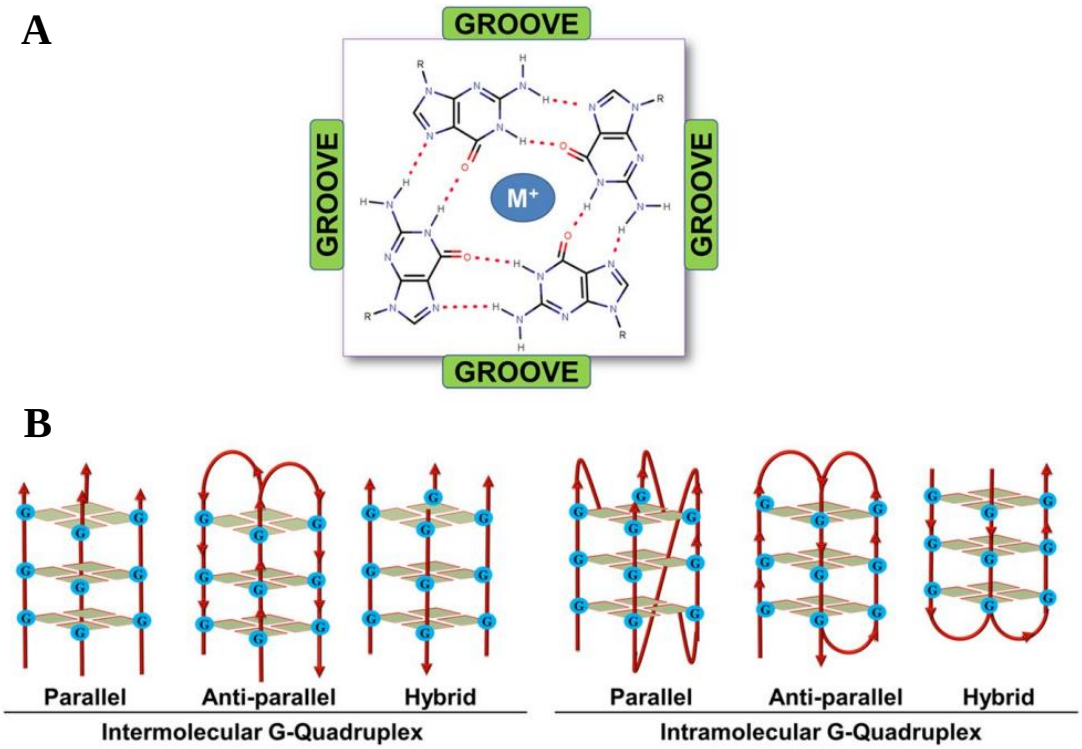


Figure 16. (A) Structure of a G-quartet, (B) different G4 topologies, where M^+ is a monovalent cation [269].

G4 signature sequences have been used in genome-wide sequence analysis to uncover crucial details about the presence and positioning of these sequences with the capacity to construct stable putative G-quadruplexes (PG4) [270–272]. The position of PG4s is non-random and appears to be associated with functional genomic regions, despite the fact that their occurrence in genomes is one-third less than would be predicted [273].

The traditional Watson–Crick base-pairing would need to be interrupted in order for Hoogsteen base-pairing to occur since genomic DNA is in the double helical shape, which prevents G4 production by PG4s [274]. Opportunities for this are thought to occur during the processes of transcription, recombination, and DNA replication when certain parts of double-stranded DNA temporarily become single-stranded [275]. These activities also shown to lead to negative DNA super-coiling, which would encourage G4 formation further [276]. For instance, the very ends of telomeres are inherently single-stranded G-rich regions and, thus, energetically more advantageous to form G4s [274].

1.3.1.1.1.1. Telomeric G-quadruplexes

Telomeres, nucleoprotein structures, play a vital role in stabilizing and protecting eukaryotic chromosomes. They are the highly regulated dynamic complexes located at the ends of chromosomes. The primary function of telomeres is to prevent the misrecognition of chromosome ends as DNA double-strand breaks. This misidentification could lead to improper initiation of DNA damage repair processes, resulting in telomere-telomere fusion and genomic instability. In other words, ensuring the continued proliferation of cells relies on the telomeres and the telomerase enzyme [277]. Telomeres consist of tandemly repeated short DNA units and are associated with protective proteins [278]. The DNA component of telomeres consists of multiple hexanucleotide sequences, specifically TTAGGG in humans. The length of this telomeric DNA varies from 5 to 15 kb, depending on the cell type and replication history. It terminates in a 3′ single-stranded region known as the 3′ G-overhang. Additionally, the protective proteins that bind to the telomeric DNA are crucial for maintaining proper telomere length and ensuring their structural and functional integrity [279].

The ribonucleoprotein complex named telomerase comprises two essential components including the enzyme telomerase reverse transcriptase (TERT) and telomerase RNA (TER) [280]. Together, they serve as a template for replicating telomeric repeats at chromosomal ends. In humans, telomerase expression is limited to a small number of cell types, and under normal conditions, its levels are tightly

regulated. On the other hand, a significant portion of human cancers demonstrate heightened telomerase levels, and researchers are only beginning to uncover the mechanisms through which cancer cells enhance telomerase activity [281]. Conversely, germline mutations that affect telomerase activity, leading to its reduction, are associated with a range of hereditary diseases, including dyskeratosis congenita [282], idiopathic pulmonary fibrosis [283], and bone marrow failure [284].

The human telomeric overhang can potentially adopt a G4 configuration [285], although the precise mechanism of this phenomenon remains an active research subject [286]. As stated before, the formation of G4s in human telomeres occurs rapidly, and under physiological conditions, these structures are thermodynamically stable [287]. Numerous studies have revealed that G4 structures play diverse roles, including telomere capping [288], regulation of replication initiation [289], and transcription [290]. On the other hand, G4 structures have also been shown to impede replication fork progression [291] and contribute to genomic deletions [292], mutations [293], and recombination events [294]. Besides, telomeres also possess a crucial role in aging [295] and are implicated in cancer development [296] processes because alterations in their structure are linked to apoptosis [297] and uncontrolled cell division [298]. However, to maintain genome integrity and cellular function, it is essential to untangle G4 structures, as they act as barriers to the activation of the replication, transcription, and translational processes [299]. To facilitate telomerase access to the 3′ ends of chromosomes, cells must unfold these structures into a single strand. Failure to properly regulate G4 structures, whether due to uncontrolled formation or breakage, disrupts cellular functions, and has been linked to various illnesses and genetic instability [299,300]. While certain cell types do not exhibit telomerase activity and maintain telomere length through alternative mechanisms, it is generally observed that increased telomerase activity leads to telomere lengthening [301]. One intriguing strategy in cancer treatment involves the stabilization of telomeric G4, which can effectively suppress telomere lengthening in cancer cells [302].

1.3.2. Physiological Importance of Telomeric G4s and their Detection

G4s are unique DNA structures, but investigation of their structural, biochemical, and thermodynamic properties has led to the debate of whether they are just an in vitro artifact or physiologically meaningful. G4s could potentially possess significant roles in vivo based on the presence of distinctively guanine-rich motifs in several essential areas of the eukaryotic genome, such as the immunoglobulin heavy chain switch region, ribosomal DNA, certain promoter regions, minisatellites, and telomeres [303].

According to estimations, the human genome may include up to 376000 sequences that have the ability to create G4 [304,305]. In eukaryotes, telomeres are crucial for maintaining the organism's genomic integrity. Because of the end replication problem, DNA is lost after each linear chromosome replication [306]. Therefore, telomeric DNA acts as a disposable, non-coding buffer to stop the loss of crucial genetic information. Chromosomal end-to-end fusions are prevented by telomere-associated proteins, which inhibit the DNA-repair machinery's ability to recognize chromosomal termini as double-stranded breaks [303].

As previously stated, repetitive G-rich DNA that is composed of TTAGGG forms the human telomere repeats. The G-overhang is a single-stranded overhang that extends from the extreme 3’-end of telomeric DNA, which is mostly double-stranded [307]. The ribonucleoprotein enzyme telomerase [308] relies on reverse transcription of an incorporated RNA template to synthesize the G-rich strand of telomeres [309]. The majority (>85%) of cancer cells display high quantities of telomerase [310] and appear to have the ability to extend telomeric regions, in contrast to the majority of normal somatic cells, which have extremely low levels of this enzyme and stop proliferating once their telomeres reach to a critical length. Thus, telomerase and the telomere, which is its substrate, have emerged as important targets for anti-cancer treatment [303].

Zahler et al. [311] showed that G4 folded telomeric DNA inhibited telomerase activity in vitro. Based on this finding, a substantial amount of research has recently been conducted to find the synthetic and natural substances that might lock telomeric DNA in a G4 shape or inhibit telomerase hence inhibiting telomere extension in vivo in

addition to the studies aiming to verify the presence and monitoring of G4s in vivo. The number of studies aiming to identify the plausible roles of G4s has also increased substantially [303].

Schaffitzel and colleagues [312] have developed synthetic single-chain antibody (Ab) fragments (scFv) specifically targeted against a parallel intermolecular G4 assembled from the ciliated protozoan Stylonichia lemnae telomeric sequence, providing the strongest evidence for G4 existence to date for the G4 in vivo. Two Ab fragments that could particularly recognize parallel or parallel/anti-parallel quadruples were produced; they were classified as Sty 3 and Sty 49, respectively. In the vegetative Stylonichia, Sty 49 produced a robust response in the macronucleus but not the micronucleus, whereas Sty 3 Ab was unable to produce a signal in vivo. Based on the precise 16 nt length of the telomeric overhang in this particular species, the authors concluded that the only dimeric G4 seen in vivo is an antiparallel one. This does not, however, rule out the possibility that parallel G4s exist in different species or at different stages of the life cycle.

Paeschke et al. [313] provided additional support for the G4 structure's in vivo data. RNA interference was employed by the authors to show that telomere-end-binding proteins, aTBP and bTBP, are required for G4 assembly in vivo, as demonstrated by the absence of response with the Sty 49 antibody in Stylonichia macronuclei upon removal of either protein. Additionally, they showed that the unfolding of the G4 requires cell-cycle-dependent kinase, Cdk2, phosphorylation of the C-terminal portion of bTBP, since inhibiting Cdk2 phosphorylation in vivo produced Sty 49 signal at the replication band of Stylonichia macronuclei, a region that had not previously shown any G4 signal. Thus, it was deduced that bTBP phosphorylation mediates the resolution of G4 DNA, which is required during telomere creation. The authors speculate that the anti-parallel G4 plays a part in telomere capping mechanisms based on this theory.

Duquette and colleagues [314] have conducted an intriguing investigation that supports the theory that a cell can include a G4 structure. Through the propagation of a plasmid harboring a G-rich insert generated from the TTAGGG human telomeric

repeat, they have developed a method for the inducible production of intramolecular G4 DNA in live E. Coli cells. Using electron microscopy, they saw the creation of "G-loops" upon transcription induction. During transcription, the non-template G-rich strand contained G4 DNA, whereas the C-rich strand created a stable RNA–DNA hybrid. By testing with proteins that have a strong affinity for G4 DNA, such as GQN1 nuclease and the previously mentioned shortened derivative of nucleolin, the validity of the G4 was confirmed.

In addition, G4 structure in human chromosomes has been identified using a radiolabelled G4 ligand 3 H-360A. The creation of metaphase spreads of human normal versus tumor cells cultivated in the presence of this ligand, followed by autoradiography, allowed for the detection of the structure. 3 H-360A attached to chromosomal terminal regions preferentially [315].

Because of their structural variety, G4s may be used to a biological system's advantage. Various factors could support a change in conformation: Variations in the cell's ionic environment or in the concentration of DNA locally may both have an impact on the kind of quadruplex that emerges [316,317]. The latter can be accomplished by the previously mentioned chaperone-like proteins or by topological reorganization of the chromosomes, as has been reported during meiotic bouquet formation which is a configuration that is seen in nearly all animals in which their telomeres are arranged [318,319].

Three different roles for G4s at the telomere have been proposed. First role is to prevent inappropriate telomere elongation, an anti-parallel intramolecular G4 or its hybrid parallel/anti-parallel counterpart may be used to protect the single-stranded overhang from telomerase or prevent the G-overhang of the chromosome end from nucleolytic attack [303]. The alternate lengthening of telomeres (ALT) method of telomere maintenance relies on recombination-mediated DNA replication of telomeres, which may be inhibited by intra-telomeric G4 formation [320]. In this instance, the quadruplex may serve as a fundamental component of the T-loop structure [321,322] or as an alternative to it [323]. The latter one is an appealing proposal since it offers a substitute for the generally accepted but purely theoretical

theory that G4 binding protein, Pot1, binds the D-loop, the unpaired section of the G-strand. In species where intramolecular folding is not possible, such as many ciliated protozoa, an antiparallel dimeric G4 can serve as preventive. These species have telomeres that have an extension length of less than four repetitions [312,313,324]. The second, in meiotic prophase I, parallel tetrameric G4smay promote intertelomeric interactions that may be implicated in the synapsis of sister chromatids. The third one is that the parallel/anti-parallel hybrid configuration of intra-telomeric G4 creation can encapsulate telomeric DNA by allowing for end-to-end oligomerization, resulting in considerable G-overhang compaction [325–327].

With the increasing number of studies, the studies involving the detection of telomerase or the telomeric DNA in vitro has also increased considerably.

1.3.3. Optical Detection Platforms Telomeric DNA and Telomerase activity Detection

Indefinite cell division, which is correlated with telomere maintenance mechanism activation, is a feature common to cancers in general. Since most cancer cells exhibit telomerase reactivation, it can be used as a universal biomarker and possible therapeutic target for cancer diagnosis, prognosis, and treatment [328,329]. As previously addressed, telomerase and telomeres have a critical role in several illnesses, according to increasing clinical data [330]. Thus, the identification and detection of human telomeric DNA and/or telomerase activity in the cell have gained significant attention in the last decades. There are many methods reported for the detection of human telomeric DNA or telomerase activity in vitro including SERS [331], photoelectrochemistry [332], differential pulse voltammetry [333], spectrophotometry [334] and fluorometry [335]. Among them, fluorometric and colorimetric detection platforms can be considered as the most facile and straightforward methods.

1.3.3.1. Fluorometric Detection Platforms

Fluorescent biosensor systems are widely utilized in biological and biomedical applications, such as in vivo imaging and solution-based assays, due to their rapidity and sensitivity [336]. They are also widely used to detect human telomeric DNA and

telomerase activity. For instance, Jha and Mayuri [337] developed a copper-curcumin-cysteine (Cu-CC) probe. They employed this probe to detect several G4 DNAs. The regeneratable fluorescence sensing probe's "turn-off–on" principle served as the basis for the system. The system's LOD for human telomeric G4 was 15.8 nM, while its LDR ranged from 60 to 160 nM. Furthermore, a CRISPR/Cas12a-based droplet digital hyperbranched amplification enhanced approach for the quantitative detection of telomerase activity (ddHECTelo) was developed by Luo et al [335]. Utilizing the ddHECTelo, they were able to measure telomerase activity at the concentration of 6.3 MCF-7 cells/μL with 6.3–125 MCF-7 cells/μL detection limit. Other methods to sense the either human telomeric DNA or telomerase activity were listed in Table 1.

Table 1. Fluorometric detection platforms for human telomeric DNA and telomerase activity.

Biomolecule	**Detection Method**	**Detection Platform**	**LDR**	**LOD**	**Year**	**Reference**
Human telomeric G4	Fluorescence	copper-curcumin-cysteine	60–160 nM	15.8 nM	2023	[337]
Telomerase Activity	Fluorescence	ddHECTelo[a]	6.3–125 MCF-7 cells/μL	6.3 MCF-7 cells/μL	2023	[335]
Telomeric DNA	Fluorescence	hollow spherical COF-100%N_3[b]	0.05–10 nM	50 pM	2022	[338]
Telomeric Dimeric G4	Fluorescence	HPTA-1[c]	0–2.4 μM	0.18 μM	2021	[339]
Human Telomeric G4	Fluorescence	Hemin@Ce-MOF[d]	1.6–39.7 nM	665 pM	2021	[340]
Telomerase Activity	Fluorescence	CRISPR/Cas 12a	57-5.7×10^5 cells/mL	57 cells/ mL	2021	[341]
Telomerase Activity	Fluorescence	CHA-DNAzyme[e]	10-1000 cells/mL	7 cells/mL	2021	[342]
Telomerase Activity	Fluorescence	DNA tweezer	280- 2850 cells/μL	141 cells/μL	2018	[343]
Human Telomeric G4	Fluorescence	TO-BTZ[f]	0-25 μM	0.8 μM	2018	[344]

Table 1 (continued)

Human Telomeric G4	Fluorescence	Tetrazolyl pyrene nucleoside	-	-	2017	[345]
hTR-DNA	Fluorescence	Hairpin DNA	0.001-1 nM	0.3 pM	2017	[346]
Telomerase Activity	Fluorescence	TS[g] primer modified GNPs	10-1000 cells	1 cell	2017	[347]
Telomerase Activity	Fluorescence	DNA modified GNPs	50-1000 cells	33 cells	2017	[348]
Telomerase Activity	Fluorescence	CCP-based FRET[h]	30-1000 cells/mL	5 cells/mL	2017	[349]
Telomerase Activity	Fluorescence	SDR[i]	1-3000 cells	1 cell	2016	[350]

[a] ddHECTelo-droplet digital hyperbranched amplification enhanced approach for the quantitative detection of telomerase activity [b]COF-100%N3- Covalent organic frameworks and polycondensation of the nonplanar 2-(2-azidoethoxy)ethoxy group, [c] HPTA-1-4-(2-(naphthalen-2-ylmethylene)hydrazinyl)-*N*-phenyl-6-(pyrrolidin-1-yl)-1,3,5-Triazin −2-amine, [d] Hemin@Ce-MOF-Hemin conjugated fluorescent cerium-based metal-organic framework, [e] CHA-DNAzyme-Catalytic hairpin assembled DNAzyme, [f] TO-BTZ- benzothiazole conjugated thiazole orange, [g] TS-telomerase substrate, [h] SDR- strand displacement reaction, [i] CCP-based FRET-Cationic conjugated polymer-based fluorescence resonance energy transfer

1.3.3.2. Colorimetric Detection Platforms

Colorimetry can be considered as the most widely used biosensing approach because of its unique benefits, which include affordability, accessibility, and simplicity. Colorimetric analysis in particular works well for point-of-care detection since the results are visible to the naked eye [351]. By exploiting these advantages of colorimetric sensing methods, several studies were conducted to detect telomerase activity or telomeric DNA. For example, Qu et al. [352] developed a colorimetric method to determine telomeric DNA, monitoring G4, and dsDNA structure through the interaction of silver nanoclusters (AgNCs), GNPs, and telomeric DNA. They observed that the estimated detection limits for telomeric DNA consisting of 10, 22, 40, and 64 nucleotides, were 1.41, 1.21, 0.23, and 0.22 nM, respectively. Additionally, the limit of detection (LDR) of the system for telomere DNAs was 5-110 nM, 3-50 nM, 1-40 nM and 0.6-15 nM, in the same order. Cheng and coworkers [353] utilized lateral flow and exponential amplification reaction assays (LFR-EXPAR) to develop a naked-eye visible assay for telomerase activity. HybriDetect lateral flow dipsticks enabled them to observe the LFR-EXPAR test results visually. They reported that the

system's LOD was 4 HeLa cells and dipsticks allowed them to observe telomerase activity in the range of 4 to 400 HeLa cells.

Several other colorimetric techniques reported for detection of human telomeric DNA and telomerase activity were tabulated in Table 2 and

Table 3. To the best of our knowledge in recent years, although there are several studies of fluorometric platforms to detect telomeric DNA, not many examples of colorimetric detection platforms were found.

Within this thesis, a colorimetric method based on the CTAB-capped GNRs has been developed for the detection of telomeric DNA in vitro, mainly due to its simplicity, affordability and accessibility and absence of such platform in the literature.

Table 2. Previously reported colorimetric detection platforms for human telomeric DNA

Biomolecule	Detection Method	Detection Platform	LDR	LOD	Year	Reference
Telomere DNA (consisting of 10, 22, 40, and 64 nucleotides)	UV-Vis Spectroscopy	AgNCs[a]	5-110 nM, 3-50 nM, 1-40 nM and 0.6-15 nM	1.41, 1.21, 0.23, and 0.22 nM	2023	[354]
Human telomerase RNA	UV-Vis Spectroscopy	CHA[b]-propelled 3D DNA amplifier	0–50 nM	41 pM	2020	[351]

[a]AgNCs - Silver nanoclusters, [b] CHA- Catalyzed hairpin assembly

Table 3. Previously reported colorimetric detection platforms for human telomeric DNA and telomerase activity.

Biomolecule	Detection Method	Detection Platform	LDR	LOD	Year	Reference
Telomerase Activity	UV-Vis Spectroscopy	P-DNANS[a] controlled GNP	30-2400 cells	10 cells	2023	[354]
Telomerase Activity	Cas9-mediated TL-LFA[b]	GNPs	-	1 Hela cells	2021	[355]

Table 3 (continued)

Telomerase Activity	UV-Vis Spectroscopy	GNPs	15-500 cells/μL	8 cell/ μL	2021	[356]
Telomerase Activity	Paper-based	GNPs seeding and enlargement	6–2500 cells	6 cells	2020	[357]
Telomerase Activity	UV-Vis Spectroscopy	GNBPs[c]	5-1000 HeLa cell	1 HeLa cells	2019	[358]
Telomerase Activity	UV-Vis Spectroscopy	DNA ends-based silver nanoparticle	1-50 cells/μL	1 cell/μL	2018	[334]
Telomerase Activity	UV-Vis Spectroscopy	GNRs	20-500 HeLa cells	5 HeLa cells	2018	[359]
Telomerase Activity	UV-Vis Spectroscopy	GNPs	50–1000 cells	25 cells	2018	[360]
Telomerase Activity	Spectrophotometer	TMB[d]	10-1000 HeLa cells	5 HeLa cells	2017	[361]
Telomerase Activity	UV-Vis Spectroscopy	GNRs	200-15000 HeLa cells/mL	90 HeLa cells/mL	2017	[238]
Telomerase Activity	UV-Vis Spectroscopy	H-GNs[e]	100 to 2300 HeLa cells/mL	60 HeLa cells/mL	2017	[362]
Telomerase Activity	UV-Vis Spectroscopy	Primer-modified GNPs	0-200 HL-60 cells/mL	29 HL-60 cells/mL	2016	[363]

[a] P-DNANS- palindromic DNA nanospheres, [b] TL-LFA- triple-line lateral flow assay, [c] GNBPs-Gold nanobipyramids, [d] TMB-3,3′,5,5′-Tetramethylbenzidine, [e] H-GNs- hemin-graphene nanomaterial

1.4. Aim of the Thesis

As previously mentioned, one characteristic shared by all malignancies is infinite cell division, that is linked to the activation of the telomere maintenance mechanism. Telomerase reactivation is present in the majority of cancer cells, making it a useful biomarker for cancer diagnosis, prognosis, and therapy [328,329]. As was already mentioned, there is growing clinical evidence that telomerase and telomeres are important in many diseases [330]. Therefore, throughout the past several decades, there has been a noticeable increase in interest in identifying and detecting human telomeric DNA and/or telomerase activity both in vivo and in vitro. We proposed that by utilizing aforementioned advantages of GNRs, a more economic, facile and straightforward sensing method for human telomeric G4 can be developed.

CHAPTER 2

MATERIALS AND METHODS

2.1. Reagents and Chemicals

All chemicals and reagents were used as received without further purification. Millipore water (Milli-Q, 18.2 MΩ cm^{-1}) was used in the preparation of all the buffers, samples, and solutions. Gold (III) chloride trihydrate ($HAuCl_4.3H_2O$, 99.9%), L-ascorbic acid ($C_6H_8O_6$, 99%), potassium chloride (KCl, 99.6%), potassium phosphate monobasic (KH_2PO_4, 99.9%), potassium phosphate dibasic (K_2HPO_4, >99.0%) were purchased from Sigma-Aldrich (St. Louis, MO). Sodium borohydride ($NaBH_4$, 96%), and silver nitrite ($AgNO_3$, 99.5%) were obtained from Merck (Darmstadt, Germany). Hexadecyltrimethylammonium bromide ($CH_3(CH_2)_{15}N(Br)(CH_3)_3$, >97.0%) was bought from ISOLAB (Wertheim, Germany). Hydrochloric acid (HCl, 35.4%) was obtained from BDH Chemicals (Poole, United Kingdom). All oligonucleotides given in Table 4 with their extinction coefficients were purchased from Integrated DNA Technologies (IDT, Dresden, Germany). Extinction coefficients used were supplied by IDT.

Table 4. Sequences used in this study and their extinction coefficients.

NAMES	SEQUENCES	EXTINCTION COEFFICIENT at 260 nm (L/(mole. cm)
Tel24	5'-TTA GGG TTA GGG TTA GGG TTA GGG-3'	244600
Tel24m1	5'-TT GGG TTA GGG TTA GGG TTA GGG A-3'	244300
Tel24m2	5'-TTA GTG TTA GTG TTA GTG TTA GTG-3'	239000

Table 4 (continued)

Tel24m3	5'-TTA GGG TTA TTT TTA GTG TTA GTG-3'	235200
Tel24m4	5'-TTA TGG TTA TGG TTA TGG TTA TGG-3'	236600
Tel24m5	5'-TTT GGG TTT GGG TTT GGG TTT GGG-3'	221000
Tel24comp	5'-CCC TAA CCC TAA CCC TAA CCC TAA-3'	220400
Pu_{22}	5'-CGG GGC GGG CCG GGG GCG GGG T-3'	178400
VEGF	5'-GGG CGG GCC GGG GGC GGG GTC CCG GCG GGG CGG GAG-3'	338200
K-RAS	5'-GGG AAG AGG GAA GAG GGG GAG-3'	232800
BCl-2	5'-AGG GGC GGG CGC GGG AGG AAG GGG GCG GGA GCG GGG C-3'	368200
C-MYC	5'-TGG GGG AGG GGT GGG GGA GGG GTG GGG GAA AGG G-3'	352500
Her2/Neu1	5'-AGG AGA AGG AGG AGG TGG AGG AGG AGG GC-3'	315900
RB	5'-CGG GGG GTT TTG GGC GGC-3'	164700
dA_{32}	5'-AAA AAA AAA AAA AAA AAA AAA AAA AAA AAA AA-3'	387400
dT_{32}	5'-TTT TTT TTT TTT TTT TTT TTT TTT TTT TTT TT-3'	259800

2.2. Instrumentation

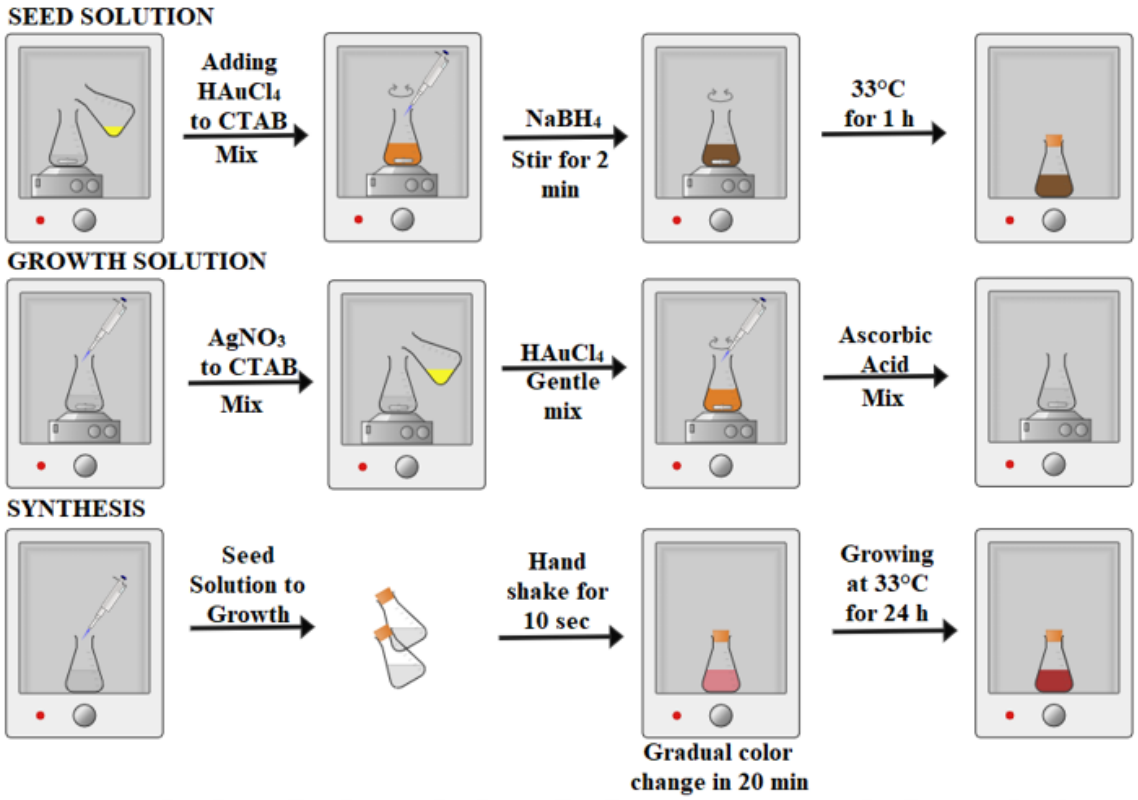
To record the absorption spectra of the samples a double beam JASCO V-730 (Easton, MD, USA) UV–vis spectrophotometer was used within the wavelength range of 350 to 1000 nm using a 10 mm quartz cell. A High Contrast transmission electron microscopy (CTEM), FEI Tecnai G2 Spirit BioTwin (at METU Central Laboratory), was utilized for the size and morphological characterization of the synthesized GNRs before and after addition of Tel24 under the optimized conditions. The CTEM analysis was performed at an acceleration voltage of 120 kV. For the preparation of the samples before CTEM analysis, commercially available carbon-coated copper grids were used by drop-casting the test solutions onto their surfaces and allowing solvent to evaporate at room temperature. A Zetasizer Nano-ZS equipment (Malvern Instruments Ltd, Malvern, UK) was employed for the Dynamic light scattering (DLS) and zeta (ζ)-potential measurements. For this purpose, 1.0 mL of the synthesized colloid (in the

absence and presence of the target analyte) was subjected to a particle size analysis instrument, and the hydrodynamic sizes were acquired by cumulant analysis of the autocorrelation data. Zeta-potential values were determined from electrophoretic mobility values to predict the nature of the electrostatic potential near the surface of the particles. Mean values were obtained from three independent measurements. Thermal denaturation studies of nucleic acid structures were performed from 15 to 95°C with a 2°C/min increment using a Cary 8454 UV–vis photodiode array spectrophotometer equipped with an Agilent 89090A Peltier unit (Santa Clara, CA, USA). A J-1500 spectropolarimeter equipped with CTU-100 Circulating Thermostat Unit (Easton, USA) was utilized to conduct Circular dichroism (CD) measurements in the wavelength range of 200 to 550 nm with 100 nm/min scanning speed and 4-sec data integration time. Digital photos were captured by iPhone 14 Pro smartphone. The UV-Vis and CD spectra were analyzed by using Igor Pro (WaveMetrics, Lake Oswego, OR, USA) unless otherwise mentioned.

2.3. Synthesis of GNRs

GNRs were synthesized using a slightly modified seed-mediated growth method originally proposed by Nikoobakht & El-Sayed [63]. As represented in Scheme 1, to prepare the seed solution, 5.0 ml of 0.1 M CTAB and 5.0 ml of 5.0 mM $HAuCl_4$ solutions were mixed under stirring at 400 rpm for 1 min. Then, 600 µL of freshly prepared ice-cold $NaBH_4$ solution (0.01 M) was added dropwise to the above mixture. The resulting solution exhibits a light brown hue. Following vigorous stirring for another 2 min, the solution was incubated at 33°C for 1 h. To prepare the growth solution, 2.5 mL of a freshly prepared $AgNO_3$ (6.0 mM) solution was added to 125 mL of 0.1 M CTAB solution under a continuous string. Then, 125 mL of 1.0 mM $HAuCl_4$ solution was added slowly. After a gentle mixing, the solution color turned orange. Next, 1375 µL 0.1 M L-ascorbic acid (AA) solution was added, and a colorless growth solution was obtained. Finally, 300 µL of the seed solution was added to 250 mL of growth solution. The mixture was shaken for 10 s and kept undisturbed at 33°C for 24 h to complete the growth of nanorods. A gradual color change was observed 20 min after shaking. The whole procedure was performed at 33°C incubation. The final

product was centrifuged twice at 9000 rpm for 20 min to remove excess CTAB and remaining reagents. GNRs were redispersed in Milli-Q water and the stock was stored at +4°C.



Scheme 1. Schematic representation of the synthesis of GNRs.

2.4. Preparation and Characterization of Nucleic Acid Solutions

The nucleic acid solutions were all prepared at a concentration of 2.3 µM in a 25 mM K-phosphate buffer (pH=7.0) containing 70 mM KCl. The prepared solutions were annealed by heating them to 95°C in the water bath for 5 min and allowing them to cool down to room temperature overnight. Double and triple-stranded nucleic acid samples were prepared by adjusting the ratios as needed to achieve a final concentration of 2.3 µM.

Thermal denaturation studies were conducted with 2 µM Tel24 and 2 µM Tel24 in the presence of 28 mM HCl and 0.01 M CTAB. CD measurements were performed with

the same solutions at 15°C, 60°C, and 80°C after 10 min of incubation. All samples were prepared freshly prior to analysis.

2.5. Colorimetric Detection of Tel24

For colorimetric detection of Tel24, 10.0 µL of 1.0 M HCl was added to 250 µL of 0.01 M CTAB-containing GNRs. Followingly, 100 µL of 2.3 µM Tel24 G4 DNA structure was added to the solution, and upon vortex-mixing, the mixture was incubated at 60°C for 10 min. The color change of the system was monitored using both visual observation and UV-Vis spectroscopy. In addition to testing various experimental conditions, the system's selectivity and sensitivity were assessed using UV-Vis spectroscopy. The impact of CTAB concentration in the solution was monitored under the following conditions: 0.64 µM Tel24, 28 mM HCl, 60°C incubation temperature, and a 10-min incubation time. To measure and optimize the required HCl concentration, various concentrations of HCl were added to the system while other conditions were kept constant. Next, the effect of incubation temperature was observed while keeping the CTAB and HCl concentrations constant and maintaining a 10-min incubation time. Finally, the incubation time was varied under optimized conditions to assess its impact on the system.

CHAPTER 3

RESULTS AND DISCUSSION

3.1. Colorimetric Detection of Tel24

The response of GNRs upon the addition of Tel24 in the presence of HCl was observed with UV-Vis spectroscopy and visual inspection (Figure 17). The synthesized GNRs exhibited a red color and a transverse LSPR at 515 nm and longitudinal LSPR at 715 nm (the black spectrum). Upon addition of HCl and Tel24, the solution's color changed from red to purple and eventually to pale blue. As mentioned earlier, changes in the color of the GNR solution can be resulted from aggregation and/or alteration in GNRs shape or size [166]. As depicted in Figure 17, neither HCl nor Tel24 induced a color or spectral change (blue and green dotted lines) individually. Nevertheless, when Tel24 was added in the presence of HCl, a noticeable color change occurred after a 10-min incubation at 60°C. The observed color change was additionally monitored using UV-Vis spectroscopy (red spectrum), revealing that the transverse LSPR shifted to 534 nm, while the longitudinal LSPR shifted to 675 nm. These results suggested that the contribution of both the aggregation and the etching mechanisms to the observed spectral changes in the developed probe [162,176].

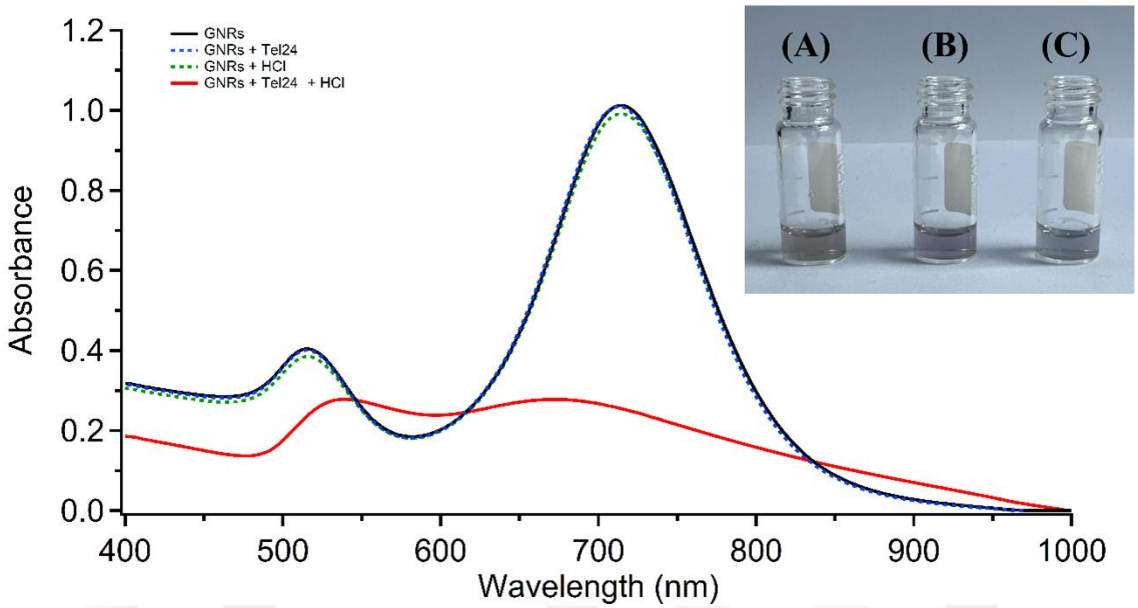


Figure 17. UV-Vis absorption spectra of GNRs probe (black line), GNRs + HCl (green dotted line), GNRs + Tel24 (blue dotted line), GNRs + Tel24+ HCl (reaction mixture upon the addition of Tel24 in the presence of HCl after 10 min incubation (red line)); Experimental conditions: [HCl]=28 mM, [Tel24]=0.64 µM, Temperature: 60°C. Inset: The digital photographs of the step-by-step color change of GNRs after the addition of Tel24 under the optimized conditions. (A): Before incubation, (B): 6 min of incubation, (C): 10 min of incubation.

3.2. Characterization

To characterize the synthesized GNRs and assess the impact of the introduction of Tel24 and HCl on the GNRs, TEM, DLS, and zeta potential analyses were performed for both the GNRs and the reaction mixtures after 6 and 10 minutes of interaction (after the addition of Tel24 and HCl). Followingly, to understand the structural change of the G4 target DNA structure in the presence of HCl and CTAB, thermal denaturation studies and CD measurements were performed.

As expected, CTEM measurements indicated that GNRs show colloidal dispersity (Figure 18A, B, C) which was consistent with the literature [63]. Scale bars for Figures 18A and 18B are 50 nm and for 18C, is 20 nm. According to intensity results of DLS measurements width of GNRs was 2.12 ± 0.18 nm and length of GNRs was 46.13 ±

4.00 nm (Figure B 1 and Table B 1). As can be seen from Figures 18D, E, F, after being treated with Tel24 under acidic conditions for 6-min, GNRs showed size decrement from tips and heterogeneity due to etching. GNRs are more susceptible to etching on their tips since tips are less protected by CTAB and their length decreases as they are being etched [364]. Under these conditions, slight aggregation was also witnessed. However, after 10 min of incubation, particle aggregation was dominant and monitored more clearly (Figure 18G, H, I). Figure 19 and Table 5 illustrate the size distribution by intensity and zeta potential measurements of GNRs and reaction mixture after a 6-min and 10-min incubation at 60°C. The DLS measurements showed that synthesized GNRs were 46.13 ± 4.00 nm in size (Figure B 1 and Table B 1). After 6-min and 10-min of incubation, their size increased to 83.54 ± 13.41 nm (Figure B 2 and Table B 1) and 156.73 ± 12.93 nm (Figure B 3 and Table B 1), respectively. It is known that increasing size in DLS measurements indicates aggregation [365]. In 2013, Kanjanawarut et al. [366] conducted a study about aggregation of GNRs by using UV-Vis spectroscopy and DLS measurements. They reported that with the introduction of negatively charged citrate ions, CTAB-capped GNRs aggregated, and this results sensitively monitored with DLS. They also emphasized that as citrate concentration increased, particle sizes (obtained via DLS) increased. Similar to the citrate ions, the negatively charged backbone of the nucleic acids might be the main contributing factor to the aggregation of GNRs. In addition, it has been previously reported that the small size distribution obtained between 5-7 nm is not an actual size distribution for the GNRs. It was reported to be due to the rotational diffusion of the non-spherical nanorods [367]. Khlebtsov and Khlebtsov clearly stated that the rotation of nonspherical strongly scattering particles with sizes larger than 30-40 nm results in a false peak between 5-10 nm [368]. Meaning that the size obtained from the CTEM measurements might be a better representation of the GNRs obtained here from DLS.

In our proposed system, the observed aggregation after 6-min incubation was slightly less than the aggregation observed after 10-min incubation time. The mean zeta potential value of the GNRs in the probe solution was measured as +34.6 ± 5.59 mV. After the addition of Tel24 over the 6 min incubation, this value was decreased to +26.9 ± 7.08 mV and increased to +47.5 ± 6.73 mV after 10-min incubation. The

unmodified GNRs are expected to have a positive zeta potential value due to the positively charged cetyltrimethylammonium group of CTAB [369]. The decrease in the zeta potential value is a potential indicator of the size reduction of GNRs upon etching. Alex and colleagues [192] conducted research about shape transitions of dumbbell shaped GNRs to particles and rods upon addition of hexavalent chromium. They stated that rise in the chromium concentration caused decrease in GNRs size and along with their size their surface potential also decreased. They explain this by the fact that as GNRs got smaller, fewer CTAB molecules were present on their surface, which resulted in a decrease in their surface positive charge [192].

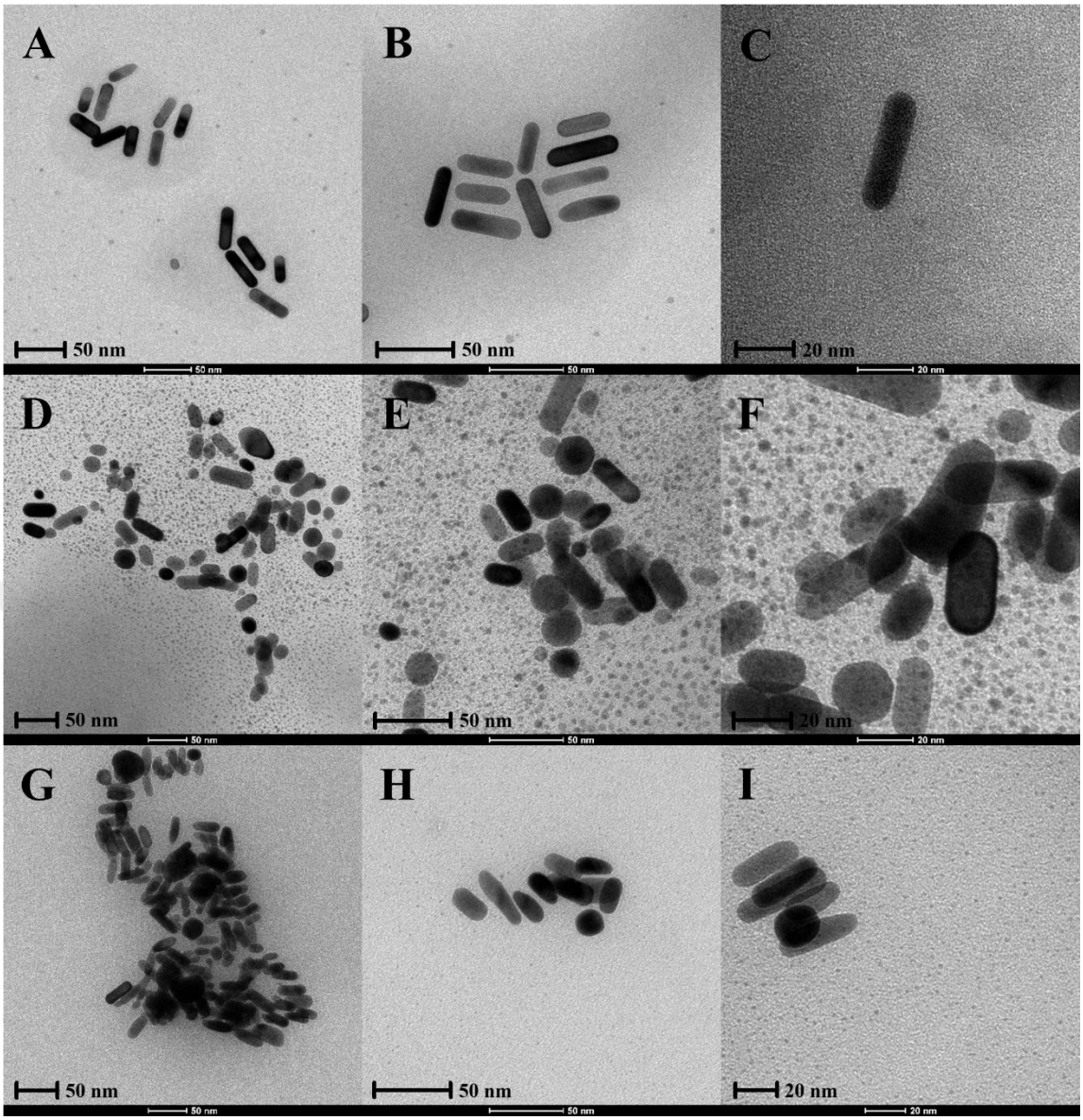


Figure 18. TEM micrographs of GNRs (A, B and C), GNRs after 6 min (D, E and F) and 10 (G, H and I) min of incubation at 60°C after the addition of Tel24 and HCl at different magnifications. Experimental conditions: [HCl]=28 mM, [Tel24]=0.64 μM.

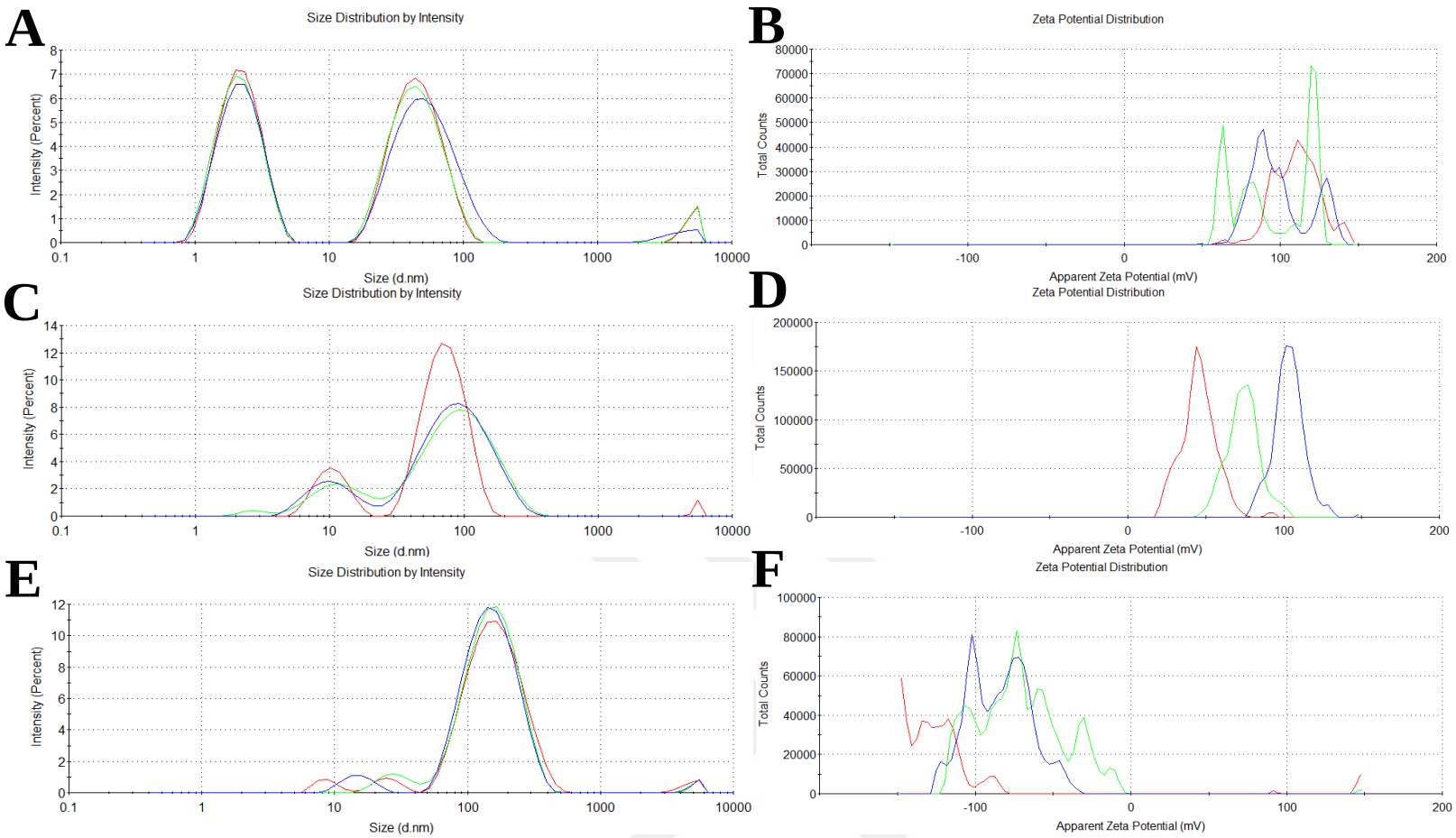


Figure 19. Dynamic Light Scattering and Zeta Potential measurements of GNRs (A and B), GNRs after 6 min of incubation (C and D) and10 min of incubation (E and F) at 60°C after the addition of Tel24 and HCl. Experimental conditions: [HCl]=28 mM, [Tel24]=0.64 μM.

Table 5. Results of DLS and Zeta potential measurements of 0, 6 and 10 min of incubations

Time	Intensity Size Peak 1	Intensity Size Peak 2	Zeta Potential
0 min	2.12 ± 0.18 nm	46.13 ± 4.00 nm	+34.6 ± 5.59 mV
6 min	10.63 ± 0.92 nm	83.54 ± 13.41 nm	+26.9 ± 7.08 mV
10 min	22.75 ± 6.41 nm	156.73 ± 12.93 nm	+47.5 ± 6.73 mV

To assess the stability of target G4, thermal denaturation studies of Tel24 in the absence and presence of HCl and HCl+CTAB were performed. Thermal denaturation temperatures (T_m) were obtained from the middle point of the sigmoid curve of absorbance vs. temperature graphs after measuring the absorbance change at 295 nm with respect to temperature [370]. T_ms of Tel24, Tel24+HCl and Tel24+HCl+CTAB were found as 59°C (Figure C 1), 69°C (Figure C 2) and 69°C (Figure C 3), respectively (Table C 1).

A through survey of the literature reveals that the increase of the melting temperatures indicates the stabilization of G4 structures [371]. Accordingly, we observed that the increase in T_m of Tel24 upon the addition of HCl resulted in the stabilization of Tel24 G4 structure under our optimized acidic conditions. In the contrary, G4 DNA structures are known to be stable at physiological conditions [372] and low pH values can cause G4 destabilization [373,374]. Still, certain sequences are known to be able to from G4 structures at neutral to low pH values [374].

Additionally, Ho and Chang [375] studied the effect of reverse micelles (RM) on Hum22 ($AGGG(TTAGGG)_3$) structures. In potassium buffer, melting temperature of Hum22 was 50.3°C and in the presence of both CTAB and potassium buffer, the melting temperature were reported to increase to 75.5°C. They concluded that RM formed by CTAB increases the stability of G4. Being in a good agreement, in our proposed system, the increase of the T_m of G4 in the presence of HCl+CTAB can be assessed as a sign of the stabilization of the G4 structure.

For further investigation of structural change of Tel24, CD measurements were conducted at 15°C. G4 structures are known to have three different main topologies

known as parallel, antiparallel and hybrid [376]. These topologies show characteristic CD peaks. Parallel G4s possess maxima peak around 264 nm and minima peak around 245 nm. Antiparallel structures are known to have a positive peak at 295 nm and a negative peak at 260 nm. Hybrid G4s exhibit a positive peak around 295 nm, a positive shoulder peak at 260 nm and a negative peak around 245 nm [377]. Accordingly, Tel24 had hybrid structure before any treatment. As depicted in Figure D 1, Tel24 had a maximum ellipticity of 8.5873 mdeg at 289 nm, a shoulder peak with 5.6034 mdeg at 271 nm and minima peak with -1.9753 mdeg at 237 nm. However, in the presence of HCl, Tel24 mostly lost its topology. On the other hand, when both CTAB and HCl were present, Tel24 was observed to adopt a parallel structure with +11.679 mdeg at 264 nm and -5.3952 mdeg at 243 nm (Figure D 1).

In 2013, Yan and colleagues [373] carried out a study to monitor the pH-driven conformational shift of G4s. In their study, the change in G4 conformation was observed by CD. Human telomeric G4, HTel $(GGGTTA)_3GGG$), exhibited a conformational shift from hybrid to antiparallel form when annealed at an acidic pH in a K^+-containing environment. The pH changed step-by-step from 7 to 4.5, and the G4 structure was disrupted at even lower pH values. Its structure collapsed completely when it was annealed at a pH lower than 3.5. However, G4s at acidic pH were highly stable after they were produced. When they reported that other types of naturally occurring G4 such as bcl-2, c-myc, RET, KRAS and ILPR, they did not display such conformational change. Since all these G4s contain the same three tetrad core, they suggested that this topology conformation may result from the presence of a certain loop sequence. G4s with the identical TTAGGG sequences were examined in order to test this theory. All of the examined G4s, except the tetramer G4 without loops, could be influenced by the pH change at various amounts. Rearranging the loops may have caused this topology modification, since the H^+ may have broken their interaction. They suggested that either partial protonation of A [378] (pKa is 4 [379]) caused this transition or water network [380]. In another study, Ho and Chang [375] investigated the effect of reverse micelles (RM) on Hum22 ($AGGG(TTAGGG)_3$) structures. In potassium buffer, melting temperature of Hum22 was reported to be 50.3°C and in the presence of both CTAB and potassium buffer melting temperature increased to 75.5°C.

Additionally, when they conducted the CD studies, they observed no conformation change of Hum22. They concluded that RM formed by CTAB increases the stability of G4 and did not cause conformation change.

Therefore, in our proposed platform, the conformation change of Tel24 from hybrid to parallel structure may be as a result of the presence of both HCl and CTAB in the system.

3.3. Optimization of the Detection Platform

To determine the optimal conditions for the developed colorimetric detection platform, the influence of certain parameters (CTAB and HCl concentrations, time, temperature) that affect the sensing performance of GNRs was investigated. The decision for optimal conditions was based on the peak shift (in nanometers, nm). CTAB, by reducing the Au^{+}/Au reduction potential, is known to promote the redox process and enhance the etching of GNRs [168]. Wang et al. [179] conducted research to detect the presence of CTAB by using GNRs. They used Cu(II)-mediated H_2O_2 etching of GNRs in the study and found out that presence of CTAB significantly affects the etching of GNRs. After synthesis of GNRs, they centrifuged the solution and when they performed the experiment without any additional CTAB, they observed no etching. Therefore, they concluded that the effect of adsorbed CTAB on the surface of the GNRs was negligible. Furthermore, it was reported that by increasing the CTAB concentration, a remarkable blue shift in the longitudinal LSPR of GNRs was observed. Moreover, CTAB contributes to colloidal stability through repulsive electrostatic interactions [381]. Rostro-Kohanloo [382] published an article about targeting antibody and cell systems by GNRs and stabilization of GNRs. They realized that below certain concentration of CTAB, GNRs aggregates because CTAB affected their stability. Accordingly, for the optimization process, first the CTAB concentration was varied between 0 to 0.14 M in the presence of 28 mM HCl (incubation temperature and time were 60°C and 10 min, respectively). Correlating with UV-Vis spectra (Figure E 1), and the peak shift trend with increasing concentration (Figure 20A), it was determined that the highest and thus the optimum value for CTAB concentration was 0.01 M. The rate of etching of GNRs is shown to be influenced by the acid

concentration and reaction temperature previously [178]. In another study, Khani and colleagues [383] monitored the impact of pH on etching of GNRs to detect glutathione. They used a wide pH range (between 3 to 10) to investigate the pH effect. The highest peak shift obtained at pH=4 so, they observed that certain acid concentration was essential to develop a sensitive detection platform.

Accordingly, the effect of acid concentration on our system was monitored by varying the HCl concentration from 0 to 33 mM. After evaluating the peak shift trend (Figure 20B) and referring to UV-Vis absorption spectra achieved (Figure E 2), it was determined that 28 mM HCl yielded the maximum peak shift and was thus selected as the optimum condition for further experiments. Chen et al. [227] conducted a study for selective detection of Cu(II) ion and marked that as temperature increased, the absorption value decreased and after some point it reached a plateau. Thus, temperature is an important factor for sensitivity of the developed sensing system. Subsequently, the temperature effect was fine-tuned within the range of 30°C to 90°C. This particular range was chosen to account for the fact that the CTAB surfactant tends to crystallize below 30°C [384]. As displayed in Figure 20C, the highest peak shift was observed at 80°C. However, as can be seen in the absorption spectra of GNRs upon the addition of the target analyte under the optimized conditions (Figure E 3), the absorbance value of longitudinal LSPR of 60°C, was less than 80°C. Additionally, this high temperature that resulted in the highest peak shift can be possess a risk for the unfolding of target G4. As shown in Figure C 2, the Tel24 G4 structure in the presence of HCl and CTAB was almost completely unfolded at 80℃. On the other hand, it was mostly intact at 60°C. To see the structural stability of Tel24 in the presence of HCl and CTAB, CD spectra at 60°C and 80°C after 10-min incubations, were also collected. The CD spectra confirmed the unfolding of the parallel structure with increasing temperature (Figure D 3). According to the study published by Novoseltseva et al. [385] as G4 structures melt, they start to unfold and their corresponding ellipticity values decrease. Tel24 has a parallel topology with +11.679 mdeg at 264 nm and -5.3952 mdeg at 243 nm. During temperature optimization steps in our study, upon incubating at 60°C, the positive peak at 264 nm decreased to +7.5437 mdeg and the negative peak at 243 nm decreased to -3.5966 mdeg. However,

after 80°C incubation, peaks almost disappeared which was an indication of the unfolding of the structure. Based on these obtained results, the optimal temperature for the reaction was selected as 60°C.

Interaction time is another key factor for optimization of a sensing system. Fang and coworkers [216] have optimized time factor between 0 to 30 min for the detection of aflatoxin and monitored the system's response. They indicated that as required time for etching to occur increased, GNRs got smaller in size, but after 25 min of interaction no size change was observed. Similarly in our developed method, to determine the optimum reaction time, the response of the system after the addition of Tel24 was investigated in the range of 0-60 min as depicted in Figure 20D and Figure E 4. 10 min was selected as the optimum reaction time for the proposed system since the maximum peak shift value was observed at 10 min.

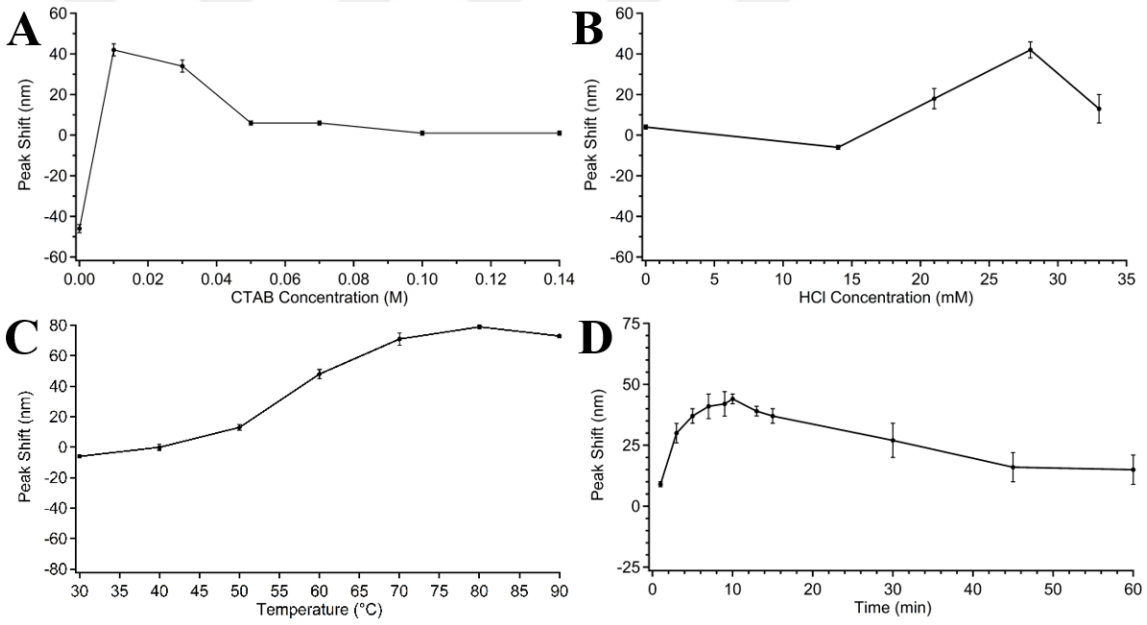


Figure 20. The effect of (A): CTAB concentration, (B): HCl concentration, (C): incubation temperature, and (D): reaction time on the response of GNRs to Tel24. The error bars indicate SD (n= 3).

3.4. Selectivity

To examine the selectivity of the system, 2.3 μM of various oligonucleotide structures including Tel24m1, Tel24m2, Tel24m3, Tel24m4, Tel24m5, Tel24comp, Pu22, VEGF, K-RAS, BCl-2, C-YMC, Her2/Neu1, RB, dA_{32}, dT_{32}, $dA_{32}dT_{32}$, $dA_{32}dT_{32}dT_{32}$ was added to the probe solution, instead of Tel24 under the optimized conditions and the response of the system was then monitored. Several modified oligonucleotide sequences (see Table 4) were used to observe the response of the system (referred to as Tel24mx). Tel24m1 is another human telomeric G4 sequence with a single base change and Tel24m2, Tel24m3, Tel24m4, Tel24m5 were designed by us and were meant to disturb G-quartet planes or loops by the change of certain nucleotides (Table 4). GGG's of Tel24 were replaced with GTGs in Tel24m2, and with TGGs in Tel24m4. In Tel24m3, only the second consecutive GGG of Tel24 was replaced by TTT. In Tel24m5, the changes were on the loops not on the GGG planes where TTA was replaced by TTT. Figure 21B shows that Tel24 displayed a noticeable 39 nm blue shift. Similarly, Tel24m1 caused a blue shift of 29 nm. Additionally, the introduction of VEGF, Her2/Neu1, and the mismatch 1 of Tel24 led to an approximately 13 nm blue shift. While other mismatch sequences and the complementary sequence did not cause any significant peak shift. Among the mismatches, the lowest response was obtained in the Tel24m3, as expected, with the whole consecutive GGG modified. A higher response was obtained with Tel24m2 and Tel24m4, where only one of the Gs is modified in a GGG plane, which might be an indication of the presence of a folded but destabilized G4. The modification of the loops was also observed to have a notable effect on the response of the probe.

In contrast, the single stranded dA_{32}, double stranded $dA_{32}dT_{32}$, and triple helical $dA_{32}dT_{32}dT_{32}$ induced a negative peak shift in the system. As seen in Figure 21A, these nucleic acid structures caused absorption decrease and peak broadening along with a slight red shift. This peak shift trend was associated with aggregation of GNRs [44]. Previously, it has been reported that the adenine has the greatest adsorption affinity towards Au among other DNA bases [386]. Although, adsorbed DNA can prevent aggregation of gold nanoparticles, it may also induce aggregation due to ionic

interactions [387]. Overall, our results clearly indicated the selectivity of the probe towards human telomeric G4 sequences (Tel24 and Tel24m1) and its possible use in the detection of human telomeric sequences.

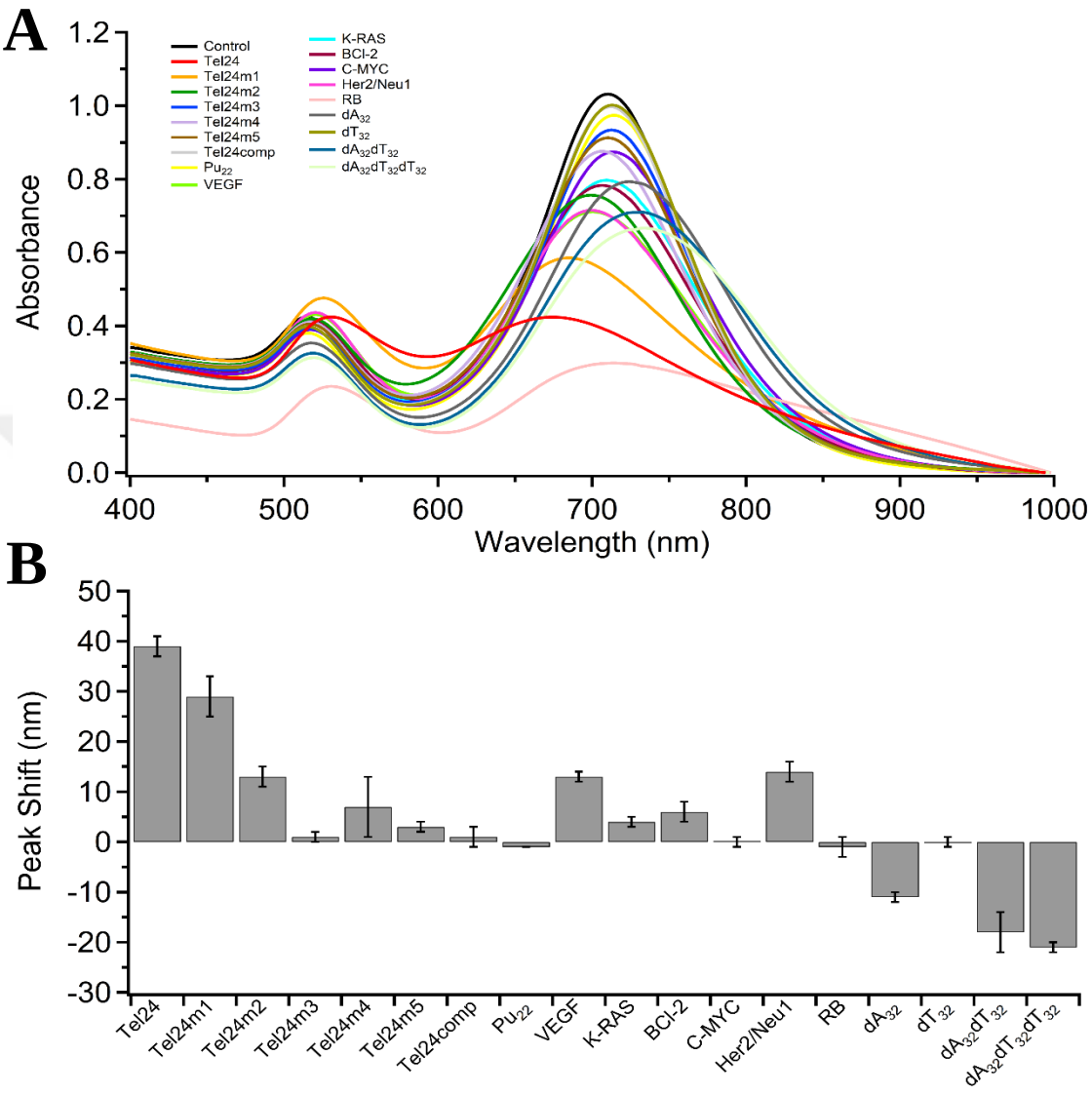


Figure 21. (A) Selectivity studies for unmodified GNRs probe based on the addition of each nucleic acid structure. (B) Bar graph depicting the peak shift vs. various under-examined nucleic acid structures for selectivity studies of unmodified GNRs probe, based on the addition of each nucleic acid structure under the specified experimental conditions: [CTAB]=0.01 M, [HCl]=28 mM, [DNA]=0.64 μM, Temperature: 60°C, Time: 10 min. The error bars indicate SD (n= 3).

3.5. Sensitivity

Finally, the sensitivity of the system was assessed by using UV-Vis spectroscopy upon the titration of Tel24 (within the range of 0.043-0.941 μM) onto the probe solution under the optimized conditions. As shown in Figure 22A the gradual addition of Tel24 resulted in a decrease and blue shift of the peak. The linear relationship between Tel24 concentration and peak shift is presented in Figure 22B. The system exhibited a linear dynamic range from 0.371 to 0.909 μM with an R^2 (Coefficient of determination) value of 0.9950. Limit of quantitation (LOQ) is defined as the last point of the calibration line [388]. LOQ of the system was determined to be 0.371 μM. The linear regression line equation was y=51.192[Tel24] – 15.602 and the LOD was calculated as 0.03 μM using the following equation:

$$LOD = 3.3 \times \frac{S_b}{a} \quad (1)$$

where Sb is the standard error of the intercept and a is the slope of the mean calibration curve [389]. Standard error of the intercept obtained from Igor Pro as 0.515.

Among the detection platforms for human telomeric G4 listed in Table 1 and Table 2, our strategy was found to provide a more straightforward, fast, and facile sensing method.

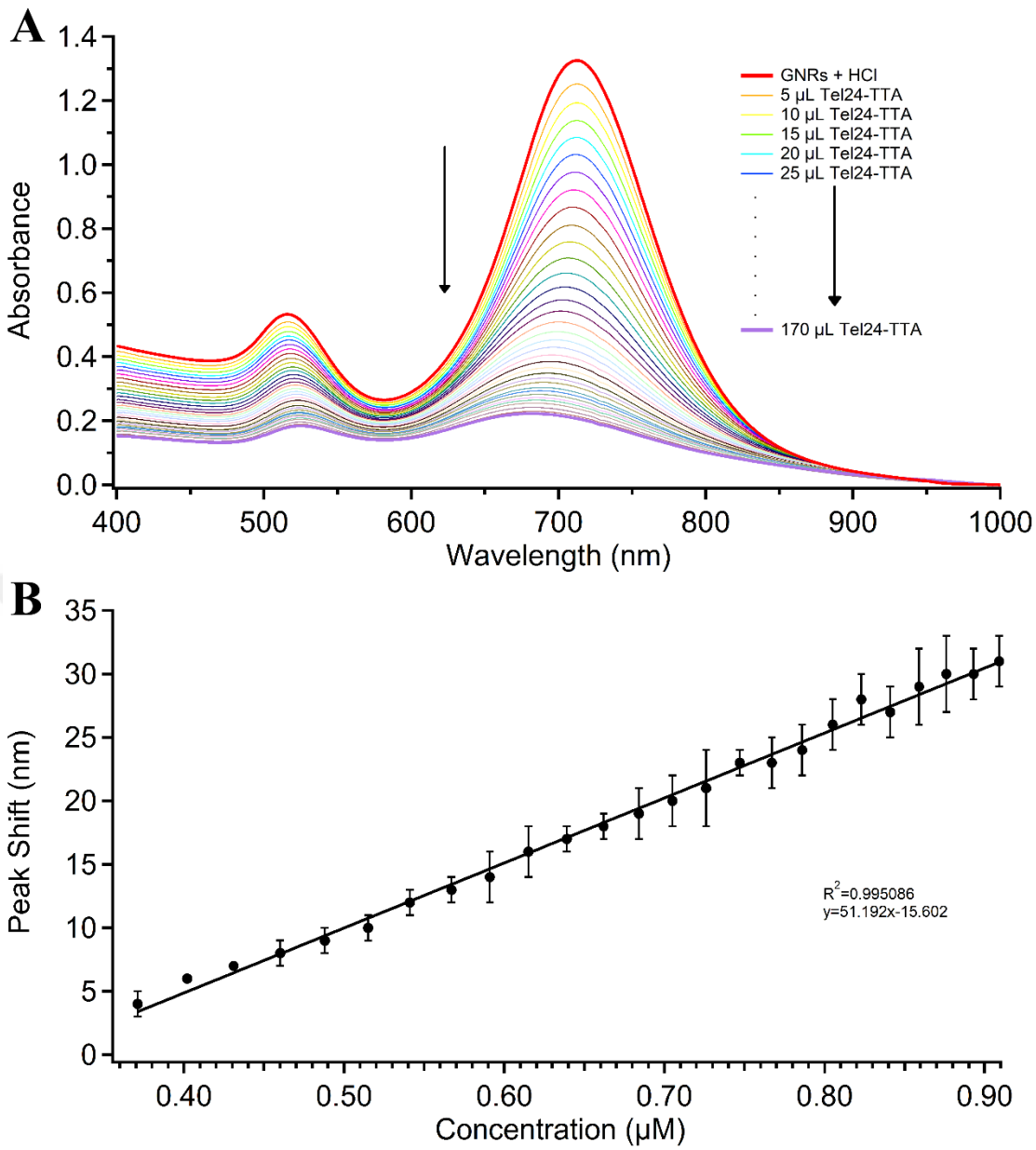


Figure 22. (A): UV-Vis absorption spectra of GNRs with increasing concentration of Tel24 under the optimized conditions. (B): Plot of peak shift vs. Tel24 concentration, Experimental conditions: [CTAB]=0.01 M, [HCl]=28 mM, Temperature: 60°C. The error bars indicate SD (n= 3).

3.6. Proposed Mechanism

Based on all the results obtained, it is certain that both the etching and aggregation of GNRs play a role in the detection of human telomeric G4 DNAs (Tel24 and Tel24m1).

The possible reasons that are thought to induce etching and aggregation are stated below.

Aggregation in the system can be explained mainly using the charge neutralization phenomena of the GNRs. CTAB is a quaternary amine, which has a positive charge on nitrogen accompanied by a solvated bromide as the counterion [144]. The positively charged CTAB-GNRs are known to be stable forming disordered assemblies in solution mainly due to the repulsions between the same charges [390]. The addition of the negatively charged DNA (the type of DNA is not given explicitly in the manuscript) is known to induce self-assembly at low DNA concentrations and aggregation at DNA high concentrations due to the partial charge neutralization and/or the stripping of the CTAB from the surface of the GNRs [391]. Moreover, Pan et al. [144] has shown that the addition of DNA resulted in the formation of the DNA−CTAB−nanorod complexes. At low concentrations of DNA, the negatively charged DNA is found to help to assemble the positively charged CTAB-GNRs using TEM, zeta potential measurements, and agarose retardation experiments. However, at higher DNA concentrations agglomeration and deposition of CTAB-GNRs were observed, which were mainly explained by the charge neutralization. Moreover, the acidic environment and the structure of the DNA are also shown to help to induce aggregation [392]. In their study using thiolated adenine-rich oligonucleotide, Sutter et al. have shown that GNRs will stay dispersed at neutral pH mainly due to the charge-charge repulsion between the negatively charged DNA strands on the GNRs. However, once the pH is lowered from pH 7.0 to pH 4.0, due to the protonation of the adenines and the formation of a double-stranded structure, assembly/agglomeration was triggered. Das et al. [393] have also shown that the secondary structure of the DNA affects the loading of thiolated DNA sequences onto CTAB-GNRs. They have shown that the conjugation efficiency of hairpin structures was higher than the dsDNA and the conjugation of dsDNA was higher than the ssDNA. Several studies with other types of nanoparticles have also shown that the sequence of DNA and its length do play a role in the colloidal behavior of the nanoparticles [394–397]. Interestingly, Peng et al. [397] found that among the nucleobases, guanine has been found to have the highest affinity toward counterions, which suggests to affect the DNA coating on

GNPs. Again Brown et al. [394] have shown that the adsorption of free nucleotides onto Au NPs by particle aggregation has shown an affinity order of G > C > A > T. And among the nucleotides T is always found to have the lowest affinity in other studies.

In our system, it was thought that the addition of the Tel24 sequence results in the formation of Tel24-CTAB-GNRs complexes, whereas the addition of Tel24 results in the neutralization, thus the aggregation of the CTAB-GNRs. The folding of the Tel24 and its sequence is also thought to play a role in the aggregation behavior similar to the aforementioned systems. Our results clearly state the effect of sequence and the secondary structure on the aggregation behavior. While the Tel24 was resulting in aggregation, the single-stranded dA_{32}, dsDNA ($dA_{32}dT_{32}$), or the modified Tel24 sequences did not result in aggregation. The ssDNA, dsDNA, or the partially folded structures might be extending out to the solution resulting in the repulsion between the negatively charged DNA strands compared to the fully folded DNA similar to the observations made by Sutter et al. Again, the induction of aggregation with Tel24 having TTA loops compared to the Tel24m5, might related to the higher affinity of adenines [386] to nanoparticles or due to the pronation at low pH as mentioned by Sutter et al. [392]. Among all the nucleic acid structures investigated during selectivity experiments, in addition to human telomeric G4 DNAs (Tel24 and Tel24m1), Tel24m2, VEGF, and Her2/Neu1 also resulted in a slight blue peak shift (around 13 nm). Consequently, it was hypothesized that the G4 topology could be the reason behind this blue shift. To prove this consideration, thermal denaturation and CD studies were performed with three different DNAs in addition to Tel24 and Tel24m1. VEGF was chosen to be analyzed as a positive reference since it was one of the blue shift-causing DNA and Pu22 and Tel24m3 were chosen as nonresponding reference samples because of the nearly zero peak shift observed. Firstly, thermal denaturation studies were performed. Determined melting temperatures of oligonucleotides that were used to explain the mechanism tabulated in Table 6. In general, the addition of CTAB and HCl stabilized the DNA [371]. Followingly, CD studies were conducted (

Table 7). As it was stated before our main analyte Tel24 had parallel topology in the presence of HCl and CTAB [377]. Tel24m1 and VEGF are also found to possess parallel structures in the presence of CTAB and HCl similar to Tel24 when they were incubated at 60℃ for 10 min. On the other hand, both Pu22 and Tel23m3, in which our probe was not showing any response, were found to have random coil structures in the presence of CTAB and HCl after they were incubated at 60℃ for 10 min. These results support our hypothesis that our developed detection system might be showing a response to only G4s with a parallel folded topology in the presence of HCl and CTAB.

Table 6. Melting temperatures of several oligonucleotides.

Samples	**Melting Temperature (℃)**
Tel24	59 (Figure C 1)
Tel24+HCl+CTAB	69 (Figure C 3)
VEGF	51 (Figure C 4)
VEGF+HCl+CTAB	67 (Figure C 5)
Tel24m1	65 (Figure C 6)
Tel24m1+HCl+CTAB	67 (Figure C 7)
Pu22	41 (Figure C 8)
Pu22+HCl+CTAB	47 (Figure C 9)
Tel24m3	27 (Figure C 10)
Tel24m3+HCl+CTAB	31 (Figure C 11)

Table 7. Wavelengths of maxima and minima peaks and topologies of several oligonucleotides according to CD studies.

Samples	**Max 1 (nm)**	**Max 2 (nm)**	**Min (nm)**	**Topology**
Tel24 (15℃)	289	271	237	Hybrid (Figure D 2)
Tel24 (60℃)	289	270	240	Hybrid (Figure D 2)
Tel24+HCl+CTAB (15℃)	264	-	244	Parallel (Figure D 3)

Table 7 (continued)

Tel24+HCl+CTAB (60℃)	264	-	243	Parallel (Figure D 3)
VEGF (15℃)	263	-	240	Parallel (Figure D 4)
VEGF (60℃)	262	-	240	Parallel (Figure D 4)
VEGF+HCl+CTAB (15℃)	264	-	243	Parallel (Figure D 4)
VEGF+HCl+CTAB (60℃)	266	-	245	Parallel (Figure D 4)
Tel24m1 (15℃)	288	271	245	Hybrid (Figure D 5)
Tel24m1 (60℃)	-	256	-	Random coil (Figure D 5)
Tel24m1+HCl+CTAB (15℃)	291	270	240	Hybrid (Figure D 5)
Tel24m1+HCl+CTAB (60℃)	266	-	245	Parallel (Figure D 5)
Pu22 (15℃)	290	244	266	Anti-Parallel (Figure D 6)
Pu22 (60℃)	280	-	228	Random coil (Figure D 6)
Pu22+HCl+CTAB (15℃)	285	253	214	Random coil (Figure D 6)
Pu22+HCl+CTAB (60℃)	283	251	229	Random coil (Figure D 6)
Tel24m3 (15℃)	277	-	245	Random coil (Figure D 7)
Tel24m3 (60℃)	274	-	246	Random coil (Figure D 7)
Tel24m3+HCl+CTAB (15℃)	278	-	248	Random coil (Figure D 7)
Tel24m3+HCl+CTAB (60℃)	276	-	251	Random coil (Figure D 7)

On the other hand, the etching of GNRs observed can result from many mechanisms. However, based on the obtained results and a detailed literature review, the direct etching strategy, where guanine and/or adenine acted as the direct etchants, was thought to be the plausible mechanism in this thesis study. The reason for this consideration was based on two main reasons.

As it was mentioned before that the materials with greater reduction potential than the reduction potential of Au^{+}/Au, such as ferric ions [190,191], chromium ions [192–194] and copper ions [195,196], can directly etch GNRs. In addition, it was shown that the

reduction potential of Au^{+}/Au was reduced to 0.959 V from 1.69 V in the presence of Br^{-} ions of CTAB [398]. The standard reduction potentials of guanosine and adenosine were estimated as 1.58 V and 1.73 V [399]. Since both G and A have higher reduction potential than, the Au^{+}/Au pair, they can theoretically etch GNRs. The topology of Tel24 might also be playing a role here. Firstly, when the G-tetrad planes of Tel24 were disrupted in several ways (Tel24m2, Tel24m3, Tel24m4, Tel24m5), the response of the system was altered. For instance, when the guanine modification is only affecting a single plane as in the case of Tel24m2 or Tel24m4, the probe was still showing a response to a 13 nm peak shift and a 7 nm peak shift, respectively, which might be an indication of a relatively mild destabilization of the structure. However, when all three Guanines were replaced so that all three planes were affected (Tel24m3) no significant peak shift was observed. These observations showed that G-tetrad formation might also be playing a significant role in the etching of the probe GNRs.

Secondly, Tel24m5 was altered to change the TTA loop sequence of the target G4 to TTT. This change resulted almost in a complete loss of response of the system supporting the idea of the contribution of adenine to the etching mechanism. Additionally, G4 structures that caused lower blue shifts from human telomeric G4s, Tel24m2, VEGF, and Her2/Neu1, also contain adenine in their loop sequences.

As a result, even though the exact mechanism of the aggregation and etching cannot be deduced, G-tetrad forming guanine and adenine present in the loop sequence and the parallel topology were thought to be the main players behind the specific response of our probe to Tel24.

CHAPTER 4

CONCLUSION

The four stranded G4 DNA is one of the unique noncanonical structures present in our genome, in the guanine rich sequences. And among these sequences that have a propensity to form G4 structures, telomeric DNA has been one of the extensively investigated. In vitro and in vivo data have shown that the guanine-rich region of the telomere has a significant physiological impact. Even though early studies revealed its protective role of the chromosome ends, the exact functions of this guanine rich regions and the G4s formed at chromosome ends are still unknown. Several hypotheses have been proposed for the various G4 conformations that are plausible in that region. G4s in intramolecular conformation are believed to have a packing role, folding the chromosomal end into a compact structure, and/or a regulatory and protective role, securing the G-overhang from telomerase and nucleases. In contrast, it is believed that during meiotic prophase I, intermolecular G4s facilitate telomere clustering and interchromosomal alignment [303].

G4 stabilizing drugs are a new class of cancer therapies that have emerged as a result of telomerase's incapacity to use a G4 folded telomeric substrate. These have the ability to encapsulate DNA in a quadruplex shape, which may either disrupt telomere-capping processes or prevent telomerase from extending telomeres. The latter effect is particularly relevant for tumors that are both ALT- and telomerase-positive. The structural variability of G4s originating from human telomeric DNA may provide a challenge to this method. Furthermore, uncertainties persist concerning the in vivo mode of action of current G4 stabilizers. Still, they provide an interesting prospect and could prove to be a useful new cancer control method [303].

Within the scope of this thesis, we aimed to develop a cost-efficient, straightforward, fast, sensitive, and selective colorimetric detection platform for the human telomeric

G4 DNA, Tel24, by utilizing GNRs. GNRs were synthesized by using the seed-mediated growth method. The CTEM micrographs indicated that the synthesized GNRs had colloidal dispersion. The intensity results of DLS measurements showed that the synthesized GNRs inherited a length of 46.13 ± 4.00 nm. GNRs exhibit a red color with a transverse LSPR band at 515 nm and a longitudinal LSPR band at 715 nm. Upon the addition of Tel24 in the presence of HCl (10 min of incubation at 60°C), the transverse LSPR shifted to 534 nm, while the longitudinal LSPR shifted to 675 nm and the color of the solution changed from red to purple and then pale blue. Additionally, neither HCl nor Tel24 caused any change in the LSPR bands by itself. When CTEM results were examined to characterize the system, it was concluded that both aggregation and etching resulted in the shifts of LSPR bands. Moreover, parameters that affected the sensitivity of the proposed system were optimized. Accordingly, it was decided that the optimum sensitivity of the detection system can be obtained under the presence of 0.01 M CTAB, 28 mM HCl, and 60°C incubation temperature and 10 min of incubation time. For further characterization, DLS and Zeta potential measurements were performed. The size distribution by number measurements emphasized that synthesized GNRs were 46.13 ± 4.00 nm in size. After 6-min and 10-min of incubation, their size increased to 83.54 ± 13.41 nm and 156.73 ± 12.93 nm, respectively. Furthermore, the mean zeta potential value of the GNRs in the probe solution was measured as +34.6 ± 5.59 mV. After the addition of Tel24 over the 6 min incubation, this value was decreased to +26.9 ± 7.08 mV and increased to +47.5 ± 6.73 mV after 10 min incubation. The selectivity of the proposed probe was investigated by examining various available G4 structures (Pu22, VEGF, K-RAS, BCl-2, C-MYC, Her2/Neu1, RB) including the mismatch and complementary structures (Tel24m1, Tel24m2, Tel24m3, Tel24m4, Tel24m5, Tel24comp, single- (dA_{32}, dT_{32}), and double- ($dA_{32}dT_{32}$), and triple-stranded ($dA_{32}dT_{32}dT_{32}$) oligonucleotides. Our results indicated the developed probe showed good selectivity towards human telomeric G4 sequences (Tel24 and Tel24m1) and its possible use in the detection of human telomeric sequences. Furthermore, sensitivity studies exhibited that the LDR of the proposed system was from 0.371 to 0.909 μM, and the LOD was calculated as 0.03 μM.

To the best of our knowledge this thesis presents the first study for colorimetric detecting human telomeric G4 DNA via using GNRs.

We believe that the developed colorimetric detection platform can open new avenues for using GNRs and establishing more straightforward visual detection approaches in G4 DNA detection strategies.

REFERENCES

[1] Ensafi AA. An introduction to sensors and biosensors. Electrochemical Biosensors, Elsevier; 2019, p. 1–10. https://doi.org/10.1016/B978-0-12-816491-4.00001-2.

[2] Kenny T, Kester W. Sensor fundamentals. Sensor Technology Handbook, Elsevier; 2005, p. 1–20. https://doi.org/10.1016/B978-075067729-5/50041-0.

[3] Fraden J. Sensor characteristics. Handbook of Modern Sensors, New York, NY: Springer New York; 2010, p. 13–52. https://doi.org/10.1007/978-1-4419-6466-3_2.

[4] Naresh V, Lee N. A review on biosensors and recent development of nanostructured materials-enabled biosensors. Sensors (Basel) 2021;21:1109. https://doi.org/10.3390/s21041109.

[5] Clark Lc, Lyons C. Electrode systems for continuous monitoring in cardiovascular surgery. Ann N Y Acad Sci 1962;102:29–45. https://doi.org/10.1111/j.1749-6632.1962.tb13623.x.

[6] Rechnitz GA, Kobos RK, Riechel SJ, Gebauer CR. A bio-selective membrane electrode prepared with living bacterial cells. Anal Chim Acta 1977;94:357–65. https://doi.org/10.1016/S0003-2670(01)84537-2.

[7] Bhalla N, Jolly P, Formisano N, Estrela P. Introduction to biosensors. Essays Biochem 2016;60:1–8. https://doi.org/10.1042/EBC20150001.

[8] Buerk DG. Biosensors. CRC Press; 2014. https://doi.org/10.1201/9781498710770.

[9] Banigo A, Azeez T, Ejeta K, Lateef A, Ajuogu E. Nanobiosensors: applications in biomedical technology. IOP Conf Ser Mater Sci Eng 2020;805:012028. https://doi.org/10.1088/1757-899X/805/1/012028.

[10] Gdowski A, Ranjan AP, Mukerjee A, Vishwanatha JK. Nanobiosensors: role in cancer detection and diagnosis. Adv Exp Med Biol 2014;807:33–58. https://doi.org/10.1007/978-81-322-1777-0_4.

[11] Osuwa JC, Anusionwu PC. Some advances and prospects in nanotechnology: a review. Asian Journal of Information Technology 2011;10:96–100. https://doi.org/10.3923/ajit.2011.96.100.

[12] Haruta M. When gold is not noble: catalysis by nanoparticles. Chem Rec 2003;3:75–87. https://doi.org/10.1002/tcr.10053.

[13] Malik P, Katyal V, Malik V, Asatkar A, Inwati G, Mukherjee TK. Nanobiosensors: concepts and variations. ISRN Nanomater 2013;2013:1–9. https://doi.org/10.1155/2013/327435.

[14] Ferrier DC, Honeychurch KC. Carbon nanotube (cnt)-based biosensors. Biosensors (Basel) 2021;11:486. https://doi.org/10.3390/bios11120486.

[15] Vashist SK, Zheng D, Al-Rubeaan K, Luong JHT, Sheu F-S. Advances in carbon nanotube based electrochemical sensors for bioanalytical applications. Biotechnol Adv 2011;29:169–88. https://doi.org/10.1016/j.biotechadv.2010.10.002.

[16] Chen Z, Zhang X, Yang R, Zhu Z, Chen Y, Tan W. Single-walled carbon nanotubes as optical materials for biosensing. Nanoscale 2011;3:1949–56. https://doi.org/10.1039/c0nr01014f.

[17] Park RS, Hills G, Sohn J, Mitra S, Shulaker MM, Wong H-SP. Hysteresis-free carbon nanotube field-effect transistors. ACS Nano 2017;11:4785–91. https://doi.org/10.1021/acsnano.7b01164.

[18] Dervisevic M, Custiuc E, Çevik E, Şenel M. Construction of novel xanthine biosensor by using polymeric mediator/mwcnt nanocomposite layer for fish freshness detection. Food Chem 2015;181:277–83. https://doi.org/10.1016/j.foodchem.2015.02.104.

[19] Wilson TA, Musameh M, Kyratzis IL, Zhang J, Bond AM, Hearn MTW. Enhanced nadh oxidation using polytyramine/carbon nanotube modified electrodes for ethanol biosensing. Electroanalysis 2017;29:1985–93. https://doi.org/10.1002/elan.201700146.

[20] Huang B, Liu J, Lai L, Yu F, Ying X, Ye B-C, et al. A free-standing electrochemical sensor based on graphene foam-carbon nanotube composite coupled with gold nanoparticles and its sensing application for electrochemical determination of dopamine and uric acid. Journal of Electroanalytical Chemistry 2017;801:129–34. https://doi.org/10.1016/j.jelechem.2017.07.029.

[21] Su Z, Xu X, Xu H, Zhang Y, Li C, Ma Y, et al. Amperometric thrombin aptasensor using a glassy carbon electrode modified with polyaniline and multiwalled carbon nanotubes tethered with a thiolated aptamer. Microchimica Acta 2017;184:1677–82. https://doi.org/10.1007/s00604-017-2164-9.

[22] Moyo M, Okonkwo JO, Agyei NM. An amperometric biosensor based on horseradish peroxidase immobilized onto maize tassel-multi-walled carbon nanotubes modified glassy carbon electrode for determination of heavy metal ions in aqueous solution. Enzyme Microb Technol 2014;56:28–34. https://doi.org/10.1016/j.enzmictec.2013.12.014.

[23] Yu X. Peroxidase activity of enzymes bound to the ends of single-wall carbon nanotube forest electrodes. Electrochem Commun 2003;5:408–11. https://doi.org/10.1016/S1388-2481(03)00076-6.

[24] Li J, Ng HT, Cassell A, Fan W, Chen H, Ye Q, et al. Carbon Nanotube Nanoelectrode Array for Ultrasensitive DNA Detection. Nano Lett 2003;3:597–602. https://doi.org/10.1021/nl0340677.

[25] Zhang A, Zheng G. Semiconductor nanowires for biosensors. Semiconductor Nanowires, Elsevier; 2015, p. 471–90. https://doi.org/10.1016/B978-1-78242-253-2.00017-7.

[26] Patolsky F, Zheng G, Lieber CM. Nanowire-based biosensors. Anal Chem 2006;78:4260–9. https://doi.org/10.1021/ac069419j.

[27] Hou J, Jia P, Yang K, Bu T, Sun X, Wang L. Facile preparation of Ru@V2O4 nanowires exhibiting excellent tetra-enzyme mimetic activities for sensitive colorimetric H2O2 and cysteine sensing. Sens Actuators B Chem 2021;344:130266. https://doi.org/10.1016/j.snb.2021.130266.

[28] Luo J, Cui J, Wang Y, Yu D, Qin Y, Zheng H, et al. Metal-organic framework-derived porous Cu2O/Cu@C core-shell nanowires and their application in uric acid biosensor. Appl Surf Sci 2020;506:144662. https://doi.org/10.1016/j.apsusc.2019.144662.

[29] Guo X, Wu J, Xia L, Xiang M, Qu F, Li J. CuO/Cu2O nanowire array photoelectrochemical biosensor for ultrasensitive detection of tyrosinase. Sci China Chem 2020;63:1012–8. https://doi.org/10.1007/s11426-020-9717-8.

[30] Chou W-C, Hu W-P, Yang Y-S, Chan HW-H, Chen W-Y. Neutralized chimeric DNA probe for the improvement of GC-rich RNA detection specificity on the nanowire field-effect transistor. Sci Rep 2019;9:11056. https://doi.org/10.1038/s41598-019-47522-9.

[31] Malsagova KA, Pleshakova TO, Galiullin RA, Kozlov AF, Shumov ID, Popov VP, et al. Highly sensitive detection of CA 125 protein with the use of an n-type nanowire biosensor. Biosensors (Basel) 2020;10:210. https://doi.org/10.3390/bios10120210.

[32] Khosravi-Nejad F, Teimouri M, Jafari Marandi S, Shariati M. The highly sensitive impedimetric biosensor in label free approach for hepatitis B virus DNA detection based on tellurium doped ZnO nanowires. Applied Physics A 2019;125:616. https://doi.org/10.1007/s00339-019-2890-4.

[33] Li Y, Schluesener HJ, Xu S. Gold nanoparticle-based biosensors. Gold Bull 2010;43:29–41. https://doi.org/10.1007/BF03214964.

[34] Zhang N, Zhao Z-Y, Gao H, Yu Y, Pan J-B, Chen H-Y, et al. An ultrasensitive electrochemiluminescence assay for nucleic acid detection based on carboxyl functionalized polymer dots. Journal of Electroanalytical Chemistry 2021;900:115743. https://doi.org/10.1016/j.jelechem.2021.115743.

[35] Zhou L, Xiong W, Liu S. Preparation of a gold electrode modified with Au–TiO2 nanoparticles as an electrochemical sensor for the detection of mercury(II) ions. J Mater Sci 2015;50:769–76. https://doi.org/10.1007/s10853-014-8636-y.

[36] Fan Y, Huang K-J, Niu D-J, Yang C-P, Jing Q-S. TiO2-graphene nanocomposite for electrochemical sensing of adenine and guanine. Electrochim Acta 2011;56:4685–90. https://doi.org/10.1016/j.electacta.2011.02.114.

[37] Tang Y, Yang Q, Wu T, Liu L, Ding Y, Yu B. Fluorescence enhancement of cadmium selenide quantum dots assembled on silver nanoparticles and its application to glucose detection. Langmuir 2014;30:6324–30. https://doi.org/10.1021/la5012154.

[38] Jeong HY, Baek SH, Chang S-J, Cheon SA, Park TJ. Robust fluorescence sensing platform for detection of CD44 cells based on graphene oxide/gold nanoparticles. Colloids Surf B Biointerfaces 2015;135:309–15. https://doi.org/10.1016/j.colsurfb.2015.07.083.

[39] Welch EC, Powell JM, Clevinger TB, Fairman AE, Shukla A. Advances in biosensors and diagnostic technologies using nanostructures and nanomaterials. Adv Funct Mater 2021;31:2104126. https://doi.org/10.1002/adfm.202104126.

[40] Alizadeh N, Ghasemi S, Salimi A, Sham T-K, Hallaj R. CuO nanorods as a laccase mimicking enzyme for highly sensitive colorimetric and electrochemical dual biosensor: Application in living cell epinephrine analysis. Colloids Surf B Biointerfaces 2020;195:111228. https://doi.org/10.1016/j.colsurfb.2020.111228.

[41] Hu W, Liu Y, Chen T, Liu Y, Li CM. Hybrid ZnO nanorod-polymer brush hierarchically nanostructured substrate for sensitive antibody microarrays. Adv Mater 2015;27:181–5. https://doi.org/10.1002/adma.201403712.

[42] Wang W, Xu Y, Hou J, Li Z, Luo F, He D, et al. Multicolor biosensor for hyaluronidase based on target-responsive hydrogel and etching of gold nanorods by H2O2. Talanta 2023;257:124367. https://doi.org/10.1016/j.talanta.2023.124367.

[43] Cao J, Sun T, Grattan KTV. Gold nanorod-based localized surface plasmon resonance biosensors: A review. Sens Actuators B Chem 2014;195:332–51. https://doi.org/10.1016/j.snb.2014.01.056.

[44] Wang C, Chen Y, Wang T, Ma Z, Su Z. Biorecognition-driven self-assembly of gold nanorods: A rapid and sensitive approach toward antibody sensing. Chemistry of Materials 2007;19:5809–11. https://doi.org/10.1021/cm0700899.

[45] Zhu Y, Qu C, Kuang H, Xu L, Liu L, Hua Y, et al. Simple, rapid and sensitive detection of antibiotics based on the side-by-side assembly of gold nanorod probes. Biosens Bioelectron 2011;26:4387–92. https://doi.org/10.1016/j.bios.2011.04.046.

[46] Wang L, Zhu Y, Xu L, Chen W, Kuang H, Liu L, et al. Side-by-side and end-to-end gold nanorod assemblies for environmental toxin sensing. Angewandte Chemie International Edition 2010;49:5472–5. https://doi.org/10.1002/anie.200907357.

[47] Wang C, Irudayaraj J. Gold nanorod probes for the detection of multiple pathogens. Small 2008;4:2204–8. https://doi.org/10.1002/smll.200800309.

[48] Biswas S, Tripathi P, Kumar N, Nara S. Gold nanorods as peroxidase mimetics and its application for colorimetric biosensing of malathion. Sens Actuators B Chem 2016;231:584–92. https://doi.org/10.1016/j.snb.2016.03.066.

[49] Chang C-W, Wang C-H, Peng C-A. Gold nanorods modified with chitosan as photothermal agents. IFMBE Proc, vol. 23, Springer, Berlin, Heidelberg; 2009, p. 874–7. https://doi.org/10.1007/978-3-540-92841-6_215.

[50] Ha S, Tripathy S, Carson A, Lavery LL, Zhang H, Agarwal A, et al. Multi-target photoacoustic molecular imaging of cardiovascular inflammatory biomarkers using bioconjugated gold nanorods. In: Oraevsky AA, Wang L V., editors. vol. 7899, SPIE; 2011, p. 78991M. https://doi.org/10.1117/12.875459.

[51] Chen J, Liang H, Lin L, Guo Z, Sun P, Chen M, et al. Gold-nanorods-based gene carriers with the capability of photoacoustic imaging and photothermal therapy. ACS Appl Mater Interfaces 2016;8:31558–66. https://doi.org/10.1021/acsami.6b10166.

[52] Yang D-P, Cui D-X. Advances and prospects of gold nanorods. Chem Asian J 2008;3:2010–22. https://doi.org/10.1002/asia.200800195.

[53] Vigderman L, Khanal BP, Zubarev ER. Functional gold nanorods: Synthesis, self-assembly, and sensing applications. Adv Mater 2012;24:4811–41, 5014. https://doi.org/10.1002/adma.201201690.

[54] Huang X, Neretina S, El-Sayed MA. Gold nanorods: from synthesis and properties to biological and biomedical applications. Advanced Materials 2009;21:4880–910. https://doi.org/10.1002/adma.200802789.

[55] Pérez-Juste J, Pastoriza-Santos I, Liz-Marzán LM, Mulvaney P. Gold nanorods: Synthesis, characterization and applications. Coord Chem Rev 2005;249:1870–901. https://doi.org/10.1016/j.ccr.2005.01.030.

[56] Chen H, Shao L, Li Q, Wang J. Gold nanorods and their plasmonic properties. Chem Soc Rev 2013;42:2679–724. https://doi.org/10.1039/C2CS35367A.

[57] Rodrigues MS, Borges J, Lopes C, Pereira RMS, Vasilevskiy MI, Vaz F. Gas sensors based on localized surface plasmon resonances: synthesis of oxide films with embedded metal nanoparticles, theory and simulation, and sensitivity enhancement strategies. Applied Sciences 2021;11:5388. https://doi.org/10.3390/app11125388.

[58] Evans PR, Hendren WR, Atkinson R, Pollard RJ. Nickel-coated gold-core nanorods produced by template assisted electrodeposition. J Electrochem Soc 2007;154:K79. https://doi.org/10.1149/1.2752119.

[59] Yu, Chang S-S, Lee C-L, Wang CRC. Gold nanorods: Electrochemical synthesis and optical properties. J Phys Chem B 1997;101:6661–4. https://doi.org/10.1021/jp971656q.

[60] Koeppl S, Ghielmetti N, Caseri W, Spolenak R. Seed-mediated synthesis of gold nanorods: control of the aspect ratio by variation of the reducing agent. Journal of Nanoparticle Research 2013;15:1471. https://doi.org/10.1007/s11051-013-1471-2.

[61] Abdelrasoul GN, Cingolani R, Diaspro A, Athanassiou A, Pignatelli F. Photochemical synthesis: Effect of UV irradiation on gold nanorods morphology. J Photochem Photobiol A Chem 2014;275:7–11. https://doi.org/10.1016/j.jphotochem.2013.10.008.

[62] Murphy CJ, Jana NR. Controlling the aspect ratio of inorganic nanorods and nanowires. 2002. https://doi.org/10.1002/1521-4095(20020104)14:1<80::AID-ADMA80>3.0.CO;2-%23.

[63] Nikoobakht B, El-Sayed MA. preparation and growth mechanism of gold nanorods (NRs) using seed-mediated growth method. Chemistry of Materials 2003;15:1957–62. https://doi.org/10.1021/cm020732l.

[64] Jana NR, Gearheart L, Murphy CJ. wet chemical synthesis of high aspect ratio cylindrical gold nanorods. J Phys Chem B 2001;105:4065–7. https://doi.org/10.1021/jp0107964.

[65] Pérez-Juste J, Liz-Marzán LM, Carnie S, Chan DYC, Mulvaney P. Electric-field-directed growth of gold nanorods in aqueous surfactant solutions. Adv Funct Mater 2004;14:571–9. https://doi.org/10.1002/adfm.200305068.

[66] Martin CR. Nanomaterials: A membrane-based synthetic approach. Science (1979) 1994;266:1961–6. https://doi.org/10.1126/science.266.5193.1961.

[67] Martin CR. membrane-based synthesis of nanomaterials. Chemistry of Materials 1996;8:1739–46. https://doi.org/10.1021/cm960166s.

[68] Foss CA, Hornyak GL, Stockert JA, Martin CR. Optical properties of composite membranes containing arrays of nanoscopic gold cylinders. J Phys Chem 1992;96:7497–9. https://doi.org/10.1021/j100198a004.

[69] Li Q, Cao Y. Preparation and characterization of gold nanorods. In: Yalçın Orhan, editor. Nanorods, InTech; 2012, p. 160. https://doi.org/10.5772/2046.

[70] Lebepe TC, Parani S, Oluwafemi OS. graphene oxide-coated gold nanorods: Synthesis and applications. Nanomaterials 2020;10:2149. https://doi.org/10.3390/nano10112149.

[71] Chang S-S, Shih C-W, Chen C-D, Lai W-C, Wang CRC. The shape transition of gold nanorods. Langmuir 1999;15:701–9. https://doi.org/10.1021/la980929l.

[72] Gorbunova M, Apyari V, Dmitrienko S, Zolotov Y. Gold nanorods and their nanocomposites: Synthesis and recent applications in analytical chemistry. TrAC Trends in Analytical Chemistry 2020;130:115974. https://doi.org/10.1016/j.trac.2020.115974.

[73] Wiesner J, Wokaun A. Anisometric gold colloids. Preparation, characterization, and optical properties. Chem Phys Lett 1989;157:569–75. https://doi.org/10.1016/S0009-2614(89)87413-5.

[74] Jana NR, Gearheart L, Murphy CJ. Seed-mediated growth approach for shape-controlled synthesis of spheroidal and rod-like gold nanoparticles using a surfactant template. Physical Chemistry of Surfaces 2001;13:1389–92.

[75] Wu H-Y, Chu H-C, Kuo T-J, Kuo C-L, Huang MH. Seed-mediated synthesis of high aspect ratio gold nanorods with nitric acid. Chemistry of Materials 2005;17:6447–51. https://doi.org/10.1021/cm051455w.

[76] Murphy CJ, Sau TK, Gole AM, Orendorff CJ, Gao J, Gou L, et al. Anisotropic metal nanoparticles: Synthesis, assembly, and optical applications. J Phys Chem B 2005;109:13857–70. https://doi.org/10.1021/jp0516846.

[77] Mahdi HS, Parveen A, Azam A. Synthesis and structural properties of gold nanoparticles by the chemical reduction method using sodium borohydride. IOP Conf Ser Mater Sci Eng 2019;577:012034. https://doi.org/10.1088/1757-899X/577/1/012034.

[78] Khan Z, Singh T, Hussain JI, Hashmi AA. Au(III)–CTAB reduction by ascorbic acid: Preparation and characterization of gold nanoparticles. Colloids Surf B

Biointerfaces 2013;104:11–7. https://doi.org/10.1016/J.COLSURFB.2012.11.017.

[79] Scarabelli L, Sánchez-Iglesias A, Pérez-Juste J, Liz-Marzán LM. A "Tips and tricks" practical guide to the synthesis of gold nanorods. J Phys Chem Lett 2015;6:4270–9. https://doi.org/10.1021/acs.jpclett.5b02123.

[80] Johnson CJ, Dujardin E, Davis SA, Murphy CJ, Mann S. Growth and form of gold nanorods prepared by seed-mediated, surfactant-directed synthesis. J Mater Chem 2002;12:1765–70. https://doi.org/10.1039/b200953f.

[81] Gai PL, Harmer MA. Surface atomic defect structures and growth of gold nanorods. Nano Lett 2002;2:771–4. https://doi.org/10.1021/nl0202556.

[82] Liu M, Guyot-Sionnest P. Mechanism of silver(i)-assisted growth of gold nanorods and bipyramids. J Phys Chem B 2005;109:22192–200. https://doi.org/10.1021/jp054808n.

[83] Orendorff CJ, Murphy CJ. Quantitation of metal content in the silver-assisted growth of gold nanorods. J Phys Chem B 2006;110:3990–4. https://doi.org/10.1021/jp0570972.

[84] Hayee F, Narayan TC, Nadkarni N, Baldi A, Koh AL, Bazant MZ, et al. In-situ visualization of solute-driven phase coexistence within individual nanorods. Nat Commun 2018;9:1775. https://doi.org/10.1038/s41467-018-04021-1.

[85] Jana NR. Gram-scale synthesis of soluble, near-monodisperse gold nanorods and other anisotropic nanoparticles. Small 2005;1:875–82. https://doi.org/10.1002/smll.200500014.

[86] Zijlstra P, Bullen C, Chon JWM, Gu M. High-temperature seedless synthesis of gold nanorods. J Phys Chem B 2006;110:19315–8. https://doi.org/10.1021/jp0635866.

[87] Kim Y-J, Song JH. Preparation of Au nanomaterials via pulsed proton beam irradiation. Journal of the Korean Physical Society 2011;59:644–7. https://doi.org/10.3938/jkps.59.644.

[88] Zhu Y-J, Hu X-L. Microwave-polyol preparation of single-crystalline gold nanorods and nanowires. Chem Lett 2003;32:1140–1. https://doi.org/10.1246/cl.2003.1140.

[89] Canizal G, Ascencio JA, Gardea-Torresday J, José-Yacamán M. Multiple twinned gold nanorods grown by bio-reduction techniques. Journal of Nanoparticle Research 2001;3:475–81. https://doi.org/10.1023/A:1012578821566.

[90] Cao J, Ma X, Zheng M, Liu J, Ji H. Solvothermal preparation of single-crystalline gold nanorods in novel nonaqueous microemulsions. Chem Lett 2005;34:730–1. https://doi.org/10.1246/cl.2005.730.

[91] Cobley CM, Chen J, Cho EC, Wang L V., Xia Y. Gold nanostructures: a class of multifunctional materials for biomedical applications. Chem Soc Rev 2011;40:44–56. https://doi.org/10.1039/B821763G.

[92] Zhu Y, Kuang H, Xu L, Ma W, Peng C, Hua Y, et al. Gold nanorodassembly based approach to toxin detection by SERS. J Mater Chem 2012;22:2387–91. https://doi.org/10.1039/C2JM15238J.

[93] Peixoto LPF, Santos JFL, Andrade GFS. Surface enhanced fluorescence immuno-biosensor based on gold nanorods. Spectrochim Acta A Mol Biomol Spectrosc 2023;284:121753. https://doi.org/10.1016/j.saa.2022.121753.

[94] Chen Z, Zhang L, Liu Y, Li J. Highly sensitive electrogenerated chemiluminescence biosensor for galactosyltransferase activity and inhibition detection using gold nanorod and enzymatic dual signal amplification. Journal of Electroanalytical Chemistry 2016;781:83–9. https://doi.org/10.1016/j.jelechem.2016.05.034.

[95] Hosseinniay S, Rezayan AH, Ghasemi F, Malekmohamadi M, Taheri RA, Hosseini M, et al. Fabrication and evaluation of optical nanobiosensor based on localized surface plasmon resonance (LSPR) of gold nanorod for detection of CRP. Anal Chim Acta 2023;1237:340580. https://doi.org/10.1016/j.aca.2022.340580.

[96] Harish KK, Nagasamy V, Himangshu B, Anuttam K. Metallic nanoparticle: A review. Biomed J Sci &Tech Res 2018;4. https://doi.org/10.26717/BJSTR.2018.04.001011.

[97] Taylor ML, Wilson RE, Amrhein KD, Huang X. Gold nanorod-assisted photothermal therapy and improvement strategies. Bioengineering 2022;9:200. https://doi.org/10.3390/bioengineering9050200.

[98] Gans R. Über die form ultramikroskopischer silberteilchen. Ann Phys 1915;352:270–84. https://doi.org/10.1002/andp.19153521006.

[99] Yan B, Yang, Wang Y. Comment on “simulation of the optical absorption spectra of gold nanorods as a function of their aspect ratio and the effect of the medium dielectric constant.” J Phys Chem B 2003;107:9159–9159. https://doi.org/10.1021/jp035241i.

[100] Brioude A, Jiang XC, Pileni MP. Optical properties of gold nanorods: DDA simulations supported by experiments. J Phys Chem B 2005;109:13138–42. https://doi.org/10.1021/jp0507288.

[101] Link S, El-Sayed MA. Simulation of the optical absorption spectra of gold nanorods as a function of their aspect ratio and the effect of the medium dielectric constant. J Phys Chem B 2005;109:10531–2. https://doi.org/10.1021/jp058091f.

[102] Eustis S, El-Sayed MA. Determination of the aspect ratio statistical distribution of gold nanorods in solution from a theoretical fit of the observed inhomogeneously broadened longitudinal plasmon resonance absorption spectrum. J Appl Phys 2006;100:044324. https://doi.org/10.1063/1.2244520.

[103] Chen H, Kou X, Yang Z, Ni W, Wang J. Shape- and size-dependent refractive index sensitivity of gold nanoparticles. Langmuir 2008;24:5233–7. https://doi.org/10.1021/la800305j.

[104] Sönnichsen C, Franzl T, Wilk T, von Plessen G, Feldmann J, Wilson O, et al. Drastic reduction of plasmon damping in gold nanorods. Phys Rev Lett 2002;88:077402. https://doi.org/10.1103/PhysRevLett.88.077402.

[105] Xie L, Zhang X, Chu C, Dong Y, Zhang T, Li X, et al. Preparation, toxicity reduction and radiation therapy application of gold nanorods. J Nanobiotechnology 2021;19:454. https://doi.org/10.1186/s12951-021-01209-4.

[106] Yu C, Irudayaraj J. Multiplex biosensor using gold nanorods. Anal Chem 2007;79:572–9. https://doi.org/10.1021/ac061730d.

[107] Huang X, El-Sayed IH, Qian W, El-Sayed MA. Cancer cell imaging and photothermal therapy in the near-infrared region by using gold nanorods. J Am Chem Soc 2006;128:2115–20. https://doi.org/10.1021/ja057254a.

[108] Huang H-C, Barua S, Kay DB, Rege K. Simultaneous enhancement of photothermal stability and gene delivery efficacy of gold nanorods using polyelectrolytes. ACS Nano 2009;3:2941–52. https://doi.org/10.1021/nn900947a.

[109] Venkatesan R, Pichaimani A, Hari K, Balasubramanian PK, Kulandaivel J, Premkumar K. Doxorubicin conjugated gold nanorods: A sustained drug delivery carrier for improved anticancer therapy. J Mater Chem B 2013;1:1010–8. https://doi.org/10.1039/C2TB00078D.

[110] Truong PL, Cao C, Park S, Kim M, Sim SJ. A new method for non-labeling attomolar detection of diseases based on an individual gold nanorod immunosensor. Lab Chip 2011;11:2591. https://doi.org/10.1039/c1lc20085b.

[111] Shang W, Zeng C, Du Y, Hui H, Liang X, Chi C, et al. Core-shell gold nanorod@metal-organic framework nanoprobes for multimodality diagnosis of glioma. Adv Mater 2017;29:1604381. https://doi.org/10.1002/adma.201604381.

[112] Wang L, Liu Y, Li W, Jiang X, Ji Y, Wu X, et al. Selective targeting of gold nanorods at the mitochondria of cancer cells: Implications for cancer therapy. Nano Lett 2011;11:772–80. https://doi.org/10.1021/nl103992v.

[113] Colacio E, Cuesta R, Gutiérrez-Zorrilla JM, Luque A, Román P, Giraldi T, et al. Gold(I)−purine interactions: synthesis and characterization of cyclic and open chain polynuclear gold(i) complexes containing xanthine derivatives and bis(phosphine) as bridging ligands. crystal structures of $[Au_2(\mu\text{-}HX)(\mu\text{-}dmpe)]\cdot 3H_2O$ and $[Au_2(\mu\text{-}TT)(\mu\text{-}dmpe)]\cdot H_2O$ (H_3X=Xanthine; H_2TT=8-Mercaptotheophylline). Inorg Chem 1996;35:4232–8. https://doi.org/10.1021/ic951591a.

[114] Pearson RG. Hard and soft acids and bases. J Am Chem Soc 1963;85:3533–9. https://doi.org/10.1021/ja00905a001.

[115] Merchant B. Gold, the noble metal and the paradoxes of its toxicology. Biologicals 1998;26:49–59. https://doi.org/10.1006/biol.1997.0123.

[116] Shaw CF. Gold-based therapeutic agents. Chem Rev 1999;99:2589–600. https://doi.org/10.1021/cr980431o.

[117] Pissuwan D, Valenzuela S, Cortie MB. Prospects for gold nanorod particles in diagnostic and therapeutic applications. Biotechnol Genet Eng Rev 2008;25:93–112. https://doi.org/10.5661/bger-25-93.

[118] Nikoobakht B, El-Sayed MA. Evidence for bilayer assembly of cationic surfactants on the surface of gold nanorods. Langmuir 2001;17:6368–74. https://doi.org/10.1021/la010530o.

[119] Ito E, Yip KW, Katz D, Fonseca SB, Hedley DW, Chow S, et al. Potential use of cetrimonium bromide as an apoptosis-promoting anticancer agent for head and neck cancer. Mol Pharmacol 2009;76:969–83. https://doi.org/10.1124/mol.109.055277.

[120] Hauck TS, Ghazani AA, Chan WCW. Assessing the effect of surface chemistry on gold nanorod uptake, toxicity, and gene expression in mammalian cells. Small 2008;4:153–9. https://doi.org/10.1002/smll.200700217.

[121] Alkilany AM, Nagaria PK, Hexel CR, Shaw TJ, Murphy CJ, Wyatt MD. Cellular uptake and cytotoxicity of gold nanorods: molecular origin of cytotoxicity and surface effects. Small 2009;5:701–8. https://doi.org/10.1002/smll.200801546.

[122] Wang L, Jiang X, Ji Y, Bai R, Zhao Y, Wu X, et al. Surface chemistry of gold nanorods: origin of cell membrane damage and cytotoxicity. Nanoscale 2013;5:8384–91. https://doi.org/10.1039/c3nr01626a.

[123] Shi X, Perry HL, Wilton-Ely JDET. Strategies for the functionalisation of gold nanorods to reduce toxicity and aid clinical translation. Nanotheranostics 2021;5:155–65. https://doi.org/10.7150/ntno.56432.

[124] Niidome T, Yamagata M, Okamoto Y, Akiyama Y, Takahashi H, Kawano T, et al. PEG-modified gold nanorods with a stealth character for in vivo applications. J Control Release 2006;114:343–7. https://doi.org/10.1016/j.jconrel.2006.06.017.

[125] Su L, Hu S, Zhang L, Wang Z, Gao W, Yuan J, et al. A fast and efficient replacement of ctab with mua on the surface of gold nanorods assisted by a water-immiscible ionic liquid. Small 2017;13. https://doi.org/10.1002/smll.201602809.

[126] Li Z, Huang P, Zhang X, Lin J, Yang S, Liu B, et al. RGD-conjugated dendrimer-modified gold nanorods for in vivo tumor targeting and photothermal therapy. Mol Pharm 2010;7:94–104. https://doi.org/10.1021/mp9001415.

[127] Zhu H, Chen Y, Yan F-J, Chen J, Tao X-F, Ling J, et al. Polysarcosine brush stabilized gold nanorods for in vivo near-infrared photothermal tumor therapy. Acta Biomater 2017;50:534–45. https://doi.org/10.1016/j.actbio.2016.12.050.

[128] Shirshahi V, Hatamie S, Tabatabaei SN, Salimi M, Saber R. Enhanced thermal stability and biocompatibility of gold nanorods by graphene oxide. Plasmonics 2018;13:1585–94. https://doi.org/10.1007/s11468-017-0667-1.

[129] Huang P, Bao L, Zhang C, Lin J, Luo T, Yang D, et al. Folic acid-conjugated silica-modified gold nanorods for X-ray/CT imaging-guided dual-mode radiation and photo-thermal therapy. Biomaterials 2011;32:9796–809. https://doi.org/10.1016/j.biomaterials.2011.08.086.

[130] Liu J, Ma W, Kou W, Shang L, Huang R, Zhao J. Poly-amino acids coated gold nanorod and doxorubicin for synergistic photodynamic therapy and chemotherapy in ovarian cancer cells. Biosci Rep 2019;39. https://doi.org/10.1042/BSR20192521.

[131] Craciun AM, Focsan M, Gaina L, Astilean S. Enhanced one- and two-photon excited fluorescence of cationic (phenothiazinyl)vinyl-pyridinium chromophore attached to polyelectrolyte-coated gold nanorods. Dyes and Pigments 2017;136:24–30. https://doi.org/10.1016/j.dyepig.2016.08.033.

[132] Xu X, Ying Y, Li Y. Gold nanorods based lspr biosensor for label-free detection of alpha-fetoprotein. Procedia Eng 2011;25:67–70. https://doi.org/10.1016/j.proeng.2011.12.017.

[133] Wang X, Li Y, Wang H, Fu Q, Peng J, Wang Y, et al. Gold nanorod-based localized surface plasmon resonance biosensor for sensitive detection of

hepatitis B virus in buffer, blood serum and plasma. Biosens Bioelectron 2010;26:404–10. https://doi.org/10.1016/j.bios.2010.07.121.

[134] Huang H, Tang C, Zeng Y, Yu X, Liao B, Xia X, et al. Label-free optical biosensor based on localized surface plasmon resonance of immobilized gold nanorods. Colloids Surf B Biointerfaces 2009;71:96–101. https://doi.org/10.1016/j.colsurfb.2009.01.014.

[135] Li M, Lu D, You R, Shen H, Zhu L, Lin Q, et al. Surface-enhanced raman scattering biosensor based on self-assembled gold nanorod arrays for rapid and sensitive detection of tyrosinase. The Journal of Physical Chemistry C 2022;126:12651–9. https://doi.org/10.1021/acs.jpcc.2c03408.

[136] Wang J, Xie H, Ding C. Designed Co-DNA-locker and ratiometric SERS sensing for accurate detection of exosomes based on gold nanorod arrays. ACS Appl Mater Interfaces 2021;13:32837–44. https://doi.org/10.1021/acsami.1c09388.

[137] Lu X, Dong X, Zhang K, Han X, Fang X, Zhang Y. A gold nanorods-based fluorescent biosensor for the detection of hepatitis B virus DNA based on fluorescence resonance energy transfer. Analyst 2013;138:642–50. https://doi.org/10.1039/c2an36099c.

[138] Wang L, Song Q, Liu Q, He D, Ouyang J. Plasmon-enhanced fluorescence-based core–shell gold nanorods as a near-IR fluorescent turn-on sensor for the highly sensitive detection of pyrophosphate in aqueous solution. Adv Funct Mater 2015;25:7017–27. https://doi.org/10.1002/adfm.201503326.

[139] Sudeep PK, Joseph STS, Thomas KG. Selective detection of cysteine and glutathione using gold nanorods. J Am Chem Soc 2005;127:6516–7. https://doi.org/10.1021/ja051145e.

[140] Huang H, Liu X, Hu T, Chu PK. Ultra-sensitive detection of cysteine by gold nanorod assembly. Biosens Bioelectron 2010;25:2078–83. https://doi.org/10.1016/j.bios.2010.02.003.

[141] Lu L, Xia Y. Enzymatic reaction modulated gold nanorod end-to-end self-assembly for ultrahigh sensitively colorimetric sensing of cholinesterase and organophosphate pesticides in human blood. Anal Chem 2015;87:8584–91. https://doi.org/10.1021/acs.analchem.5b02516.

[142] He W, Huang CZ, Li YF, Xie JP, Yang RG, Zhou PF, et al. One-step label-free optical genosensing system for sequence-specific DNA related to the human immunodeficiency virus based on the measurements of light scattering signals of gold nanorods. Anal Chem 2008;80:8424–30. https://doi.org/10.1021/ac801005d.

[143] Khanal BP, Zubarev ER. Rings of nanorods. Angewandte Chemie International Edition 2007;46:2195–8. https://doi.org/10.1002/anie.200604889.

[144] Pan B, Cui D, Ozkan C, Xu P, Huang T, Li Q, et al. DNA-templated ordered array of gold nanorods in one and two dimensions 2007. https://doi.org/10.1021/jp072335+.

[145] Wang J, Zhang HZ, Li RS, Huang CZ. Localized surface plasmon resonance of gold nanorods and assemblies in the view of biomedical analysis. TrAC Trends in Analytical Chemistry 2016;80:429–43. https://doi.org/10.1016/j.trac.2016.03.015.

[146] Chang L, Khan Y, Li L, Yang N, Yin P, Guo L. Colorimetric detection of HVA by self-assembly of Au nanorods with DNA double helices to give side-by-side and end-to-end structures. RSC Adv 2017;7:13896–903. https://doi.org/10.1039/C6RA28408F.

[147] Caswell KK, Wilson JN, Bunz UHF, Murphy CJ. Preferential end-to-end assembly of gold nanorods by biotin-streptavidin connectors. J Am Chem Soc 2003;125:13914–5. https://doi.org/10.1021/ja037969i.

[148] Wang J, Zhang P, Li CM, Li YF, Huang CZ. A highly selective and colorimetric assay of lysine by molecular-driven gold nanorods assembly. Biosens Bioelectron 2012;34:197–201. https://doi.org/10.1016/j.bios.2012.02.001.

[149] Wang Y, Li YF, Wang J, Sang Y, Huang CZ. End-to-end assembly of gold nanorods by means of oligonucleotide-mercury(II) molecular recognition. Chem Commun (Camb) 2010;46:1332–4. https://doi.org/10.1039/b921464j.

[150] Zhen SJ, Huang CZ, Wang J, Li YF. End-to-end assembly of gold nanorods on the basis of aptamer−protein recognition. The Journal of Physical Chemistry C 2009;113:21543–7. https://doi.org/10.1021/jp905084e.

[151] Funston AM, Novo C, Davis TJ, Mulvaney P. Plasmon coupling of gold nanorods at short distances and in different geometries. Nano Lett 2009;9:1651–8. https://doi.org/10.1021/nl900034v.

[152] Sethi M, Joung G, Knecht MR. Linear assembly of Au nanorods using biomimetic ligands. Langmuir 2009;25:1572–81. https://doi.org/10.1021/la802845b.

[153] Kawamura G, Yang Y, Nogami M. Facile assembling of gold nanorods with large aspect ratio and their surface-enhanced Raman scattering properties. Appl Phys Lett 2007;90. https://doi.org/10.1063/1.2752026.

[154] Shibu Joseph ST, Ipe BI, Pramod P, Thomas KG. Gold nanorods to nanochains: mechanistic investigations on their longitudinal assembly using

α,ω-alkanedithiols and interplasmon coupling. J Phys Chem B 2006;110:150–7. https://doi.org/10.1021/jp0544179.

[155] Zhang L, Chen H, Wang J, Li YF, Wang J, Sang Y, et al. Tetrakis(4-sulfonatophenyl)porphyrin-directed assembly of gold nanocrystals: tailoring the plasmon coupling through controllable gap distances. Small 2010;6:n/a-n/a. https://doi.org/10.1002/smll.201090062.

[156] Chang J-Y, Wu H, Chen H, Ling Y-C, Tan W. Oriented assembly of Au nanorods using biorecognition system. Chem Commun (Camb) 2005:1092–4. https://doi.org/10.1039/b414059a.

[157] Ma W, Kuang H, Xu L, Ding L, Xu C, Wang L, et al. Attomolar DNA detection with chiral nanorod assemblies. Nat Commun 2013;4:2689. https://doi.org/10.1038/ncomms3689.

[158] Wang L, Jin Y, Deng J, Chen G. Gold nanorods-based FRET assay for sensitive detection of Pb2+ using 8-17DNAzyme. Analyst 2011;136:5169. https://doi.org/10.1039/c1an15783c.

[159] Dujardin E, Mann S, Hsin L-B, Wang CRC. DNA-driven self-assembly of gold nanorods. Chemical Communications 2001:1264–5. https://doi.org/10.1039/b102319p.

[160] Mitamura K, Imae T, Saito N, Takai O. Fabrication and self-assembly of hydrophobic gold nanorods. J Phys Chem B 2007;111:8891–8. https://doi.org/10.1021/jp072524s.

[161] Wang L, Zhu Y, Xu L, Chen W, Kuang H, Liu L, et al. Side-by-side and end-to-end gold nanorod assemblies for environmental toxin sensing. Angewandte Chemie 2010;122:5604–7. https://doi.org/10.1002/ange.200907357.

[162] Liz-Marzán LM, Pérez-Juste J, Pastoriza-Santos I. Plasmonics of gold nanorods. considerations for biosensing. NATO Science for Peace and Security Series B: Physics and Biophysics, Springer Verlag; 2008, p. 103–11. https://doi.org/10.1007/978-1-4020-6829-4_9.

[163] Huang H-C, Koria P, Parker SM, Selby L, Megeed Z, Rege K. Optically responsive gold nanorod-polypeptide assemblies. Langmuir 2008;24:14139–44. https://doi.org/10.1021/la802842k.

[164] McLintock A, Hunt N, Wark AW. Controlled side-by-side assembly of gold nanorods and dye molecules into polymer-wrapped SERRS-active clusters. Chem Commun (Camb) 2011;47:3757–9. https://doi.org/10.1039/c0cc04353b.

[165] Gole A, Murphy CJ. Biotin-streptavidin-induced aggregation of gold nanorods: tuning rod-rod orientation. Langmuir 2005;21:10756–62. https://doi.org/10.1021/la0512704.

[166] Rao H, Xue X, Wang H, Xue Z. Gold nanorod etching-based multicolorimetric sensors: strategies and applications. J Mater Chem C Mater 2019;7:4610–21. https://doi.org/10.1039/C9TC00757A.

[167] Lee K-S, El-Sayed MA. Dependence of the enhanced optical scattering efficiency relative to that of absorption for gold metal nanorods on aspect ratio, size, end-cap shape, and medium refractive index. J Phys Chem B 2005;109:20331–8. https://doi.org/10.1021/jp054385p.

[168] Kermanshahian K, Yadegar A, Ghourchian H. Gold nanorods etching as a powerful signaling process for plasmonic multicolorimetric chemo-/biosensors: Strategies and applications. Coord Chem Rev 2021;442:213934. https://doi.org/10.1016/j.ccr.2021.213934.

[169] Zeng J, Zhang Y, Zeng T, Aleisa R, Qiu Z, Chen Y, et al. Anisotropic plasmonic nanostructures for colorimetric sensing. Nano Today 2020;32:100855. https://doi.org/10.1016/j.nantod.2020.100855.

[170] Fahimi-Kashani N, Hormozi-Nezhad MR. Gold nanorod-based chrono-colorimetric sensor arrays: A promising platform for chemical discrimination applications. ACS Omega 2018;3:1386–94. https://doi.org/10.1021/acsomega.7b01780.

[171] Wang G, Chen Z, Chen L. Mesoporous silica-coated gold nanorods: towards sensitive colorimetric sensing of ascorbic acid via target-induced silver overcoating. Nanoscale 2011;3:1756–9. https://doi.org/10.1039/c0nr00863j.

[172] Lin J-M, Huang Y-Q, Liu Z, Lin C-Q, Ma X, Liu J-M. Design of an ultra-sensitive gold nanorod colorimetric sensor and its application based on formaldehyde reducing Ag+. RSC Adv 2015;5:99944–50. https://doi.org/10.1039/C5RA16266A.

[173] Lin T, Wu Y, Li Z, Song Z, Guo L, Fu F. Visual monitoring of food spoilage based on hydrolysis-induced silver metallization of Au nanorods. Anal Chem 2016;88:11022–7. https://doi.org/10.1021/acs.analchem.6b02870.

[174] Yang X, Gao Z. Enzyme-catalysed deposition of ultrathin silver shells on gold nanorods: a universal and highly efficient signal amplification strategy for translating immunoassay into a litmus-type test. Chem Commun (Camb) 2015;51:6928–31. https://doi.org/10.1039/c5cc01286d.

[175] Chen J, Jackson AA, Rotello VM, Nugen SR. Colorimetric detection of escherichia coli based on the enzyme-induced metallization of gold nanorods. Small 2016;12:2469–75. https://doi.org/10.1002/smll.201503682.

[176] Zhang B, Xia Y. Etching of gold nanorods: The effects of diameter on analytical performances. Chinese Chemical Letters 2019;30:1663–6. https://doi.org/10.1016/j.cclet.2019.06.038.

[177] Chandrasekar G, Mougin K, Haidara H, Vidal L, Gnecco E. Shape and size transformation of gold nanorods (GNRs) via oxidation process: A reverse growth mechanism. Appl Surf Sci 2011;257:4175–9. https://doi.org/10.1016/j.apsusc.2010.12.015.

[178] Tsung C-K, Kou X, Shi Q, Zhang J, Yeung MH, Wang J, et al. Selective shortening of single-crystalline gold nanorods by mild oxidation. J Am Chem Soc 2006;128:5352–3. https://doi.org/10.1021/ja060447t.

[179] Weng G, Li J, Zhu J, Zhao J. Plasmonic sensing of CTAB in gold nanorods solution based on Cu(II) ions-mediated H2O2 etching effect. Journal of Nanoparticle Research 2014;16:2728. https://doi.org/10.1007/s11051-014-2728-0.

[180] Mao Y, Li J, Yan J, Ma Y, Song Y, Tian T, et al. A portable visual detection method based on a target-responsive DNA hydrogel and color change of gold nanorods. Chem Commun (Camb) 2017;53:6375–8. https://doi.org/10.1039/c7cc01360d.

[181] Zhu Q, Wu J, Zhao J, Ni W. Role of bromide in hydrogen peroxide oxidation of CTAB-stabilized gold nanorods in aqueous solutions. Langmuir 2015;31:4072–7. https://doi.org/10.1021/acs.langmuir.5b00137.

[182] Sreeprasad TS, Samal AK, Pradeep T. Body- or tip-controlled reactivity of gold nanorods and their conversion to particles through other anisotropic structures. Langmuir 2007;23:9463–71. https://doi.org/10.1021/la700851x.

[183] Gisbert-González JM, Oliver-Pardo M V., Briega-Martos V, Feliu JM, Herrero E. Charge effects on the behavior of CTAB adsorbed on Au(111) electrodes in aqueous solutions. Electrochim Acta 2021;370:137737. https://doi.org/10.1016/j.electacta.2021.137737.

[184] Wang ZL, Gao RP, Nikoobakht B, El-Sayed MA. Surface reconstruction of the unstable {110} surface in gold nanorods. J Phys Chem B 2000;104:5417–20. https://doi.org/10.1021/jp000800w.

[185] Khelfa A, Meng J, Byun C, Wang G, Nelayah J, Ricolleau C, et al. Selective shortening of gold nanorods: when surface functionalization dictates the reactivity of nanostructures. Nanoscale 2020;12:22658–67. https://doi.org/10.1039/d0nr06326f.

[186] Zhang Z, Wang H, Chen Z, Wang X, Choo J, Chen L. Plasmonic colorimetric sensors based on etching and growth of noble metal nanoparticles: Strategies and applications. Biosens Bioelectron 2018;114:52–65. https://doi.org/10.1016/j.bios.2018.05.015.

[187] Rex M, Hernandez FE, Campiglia AD. Pushing the limits of mercury sensors with gold nanorods. Anal Chem 2006;78:445–51. https://doi.org/10.1021/ac051166r.

[188] Chemnasiri W, Hernandez FE. Gold nanorod-based mercury sensor using functionalized glass substrates. Sens Actuators B Chem 2012;173:322–8. https://doi.org/10.1016/j.snb.2012.07.002.

[189] Duan Q-Q, Zhou J-L, Li P-W, Sun L, Zhuo K, Zhang Y-X, et al. High-sensitivity mercury ion detection system using unmodified gold nanorods. Chinese Journal of Analytical Chemistry 2018;46:e1874–9. https://doi.org/10.1016/S1872-2040(18)61112-0.

[190] Zou R, Guo X, Yang J, Li D, Peng F, Zhang L, et al. Selective etching of gold nanorods by ferric chloride at room temperature. CrystEngComm 2009;11:2797. https://doi.org/10.1039/b911902g.

[191] Thatai S, Khurana P, Prasad S, Kumar D. A new way in nanosensors: Gold nanorods for sensing of Fe(III) ions in aqueous media. Microchemical Journal 2014;113:77–82. https://doi.org/10.1016/j.microc.2013.11.004.

[192] Alex SA, Satija J, Khan MA, Bhalerao GM, Chakravarty S, Kasilingam B, et al. Etching-based transformation of dumbbell-shaped gold nanorods facilitated by hexavalent chromium and their possible application as a plasmonic sensor. Analytical Methods 2015;7:5583–92. https://doi.org/10.1039/c5ay00935a.

[193] Li F-M, Liu J-M, Wang X-X, Lin L-P, Cai W-L, Lin X, et al. Non-aggregation based label free colorimetric sensor for the detection of Cr (VI) based on selective etching of gold nanorods. Sens Actuators B Chem 2011;155:817–22. https://doi.org/10.1016/j.snb.2011.01.054.

[194] Alex SA, Chandrasekaran N, Mukherjee A. Using gold nanorod-based colorimetric sensor for determining chromium in biological samples. J Mol Liq 2018;264:119–26. https://doi.org/10.1016/j.molliq.2018.05.056.

[195] Zhang Z, Chen Z, Qu C, Chen L. Highly sensitive visual detection of copper ions based on the shape-dependent LSPR spectroscopy of gold nanorods. Langmuir 2014;30:3625–30. https://doi.org/10.1021/la500106a.

[196] Sreeprasad TS, Samal AK, Pradeep T. Reactivity and resizing of gold nanorods in presence of Cu2+. Bulletin of Materials Science 2008;31:219–24. https://doi.org/10.1007/s12034-008-0039-8.

[197] Chen Z, Zhang Z, Qu C, Pan D, Chen L. Highly sensitive label-free colorimetric sensing of nitrite based on etching of gold nanorods. Analyst 2012;137:5197–200. https://doi.org/10.1039/c2an35787a.

[198] He Z, Zhang L, Peng G, Wang G, Liang X. Chemical redox-modulated etching of plasmonic nanoparticles for nitrite detection: Comparison among gold nanosphere, nanorod, and nanotriangle. J Anal Test 2021;5:350–9. https://doi.org/10.1007/s41664-021-00153-4.

[199] Wen X, Shuai H, Min L. Precise modulation of gold nanorods aspect ratio based on localized surface plasmon resonance. Opt Mater (Amst) 2016;60:324–30. https://doi.org/10.1016/j.optmat.2016.08.008.

[200] Shan G, Zheng S, Chen S, Chen Y, Liu Y. Detection of label-free H2O2 based on sensitive Au nanorods as sensor. Colloids Surf B Biointerfaces 2013;102:327–30. https://doi.org/10.1016/j.colsurfb.2012.07.041.

[201] Zou BQ, Zhang HZ, Fu Z, Zhan T, Wang J. Size-modulated optical property of gold nanorods for sensitive and colorimetric detection of thiourea in fruit juice. Talanta 2021;225:121965. https://doi.org/10.1016/j.talanta.2020.121965.

[202] Liu J-M, Jiao L, Lin L-P, Cui M-L, Wang X-X, Zhang L-H, et al. Non-aggregation based label free colorimetric sensor for the detection of Cu2+ based on catalyzing etching of gold nanorods by dissolve oxygen. Talanta 2013;117:425–30. https://doi.org/10.1016/j.talanta.2013.09.004.

[203] Lee S, Nam Y-S, Choi S-H, Lee Y, Lee K-B. Highly sensitive photometric determination of cyanide based on selective etching of gold nanorods. Microchimica Acta 2016;183:3035–41. https://doi.org/10.1007/s00604-016-1952-y.

[204] Lan Y-J, Lin Y-W. A non-aggregation colorimetric method for trace lead(ii) ions based on the leaching of gold nanorods. Anal Methods 2014;6:7234–42. https://doi.org/10.1039/c4ay00972j.

[205] Sepahvand M, Ghasemi F, Seyed Hosseini HM. Thiol-mediated etching of gold nanorods as a neoteric strategy for room-temperature and multicolor detection of nitrite and nitrate. Anal Methods 2021;13:4370–8. https://doi.org/10.1039/d1ay01117k.

[206] Chen L, Lu L, Wang S, Xia Y. Valence states modulation strategy for picomole level assay of Hg2+ in drinking and environmental water by directional self-assembly of gold nanorods. ACS Sens 2017;2:781–8. https://doi.org/10.1021/acssensors.7b00149.

[207] Zhu J, Yu Y-Q, Li J-J, Zhao J-W. Colorimetric detection of lead(ii) ions based on accelerating surface etching of gold nanorods to nanospheres: the effect of sodium thiosulfate. RSC Adv 2016;6:25611–9. https://doi.org/10.1039/c5ra26560f.

[208] Yu L, Song Z, Peng J, Yang M, Zhi H, He H. Progress of gold nanomaterials for colorimetric sensing based on different strategies. TrAC Trends in

Analytical Chemistry 2020;127:115880. https://doi.org/10.1016/j.trac.2020.115880.

[209] Ni W, Kou X, Yang Z, Wang J. Tailoring longitudinal surface plasmon wavelengths, scattering and absorption cross sections of gold nanorods. ACS Nano 2008;2:677–86. https://doi.org/10.1021/nn7003603.

[210] Kedia A, Kumar PS. Halide ion induced tuning and self-organization of gold nanostars. RSC Adv 2014;4:4782–90. https://doi.org/10.1039/C3RA43976C.

[211] Weng G, Dong X, Li J, Zhao J. Halide ions can trigger the oxidative etching of gold nanorods with the iodide ions being the most efficient. J Mater Sci 2016;51:7678–90. https://doi.org/10.1007/s10853-016-0050-1.

[212] Zhang Z, Chen Z, Cheng F, Zhang Y, Chen L. Iodine-mediated etching of gold nanorods for plasmonic sensing of dissolved oxygen and salt iodine. Analyst 2016;141:2955–61. https://doi.org/10.1039/C5AN02633D.

[213] Zhang Z, Chen Z, Cheng F, Zhang Y, Chen L. Highly sensitive on-site detection of glucose in human urine with naked eye based on enzymatic-like reaction mediated etching of gold nanorods. Biosens Bioelectron 2017;89:932–6. https://doi.org/10.1016/j.bios.2016.09.090.

[214] Zhang Z, Chen Z, Wang S, Cheng F, Chen L. Iodine-mediated etching of gold nanorods for plasmonic ELISA based on colorimetric detection of alkaline phosphatase. ACS Appl Mater Interfaces 2015;7:27639–45. https://doi.org/10.1021/acsami.5b07344.

[215] Zhang Z, Chen Z, Chen L. Ultrasensitive visual sensing of molybdate based on enzymatic-like etching of gold nanorods. Langmuir 2015;31:9253–9. https://doi.org/10.1021/acs.langmuir.5b02113.

[216] Fang B, Xu S, Huang Y, Su F, Huang Z, Fang H, et al. Gold nanorods etching-based plasmonic immunoassay for qualitative and quantitative detection of aflatoxin M1 in milk. Food Chem 2020;329:127160. https://doi.org/10.1016/j.foodchem.2020.127160.

[217] Sun Y, Li S, Chen R, Wu P, Liang J. Ultrasensitive and rapid detection of T-2 toxin using a target-responsive DNA hydrogel. Sens Actuators B Chem 2020;311:127912. https://doi.org/10.1016/j.snb.2020.127912.

[218] Qin X, Yuan C-L, Shi R, Wang S-Z, Wang Y-L. Colorimetric detection of dopamine based on iodine-mediated etching of gold nanorods. Chinese Journal of Analytical Chemistry 2021;49:60–7. https://doi.org/10.1016/S1872-2040(20)60073-1.

[219] Li Y, Luo G, Qing Z, Li X, Zou Z, Yang R. Colorimetric aminotriazole assay based on catalase deactivation-dependent longitudinal etching of gold nanorods. Microchimica Acta 2019;186:565. https://doi.org/10.1007/s00604-019-3677-1.

[220] Liu JJ, Yan HH, Yuan D, Zhang Q, Li CM, Huang CZ, et al. The synergistic effect enhanced chemical etching of gold nanorods for the rapid and sensitive detection of biomarks. Talanta 2020;219:121203. https://doi.org/10.1016/j.talanta.2020.121203.

[221] Wang H, Rao H, Xue X, An P, Gao M, Luo M, et al. Target-mediated surface chemistry of gold nanorods for breaking the low color resolution limitation of monocolorimetric sensor. Anal Chim Acta 2020;1097:222–9. https://doi.org/10.1016/j.aca.2019.11.022.

[222] Cheng X, Huang Y, Yuan C, Dai K, Jiang H, Ma J. Colorimetric detection of α-glucosidase activity based on the etching of gold nanorods and its application to screen anti-diabetic drugs. Sens Actuators B Chem 2019;282:838–43. https://doi.org/10.1016/j.snb.2018.11.097.

[223] Qing Z, Li Y, Li Y, Luo G, Hu J, Zou Z, et al. Thiol-suppressed I2-etching of AuNRs: acetylcholinesterase-mediated colorimetric detection of organophosphorus pesticides. Microchimica Acta 2020;187:497. https://doi.org/10.1007/s00604-020-04486-2.

[224] Liu B-W, Huang P-C, Wu F-Y. Smartphone colorimetric assay of acid phosphatase based on a controlled iodine-mediated etching of gold nanorods. Anal Bioanal Chem 2020;412:8051–9. https://doi.org/10.1007/s00216-020-02954-5.

[225] Haber F, Weiss J. The catalytic decomposition of hydrogen peroxide by iron salts. Proc R Soc Lond A Math Phys Sci 1934;147:332–51. https://doi.org/10.1098/rspa.1934.0221.

[226] Meyerstein D. Re-examining Fenton and Fenton-like reactions. Nature Reviews Chemistry 2021 5:9 2021;5:595–7. https://doi.org/10.1038/s41570-021-00310-4.

[227] Chen Z, Liu R, Wang S, Qu C, Chen L, Wang Z. Colorimetric sensing of copper(ii) based on catalytic etching of gold nanorods. RSC Adv 2013;3:13318. https://doi.org/10.1039/c3ra40559a.

[228] Sharma P, Jha AB, Dubey RS, Pessarakli M. Reactive oxygen species, oxidative damage, and antioxidative defense mechanism in plants under stressful conditions. J Bot 2012;2012:1–26. https://doi.org/10.1155/2012/217037.

[229] Lee HJ, Lee H, Lee C. Degradation of diclofenac and carbamazepine by the copper(II)-catalyzed dark and photo-assisted Fenton-like systems. Chemical

Engineering Journal 2014;245:258–64. https://doi.org/10.1016/J.cej.2014.02.037.

[230] Ling SK, Wang S, Peng Y. Oxidative degradation of dyes in water using Co2+/H2O2 and Co2+/peroxymonosulfate. J Hazard Mater 2010;178:385–9. https://doi.org/10.1016/j.jhazmat.2010.01.091.

[231] Zhang Z, Chen Z, Pan D, Chen L. Fenton-like reaction-mediated etching of gold nanorods for visual detection of Co2+. Langmuir 2015;31:643–50. https://doi.org/10.1021/la504256c.

[232] Liu X, Zhang S, Tan P, Zhou J, Huang Y, Nie Z, et al. A plasmonic blood glucose monitor based on enzymatic etching of gold nanorods. Chemical Communications 2013;49:1856–8. https://doi.org/10.1039/C3CC38476D.

[233] Lee H, Lee HJ, Sedlak DL, Lee C. pH-Dependent reactivity of oxidants formed by iron and copper-catalyzed decomposition of hydrogen peroxide. Chemosphere 2013;92:652–8. https://doi.org/10.1016/j.chemosphere.2013.01.073.

[234] Bokare AD, Choi W. Zero-valent aluminum for oxidative degradation of aqueous organic pollutants. Environ Sci Technol 2009;43:7130–5. https://doi.org/10.1021/es9013823.

[235] Wen G, Luo Y, Liang A, Jiang Z. Autocatalytic oxidization of nanosilver and its application to spectral analysis. Scientific Reports 2014 4:1 2014;4:1–7. https://doi.org/10.1038/srep03990.

[236] Bishkul H, Khoshfetrat SM, Noori A, Mehrgardi MA, Mousavi MF. Rich-color visual genotyping of single-nucleotide polymorphisms based on platinum nanoparticle–induced etching of gold nanorods. Emergent Mater 2019;2:351–61. https://doi.org/10.1007/s42247-019-00049-1.

[237] Ma X, Chen Z, Kannan P, Lin Z, Qiu B, Guo L. Gold nanorods as colorful chromogenic substrates for semiquantitative detection of nucleic acids, proteins, and small molecules with the naked eye. Anal Chem 2016;88:3227–34. https://doi.org/10.1021/acs.analchem.5b04621.

[238] Yang H, Liu A, Wei M, Liu Y, Lv B, Wei W, et al. Visual, label-free telomerase activity monitor via enzymatic etching of gold nanorods. Anal Chem 2017;89:12094–100. https://doi.org/10.1021/acs.analchem.7b02608.

[239] Yuan D, Yan H, Liu J, Liu J, Li C, Wang J. A fast and colorimetric sensor array for the discrimination of ribonucleotides in human urine samples by gold nanorods. Chinese Chemical Letters 2020;31:455–8. https://doi.org/10.1016/j.cclet.2019.07.067.

[240] Wen S, Huang M, Cheng R, Gao J, Wang J. Silver-coated gold nanorods as optical probes for the sensitive detection of ascorbic acid in tablets. Chemosensors 2022;10:543. https://doi.org/10.3390/chemosensors10120543.

[241] Wang X-X, Liu J-M, Jiang S-L, Jiao L, Lin L-P, Cui M-L, et al. Non-aggregation colorimetric sensor for detecting vitamin C based on surface plasmon resonance of gold nanorods. Sens Actuators B Chem 2013;182:205–10. https://doi.org/10.1016/j.snb.2013.02.059.

[242] Liu J-M, Jiao L, Zhang L-H, Zheng Z-Y, Wang X-X, Lin L-P, et al. Design of highly sensitive non-aggregation colorimetric sensor and its application based on inhibiting vitamin C reducing Hg2+. Sens Actuators B Chem 2013;188:613–20. https://doi.org/10.1016/j.snb.2013.07.054.

[243] Zhao Y, Zuo X, Li Q, Chen F, Chen Y-R, Deng J, et al. Nucleic acids analysis. Sci China Chem 2021;64:171–203. https://doi.org/10.1007/s11426-020-9864-7.

[244] Blanco A, Blanco G. Nucleic acids. Med Biochem, Elsevier; 2017, p. 121–40. https://doi.org/10.1016/B978-0-12-803550-4.00006-9.

[245] Blackstock JC. Nucleic acids. Guide to Biochemistry, Elsevier; 1989, p. 78–90. https://doi.org/10.1016/B978-0-7236-1151-6.50013-3.

[246] Aaron J-J, Trajkovska S. Purines, pyrimidines, and nucleotides. Encyclopedia of Analytical Science, Elsevier; 2005, p. 393–402. https://doi.org/10.1016/B0-12-369397-7/00500-8.

[247] Shen C-H. Nucleic acids. Diagnostic Molecular Biology, Elsevier; 2023, p. 1–26. https://doi.org/10.1016/B978-0-323-91788-9.00005-3.

[248] Das G, Harikrishna S, Gore KR. Influence of sugar modifications on the nucleoside conformation and oligonucleotide stability: A critical review. The Chemical Record 2022;22:e202200174. https://doi.org/10.1002/tcr.202200174.

[249] Watson Jd, Crick Fhc. Molecular structure of nucleic acids: A structure for deoxyribose nucleic acid. Nature 1953;171:737–8. https://doi.org/10.1038/171737a0.

[250] Choi J, Majima T. Conformational changes of non-B DNA. Chem Soc Rev 2011;40:5893. https://doi.org/10.1039/c1cs15153c.

[251] Lander ES, Linton LM, Birren B, Nusbaum C, Zody MC, Baldwin J, et al. Initial sequencing and analysis of the human genome. Nature 2001;409:860–921. https://doi.org/10.1038/35057062.

[252] Wells RD. Non-B DNA conformations, mutagenesis and disease. Trends Biochem Sci 2007;32:271–8. https://doi.org/10.1016/j.tibs.2007.04.003.

[253] Wang G, Vasquez KM. Non-B DNA structure-induced genetic instability. Mutation Research/Fundamental and Molecular Mechanisms of Mutagenesis 2006;598:103–19. https://doi.org/10.1016/j.mrfmmm.2006.01.019.

[254] Zhao J, Bacolla A, Wang G, Vasquez KM. Non-B DNA structure-induced genetic instability and evolution. Cellular and Molecular Life Sciences 2010;67:43–62. https://doi.org/10.1007/s00018-009-0131-2.

[255] Duardo RC, Guerra F, Pepe S, Capranico G. Non-B DNA structures as a booster of genome instability. Biochimie 2023;214:176–92. https://doi.org/10.1016/j.biochi.2023.07.002.

[256] Ghosal G, Muniyappa K. Hoogsteen base-pairing revisited: Resolving a role in normal biological processes and human diseases. Biochem Biophys Res Commun 2006;343:1–7. https://doi.org/10.1016/j.bbrc.2006.02.148.

[257] Moon J, Han JH, Kim DY, Jung M, Kim SK. Effects of deficient of the Hoogsteen base-pairs on the G-quadruplex stabilization and binding mode of a cationic porphyrin. Biochem Biophys Rep 2015;2:29–35. https://doi.org/10.1016/j.bbrep.2015.03.012.

[258] Mergny J-L, Lacroix L, Han X, Leroy J-L, Helene C. Intramolecular Folding of Pyrimidine Oligodeoxynucleotides into an i-DNA Motif. J Am Chem Soc 1995;117:8887–98. https://doi.org/10.1021/ja00140a001.

[259] Frank-Kamenetskii MD, Mirkin SM. Triplex dna structures. Annu Rev Biochem 1995;64:65–95. https://doi.org/10.1146/annurev.bi.64.070195.000433.

[260] Chakraborty S, Sharma S, Maiti PK, Krishnan Y. The poly dA helix: a new structural motif for high performance DNA-based molecular switches. Nucleic Acids Res 2009;37:2810–7. https://doi.org/10.1093/nar/gkp133.

[261] Guiblet WM, Cremona MA, Harris RS, Chen D, Eckert KA, Chiaromonte F, et al. Non-B DNA: a major contributor to small- and large-scale variation in nucleotide substitution frequencies across the genome. Nucleic Acids Res 2021;49:1497–516. https://doi.org/10.1093/nar/gkaa1269.

[262] Gellert M, Lipsett MN, Davies DR. Helix formation by guanylic acid. Proceedings of the National Academy of Sciences 1962;48:2013–8. https://doi.org/10.1073/pnas.48.12.2013.

[263] Sen D, Gilbert W. Formation of parallel four-stranded complexes by guanine-rich motifs in DNA and its implications for meiosis. Nature 1988;334:364–6. https://doi.org/10.1038/334364a0.

[264] Sundquist WI, Klug A. Telomeric DNA dimerizes by formation of guanine tetrads between hairpin loops. Nature 1989;342:825–9. https://doi.org/10.1038/342825a0.

[265] Williamson JR, Raghuraman MK, Cech TR. Monovalent cation-induced structure of telomeric DNA: The G-quartet model. Cell 1989;59:871–80. https://doi.org/10.1016/0092-8674(89)90610-7.

[266] Patel DJ, Phan AT, Kuryavyi V. Human telomere, oncogenic promoter and 5'-UTR G-quadruplexes: diverse higher order DNA and RNA targets for cancer therapeutics. Nucleic Acids Res 2007;35:7429–55. https://doi.org/10.1093/nar/gkm711.

[267] Burge S, Parkinson GN, Hazel P, Todd AK, Neidle S. Quadruplex DNA: sequence, topology and structure. Nucleic Acids Res 2006;34:5402–15. https://doi.org/10.1093/nar/gkl655.

[268] Lane AN, Chaires JB, Gray RD, Trent JO. Stability and kinetics of G-quadruplex structures. Nucleic Acids Res 2008;36:5482–515. https://doi.org/10.1093/nar/gkn517.

[269] Mishra SK, Jain N, Shankar U, Tawani A, Sharma TK, Kumar A. Characterization of highly conserved G-quadruplex motifs as potential drug targets in Streptococcus pneumoniae. Sci Rep 2019;9:1791. https://doi.org/10.1038/s41598-018-38400-x.

[270] Johnson JE, Smith JS, Kozak ML, Johnson FB. In vivo veritas: Using yeast to probe the biological functions of G-quadruplexes. Biochimie 2008;90:1250–63. https://doi.org/10.1016/j.biochi.2008.02.013.

[271] Rawal P, Kummarasetti VBR, Ravindran J, Kumar N, Halder K, Sharma R, et al. Genome-wide prediction of G4 DNA as regulatory motifs: Role in , Escherichia coli, global regulation. Genome Res 2006;16:644–55. https://doi.org/10.1101/gr.4508806.

[272] Huppert JL. Hunting G-quadruplexes. Biochimie 2008;90:1140–8. https://doi.org/10.1016/j.biochi.2008.01.014.

[273] Huppert JL, Balasubramanian S. G-quadruplexes in promoters throughout the human genome. Nucleic Acids Res 2007;35:406–13. https://doi.org/10.1093/nar/gkl1057.

[274] Lipps HJ, Rhodes D. G-quadruplex structures: in vivo evidence and function. Trends Cell Biol 2009;19:414–22. https://doi.org/10.1016/j.tcb.2009.05.002.

[275] Maizels N, Gray LT. The G4 genome. PLoS Genet 2013;9:e1003468. https://doi.org/10.1371/journal.pgen.1003468.

[276] Sekibo DAT, Fox KR. The effects of DNA supercoiling on G-quadruplex formation. Nucleic Acids Res 2017;45:12069–79. https://doi.org/10.1093/nar/gkx856.

[277] Valeeva LR, Abdulkina LR, Agabekian IA, Shakirov E V. Telomere biology and ribosome biogenesis: structural and functional interconnections. Biochemistry and Cell Biology 2023;101:394–409. https://doi.org/10.1139/bcb-2022-0383.

[278] Blackburn EH, Epel ES, Lin J. Human telomere biology: A contributory and interactive factor in aging, disease risks, and protection. Science 2015;350:1193–8. https://doi.org/10.1126/science.aab3389.

[279] Revy P, Kannengiesser C, Bertuch AA. Genetics of human telomere biology disorders. Nat Rev Genet 2023;24:86–108. https://doi.org/10.1038/s41576-022-00527-z.

[280] Egan ED, Collins K. Biogenesis of telomerase ribonucleoproteins. RNA 2012;18:1747–59. https://doi.org/10.1261/rna.034629.112.

[281] Roake CM, Artandi SE. Regulation of human telomerase in homeostasis and disease. Nat Rev Mol Cell Biol 2020;21:384–97. https://doi.org/10.1038/s41580-020-0234-z.

[282] Kocak H, Ballew BJ, Bisht K, Eggebeen R, Hicks BD, Suman S, et al. Hoyeraal-Hreidarsson syndrome caused by a germline mutation in the TEL patch of the telomere protein TPP1. Genes Dev 2014;28:2090–102. https://doi.org/10.1101/gad.248567.114.

[283] Armanios MY, Chen JJ-L, Cogan JD, Alder JK, Ingersoll RG, Markin C, et al. Telomerase mutations in families with idiopathic pulmonary fibrosis. N Engl J Med 2007;356:1317–26. https://doi.org/10.1056/NEJMoa066157.

[284] Armanios M, Blackburn EH. The telomere syndromes. Nature Reviews Genetics 2012 13:10 2012;13:693–704. https://doi.org/10.1038/nrg3246.

[285] Vy Thi Le T, Han S, Chae J, Park H-J. G-Quadruplex binding ligands: From naturally occurring to rationally designed molecules. Curr Pharm Des 2012;18:1948–72. https://doi.org/10.2174/138161212799958431.

[286] Chaires JB. Human telomeric G-quadruplex: thermodynamic and kinetic studies of telomeric quadruplex stability. FEBS J 2010;277:1098–106. https://doi.org/10.1111/j.1742-4658.2009.07462.x.

[287] Chambers VS, Marsico G, Boutell JM, Di Antonio M, Smith GP, Balasubramanian S. High-throughput sequencing of DNA G-quadruplex structures in the human genome. Nat Biotechnol 2015;33:877–81. https://doi.org/10.1038/nbt.3295.

[288] Zhou G, Liu X, Li Y, Xu S, Ma C, Wu X, et al. Telomere targeting with a novel G-quadruplex-interactive ligand BRACO-19 induces T-loop disassembly and telomerase displacement in human glioblastoma cells. Oncotarget 2016;7:14925–39. https://doi.org/10.18632/oncotarget.7483.

[289] Yang D. G-Quadruplex DNA and RNA. Methods Mol Biol 2019;2035:1–24. https://doi.org/10.1007/978-1-4939-9666-7_1.

[290] Kim N. The Interplay between G-quadruplex and transcription. Curr Med Chem 2019;26:2898–917. https://doi.org/10.2174/0929867325666171229132619.

[291] Paeschke K, Burkovics P. Mgs1 function at G-quadruplex structures during DNA replication. Curr Genet 2021;67:225–30. https://doi.org/10.1007/s00294-020-01128-1.

[292] Bryan TM. Mechanisms of DNA replication and repair: Insights from the study of G-Quadruplexes. Molecules 2019;24. https://doi.org/10.3390/molecules24193439.

[293] Valton A-L, Prioleau M-N. G-Quadruplexes in DNA replication: A problem or a necessity? Trends Genet 2016;32:697–706. https://doi.org/10.1016/j.tig.2016.09.004.

[294] Lerner LK, Sale JE. Replication of G Quadruplex DNA. Genes (Basel) 2019;10:95. https://doi.org/10.3390/genes10020095.

[295] Londoño-Vallejo JA. Telomeres, epigenetics, and aging. Epigenetics of Aging, New York, NY: Springer New York; 2010, p. 205–25. https://doi.org/10.1007/978-1-4419-0639-7_12.

[296] Gunes C, Avila AI, Rudolph KL. Telomeres in cancer. Differentiation 2018;99:41–50. https://doi.org/10.1016/j.diff.2017.12.004.

[297] Mondello C, Scovassi AI. Telomeres, telomerase, and apoptosis. Https://DoiOrg/101139/O04-048 2011;82:498–507. https://doi.org/10.1139/O04-048.

[298] Xu L, Li S, Stohr BA. The role of telomere biology in cancer. Annu Rev Pathol 2013;8:49–78. https://doi.org/10.1146/annurev-pathol-020712-164030.

[299] Cea V, Cipolla L, Sabbioneda S. Replication of structured DNA and its implication in epigenetic stability. Front Genet 2015;6:209. https://doi.org/10.3389/fgene.2015.00209.

[300] Maizels N. G4-associated human diseases. EMBO Rep 2015;16:910–22. https://doi.org/10.15252/embr.201540607.

[301] Axelrad MD, Budagov T, Atzmon G. Telomere length and telomerase activity; a Yin and Yang of cell senescence. J Vis Exp 2013:e50246. https://doi.org/10.3791/50246.

[302] Takahashi S, Bhowmik S, Sato S, Takenaka S, Sugimoto N. Replication control of human telomere G-Quadruplex DNA by G-Quadruplex ligands dependent on solution environment. Life 2022;12:553. https://doi.org/10.3390/life12040553.

[303] Oganesian L, Bryan TM. Physiological relevance of telomeric G-quadruplex formation: a potential drug target. BioEssays 2007;29:155–65. https://doi.org/10.1002/bies.20523.

[304] Huppert JL. Prevalence of quadruplexes in the human genome. Nucleic Acids Res 2005;33:2908–16. https://doi.org/10.1093/nar/gki609.

[305] Todd AK. Highly prevalent putative quadruplex sequence motifs in human DNA. Nucleic Acids Res 2005;33:2901–7. https://doi.org/10.1093/nar/gki553.

[306] Olovnikov AM. A theory of marginotomy. J Theor Biol 1973;41:181–90. https://doi.org/10.1016/0022-5193(73)90198-7.

[307] Blackburn EH, Szostak JW. The molecular structure of centromeres and telomeres. Annu Rev Biochem 1984;53:163–94. https://doi.org/10.1146/annurev.bi.53.070184.001115.

[308] Greider CW, Blackburn EH. Identification of a specific telomere terminal transferase activity in tetrahymena extracts. Cell 1985;43:405–13. https://doi.org/10.1016/0092-8674(85)90170-9.

[309] Shippen-Lentz D, Blackburn EH. Functional evidence for an RNA template in telomerase. Science (1979) 1990;247:546–52. https://doi.org/10.1126/science.1689074.

[310] Shay JW, Bacchetti S. A survey of telomerase activity in human cancer. Eur J Cancer 1997;33:787–91. https://doi.org/10.1016/S0959-8049(97)00062-2.

[311] Zahler AM, Williamson JR, Cech TR, Prescott DM. Inhibition of telomerase by G-quartet DNA structures. Nature 1991;350:718–20. https://doi.org/10.1038/350718a0.

[312] Schaffitzel C, Berger I, Postberg J, Hanes J, Lipps HJ, Plückthun A. In vitro generated antibodies specific for telomeric guanine-quadruplex DNA react with Stylonychia lemnae macronuclei. Proceedings of the National Academy of Sciences 2001;98:8572–7. https://doi.org/10.1073/pnas.141229498.

[313] Paeschke K, Simonsson T, Postberg J, Rhodes D, Lipps HJ. Telomere end-binding proteins control the formation of G-quadruplex DNA structures in vivo. Nature Structural & Molecular Biology 2005 12:10 2005;12:847–54. https://doi.org/10.1038/nsmb982.

[314] Duquette ML, Handa P, Vincent JA, Taylor AF, Maizels N. Intracellular transcription of G-rich DNAs induces formation of G-loops, novel structures containing G4 DNA. Genes Dev 2004;18:1618–29. https://doi.org/10.1101/gad.1200804.

[315] Granotier C. Preferential binding of a G-quadruplex ligand to human chromosome ends. Nucleic Acids Res 2005;33:4182–90. https://doi.org/10.1093/nar/gki722.

[316] Sen D, Gilbert W. A sodium-potassium switch in the formation of four-stranded G4-DNA. Nature 1990;344:410–4. https://doi.org/10.1038/344410a0.

[317] Miura T, Benevides JM, Thomas GJ. A phase diagram for sodium and potassium ion control of polymorphism in telomeric DNA. J Mol Biol 1995;248:233–8. https://doi.org/10.1016/S0022-2836(95)80046-8.

[318] Harper L, Golubovskaya I, Cande WZ. A bouquet of chromosomes. J Cell Sci 2004;117:4025–32. https://doi.org/10.1242/jcs.01363.

[319] Loidl J, Scherthan H. Organization and pairing of meiotic chromosomes in the ciliate Tetrahymena thermophila. J Cell Sci 2004;117:5791–801. https://doi.org/10.1242/jcs.01504.

[320] Neumann AA, Reddel RR. Telomere maintenance and cancer ? look, no telomerase. Nature Reviews Cancer 2002 2:11 2002;2:879–84. https://doi.org/10.1038/nrc929.

[321] Han H, Hurley LH. G-quadruplex DNA: A potential target for anti-cancer drug design. Trends Pharmacol Sci 2000;21:136–42. https://doi.org/10.1016/s0165-6147(00)01457-7.

[322] Zhang N, Phan AT, Patel DJ. (3 + 1) assembly of three human telomeric repeats into an asymmetric dimeric G-Quadruplex. J Am Chem Soc 2005;127:17277–85. https://doi.org/10.1021/ja0543090.

[323] Griffith JD, Comeau L, Rosenfield S, Stansel RM, Bianchi A, Moss H, et al. Mammalian telomeres end in a large duplex loop. Cell 1999;97:503–14. https://doi.org/10.1016/S0092-8674(00)80760-6.

[324] Lipps HJ, Gruissem W, Prescott DM. Higher order DNA structure in macronuclear chromatin of the hypotrichous ciliate Oxytricha nova. Proceedings of the National Academy of Sciences 1982;79:2495–9. https://doi.org/10.1073/pnas.79.8.2495.

[325] Xu Y, Noguchi Y, Sugiyama H. The new models of the human telomere d[AGGG(TTAGGG)3] in K+ solution. Bioorg Med Chem 2006;14:5584–91. https://doi.org/10.1016/j.bmc.2006.04.033.

[326] Ambrus A, Chen D, Dai J, Bialis T, Jones RA, Yang D. Human telomeric sequence forms a hybrid-type intramolecular G-quadruplex structure with mixed parallel/antiparallel strands in potassium solution. Nucleic Acids Res 2006;34:2723–35. https://doi.org/10.1093/nar/gkl348.

[327] Parkinson GN, Lee MPH, Neidle S. Crystal structure of parallel quadruplexes from human telomeric DNA. Nature 2002 417:6891 2002;417:876–80. https://doi.org/10.1038/nature755.

[328] Chatterjee SK, Zetter BR. Cancer biomarkers: knowing the present and predicting the future. Future Oncology 2005;1:37–50. https://doi.org/10.1517/14796694.1.1.37.

[329] Jafri MA, Ansari SA, Alqahtani MH, Shay JW. Roles of telomeres and telomerase in cancer, and advances in telomerase-targeted therapies. Genome Med 2016;8:69. https://doi.org/10.1186/s13073-016-0324-x.

[330] Wang D, Xue W, Ren X, Xu Z. A review on sensing mechanisms and strategies for telomerase activity detection. TrAC Trends in Analytical Chemistry 2021;134:116115. https://doi.org/10.1016/j.trac.2020.116115.

[331] Eom G, Kim H, Hwang A, Son H, Choi Y, Moon J, et al. Nanogap-rich Au nanowire SERS sensor for ultrasensitive telomerase activity detection: Application to gastric and breast cancer tissues diagnosis. Adv Funct Mater 2017;27:1701832. https://doi.org/10.1002/adfm.201701832.

[332] Chu Y, Deng A-P, Wang W, Zhu J-J. Concatenated catalytic hairpin assembly/hyperbranched hybridization chain reaction based enzyme-free signal amplification for the sensitive photoelectrochemical detection of human telomerase RNA. Anal Chem 2019;91:3619–27. https://doi.org/10.1021/acs.analchem.8b05610.

[333] Liu L, Chang Y, Ji X, Chen J, Zhang M, Yang S. Surface-tethered electrochemical biosensor for telomerase detection by integration of homogeneous extension and hybridization reactions. Talanta 2023;253:123597. https://doi.org/10.1016/j.talanta.2022.123597.

[334] Chen W, Wang L, He R, Xu X, Jiang W. Convertible DNA ends-based silver nanoprobes for colorimetric detection human telomerase activity. Talanta 2018;178:458–63. https://doi.org/10.1016/j.talanta.2017.09.057.

[335] Luo X, Wan Y, Wang K, Wei Q, Yu Z, Chen L, et al. Digital CRISPR/Cas12a-based platform for precise quantification of telomerase activity. Sens Actuators B Chem 2023;394:134374. https://doi.org/10.1016/j.snb.2023.134374.

[336] Luo S, Zhang Y, Situ B, Zheng L. Fluorescence sensing telomerase activity: From extracellular detection to in situ imaging. Sens Actuators B Chem 2018;273:853–61. https://doi.org/10.1016/j.snb.2018.06.088.

[337] Mayuri S, Jha NS. Fluorescent copper conjugated curcumin cysteine nanoprobe for selective determination of Fe3+ and G-quadruplex DNA. Microchimica Acta 2023;190:17. https://doi.org/10.1007/s00604-022-05594-x.

[338] Ahmed LR, Gilmanova L, Pan C-T, Kaskel S, EL-Mahdy AFM. Hollow spherical covalent organic frameworks from nonplanar or planar monomers for the fluorescence detection of telomere DNA: Role of the 2-(2-Azidoethoxy)ethoxy group. ACS Appl Polym Mater 2022;4:9132–43. https://doi.org/10.1021/acsapm.2c01460.

[339] Zhao J, Zhai Q. A highly selective switch-on fluorescence sensor targeting telomeric dimeric G-quadruplex. Bioorg Med Chem Lett 2021;40:127971. https://doi.org/10.1016/j.bmcl.2021.127971.

[340] Javan Kouzegaran V, Farhadi K, Forough M, Bahram M, Persil Çetinkol Ö. Highly-sensitive and fast detection of human telomeric G-Quadruplex DNA based on a hemin-conjugated fluorescent metal-organic framework platform. Biosens Bioelectron 2021;178:112999. https://doi.org/10.1016/j.bios.2021.112999.

[341] Chen X, Deng Y, Cao G, Liu X, Gu T, Feng R, et al. An ultrasensitive and point-of-care sensor for the telomerase activity detection. Anal Chim Acta 2021;1146:61–9. https://doi.org/10.1016/j.aca.2020.11.037.

[342] Shen Y, Gong J, Li S, Liu C, Zhou L, Sheng J, et al. Enzyme-free dual-DNA walker based on catalytic hairpin assembled DNAzyme for sensing telomerase activity. Sens Actuators B Chem 2021;329:129078. https://doi.org/10.1016/j.snb.2020.129078.

[343] Xu X, Wang L, Li K, Huang Q, Jiang W. A smart DNA tweezer for detection of human telomerase activity. Anal Chem 2018;90:3521–30. https://doi.org/10.1021/acs.analchem.7b05373.

[344] Wang Y-Q, Hu M-H, Guo R-J, Chen S-B, Huang Z-S, Tan J-H. Tuning the selectivity of a commercial cyanine nucleic acid dye for preferential sensing of hybrid telomeric G-quadruplex DNA. Sens Actuators B Chem 2018;266:187–94. https://doi.org/10.1016/j.snb.2018.03.125.

[345] Bag SS, Pradhan MK, Talukdar S. Tetrazolylpyrene unnatural nucleoside as a human telomeric multimeric G-quadruplex selective switch-on fluorescent sensor. Org Biomol Chem 2017;15:10145–50. https://doi.org/10.1039/c7ob02433a.

[346] Xu J, Wang Y, Yang L, Gao Y, Li B, Jin Y. A cytometric assay for ultrasensitive and robust detection of human telomerase RNA based on toehold strand displacement. Biosens Bioelectron 2017;87:1071–6. https://doi.org/10.1016/j.bios.2016.08.038.

[347] Gao Y, Xu J, Li B, Jin Y. Nanoparticle-aided amplification of fluorescence polarization for ultrasensitively monitoring activity of telomerase. ACS Appl Mater Interfaces 2016;8:13707–13. https://doi.org/10.1021/acsami.6b02271.

[348] Yang X-J, Zhang K, Zhang T-T, Xu J-J, Chen H-Y. Reliable Förster resonance energy transfer probe based on structure-switching DNA for ratiometric sensing of telomerase in living cells. Anal Chem 2017;89:4216–22. https://doi.org/10.1021/acs.analchem.7b00267.

[349] Chen C, Wei M, Liu Y, Xu E, Wei W, Zhang Y, et al. Visual and fluorometric determination of telomerase activity by using a cationic conjugated polymer and fluorescence resonance energy transfer. Microchimica Acta 2017;184:3453–60. https://doi.org/10.1007/s00604-017-2362-5.

[350] Gao Y, Xu J, Li B, Jin Y. PCR-free and label-free fluorescent detection of telomerase activity at single-cell level based on triple amplification. Biosens Bioelectron 2016;81:415–22. https://doi.org/10.1016/j.bios.2016.03.022.

[351] Wang D, Zhao X, Wei Y, Xue W, Xu Z. A pH-responsive colorimetric detection of human telomerase RNA based on a three-dimensional DNA amplifier. Anal Chim Acta 2020;1111:67–74. https://doi.org/10.1016/j.aca.2020.03.049.

[352] Qu F, Chen Z, You J, Song C. A colorimetric platform for sensitively differentiating telomere DNA with different lengths, monitoring G-quadruplex and dsDNA based on silver nanoclusters and unmodified gold nanoparticles. Spectrochim Acta A Mol Biomol Spectrosc 2018;196:148–54. https://doi.org/10.1016/j.saa.2018.02.024.

[353] Cheng X-R, Wang F, Liu C, Li J, Shan C, Wang K, et al. Sensitive naked-eye detection of telomerase activity based on exponential amplification reaction and lateral flow assay. Anal Bioanal Chem 2022;414:6139–47. https://doi.org/10.1007/s00216-022-04179-0.

[354] He J-L, Tang L, Liao S-Q, Guo M-T, Wu L, Song Y, et al. Label-free palindromic DNA nanospheres as naked-eye colorimetric assay platform for detection of telomerase activity. Talanta 2023;253:123990. https://doi.org/10.1016/j.talanta.2022.123990.

[355] Cheng M, Xiong E, Tian T, Zhu D, Ju H, Zhou X. A CRISPR-driven colorimetric code platform for highly accurate telomerase activity assay. Biosens Bioelectron 2021;172:112749. https://doi.org/10.1016/j.bios.2020.112749.

[356] Huang R, Wang M, Chen X, Yu N, Jiang C. Gold nanoparticle based colorimetric assay of telomerase activity using the cyclic strand displacement reaction. New Journal of Chemistry 2021;45:5322–6. https://doi.org/10.1039/d1nj00036e.

[357] Mahmoudi T, Pirpour Tazehkand A, Pourhassan-Moghaddam M, Alizadeh-Ghodsi M, Ding L, Baradaran B, et al. PCR-free paper-based nanobiosensing platform for visual detection of telomerase activity via gold enhancement. Microchemical Journal 2020;154:104594. https://doi.org/10.1016/j.microc.2020.104594.

[358] Xu S, Jiang L, Nie Y, Wang J, Li H, Liu Y, et al. Gold nanobipyramids as dual-functional substrates for in situ "turn on" analyzing intracellular telomerase activity based on target-triggered plasmon-enhanced fluorescence. ACS Appl Mater Interfaces 2018;10:26851–8. https://doi.org/10.1021/acsami.8b05447.

[359] Wang D, Guo R, Wei Y, Zhang Y, Zhao X, Xu Z. Sensitive multicolor visual detection of telomerase activity based on catalytic hairpin assembly and etching of Au nanorods. Biosens Bioelectron 2018;122:247–53. https://doi.org/10.1016/j.bios.2018.09.064.

[360] Yu T, Zhao W, Xu J-J, Chen H-Y. A PCR-free colorimetric strategy for visualized assay of telomerase activity. Talanta 2018;178:594–9. https://doi.org/10.1016/j.talanta.2017.09.070.

[361] Wang Y, Yang L, Wang Y, Liu W, Li B, Jin Y. An ultra-sensitive colorimetric assay for reliable visual detection of telomerase activity. Analyst 2017;142:3235–40. https://doi.org/10.1039/c7an00950j.

[362] Xu X, Wei M, Liu Y, Liu X, Wei W, Zhang Y, et al. A simple, fast, label-free colorimetric method for detection of telomerase activity in urine by using hemin-graphene conjugates. Biosens Bioelectron 2017;87:600–6. https://doi.org/10.1016/j.bios.2016.09.005.

[363] Zhang L, Zhang S, Pan W, Liang Q, Song X. Exonuclease I manipulating primer-modified gold nanoparticles for colorimetric telomerase activity assay. Biosens Bioelectron 2016;77:144–8. https://doi.org/10.1016/j.bios.2015.08.045.

[364] Wu S, Li D, Gao Z, Wang J. Controlled etching of gold nanorods by the Au(III)-CTAB complex, and its application to semi-quantitative visual determination of organophosphorus pesticides. Microchimica Acta 2017;184:4383–91. https://doi.org/10.1007/s00604-017-2468-9.

[365] Pamies R, Cifre JGH, Espín VF, Collado-González M, Baños FGD, de la Torre JG. Aggregation behaviour of gold nanoparticles in saline aqueous media. Journal of Nanoparticle Research 2014;16:2376. https://doi.org/10.1007/s11051-014-2376-4.

[366] Kanjanawarut R, Yuan B, XiaoDi S. UV-Vis spectroscopy and dynamic light scattering study of gold nanorods aggregation. Nucleic Acid Ther 2013;23:273–80. https://doi.org/10.1089/nat.2013.0421.

[367] Liu H, Pierre-Pierre N, Huo Q. Dynamic light scattering for gold nanorod size characterization and study of nanorod-protein interactions. Gold Bull 2012;45:187–95. https://doi.org/10.1007/S13404-012-0067-4.

[368] Khlebtsov BN, Khlebtsov NG. On the measurement of gold nanoparticle sizes by the dynamic light scattering method. Colloid Journal 2011;73:118–27. https://doi.org/10.1134/s1061933x11010078.

[369] He J, Unser S, Bruzas I, Cary R, Shi Z, Mehra R, et al. The facile removal of CTAB from the surface of gold nanorods. Colloids Surf B Biointerfaces 2018;163:140–5. https://doi.org/10.1016/j.colsurfb.2017.12.019.

[370] Mergny J, Lacroix L. UV melting of G-Quadruplexes. Curr Protoc Nucleic Acid Chem 2009;37. https://doi.org/10.1002/0471142700.nc1701s37.

[371] Jana J, Weisz K. Thermodynamic stability of G-Quadruplexes: Impact of sequence and environment. ChemBioChem 2021;22:2848–56. https://doi.org/10.1002/cbic.202100127.

[372] Murat P, Balasubramanian S. Existence and consequences of G-quadruplex structures in DNA. Curr Opin Genet Dev 2014;25:22–9. https://doi.org/10.1016/j.gde.2013.10.012.

[373] Yan Y-Y, Tan J-H, Lu Y-J, Yan S-C, Wong K-Y, Li D, et al. G-Quadruplex conformational change driven by pH variation with potential application as a nanoswitch. Biochimica et Biophysica Acta (BBA) - General Subjects 2013;1830:4935–42. https://doi.org/10.1016/j.bbagen.2013.06.019.

[374] Nishio M, Tsukakoshi K, Ikebukuro K. G-quadruplex: Flexible conformational changes by cations, pH, crowding and its applications to biosensing. Biosens Bioelectron 2021;178:113030. https://doi.org/10.1016/j.bios.2021.113030.

[375] Ho MC, Chang CW. Cationic and anionic reverse micelles as the molecular crowding container for G-quadruplex structure. RSC Adv 2014;4:20531–4. https://doi.org/10.1039/c4ra02141j.

[376] Ma Y, Iida K, Nagasawa K. Topologies of G-quadruplex: Biological functions and regulation by ligands. Biochem Biophys Res Commun 2020;531:3–17. https://doi.org/10.1016/j.bbrc.2019.12.103.

[377] del Villar-Guerra R, Trent JO, Chaires JB. G-Quadruplex Secondary structure obtained from circular dichroism spectroscopy. Angewandte Chemie International Edition 2018;57:7171–5. https://doi.org/10.1002/anie.201709184.

[378] Lee JA, DeRosa MC. A pH-driven DNA switch based on the A+ ·G mispair. Chem Commun 2010;46:418–20. https://doi.org/10.1039/B918725A.

[379] Verdolino V, Cammi R, Munk BH, Schlegel HB. Calculation of pKa values of nucleobases and the guanine oxidation products guanidinohydantoin and

spiroiminodihydantoin using density functional theory and a polarizable continuum model. J Phys Chem B 2008;112:16860–73. https://doi.org/10.1021/jp8068877.

[380] Wei D, Parkinson GN, Reszka AP, Neidle S. Crystal structure of a c-kit promoter quadruplex reveals the structural role of metal ions and water molecules in maintaining loop conformation. Nucleic Acids Res 2012;40:4691–700. https://doi.org/10.1093/nar/gks023.

[381] Hamon C, Bizien T, Artzner F, Even-Hernandez P, Marchi V. Replacement of CTAB with peptidic ligands at the surface of gold nanorods and their self-assembling properties. J Colloid Interface Sci 2014;424:90–7. https://doi.org/10.1016/j.jcis.2014.03.002.

[382] Rostro-Kohanloo BC, Bickford LR, Payne CM, Day ES, Anderson LJE, Zhong M, et al. The stabilization and targeting of surfactant-synthesized gold nanorods. Nanotechnology 2009;20:434005. https://doi.org/10.1088/0957-4484/20/43/434005.

[383] Khani H, Abbasi S, Tavakkoli Yaraki M, Gholivand MB. Colorimetric detection and determination of glutathione based on superoxide radical-assisted etching approach. Microchemical Journal 2022;173:107006. https://doi.org/10.1016/j.microc.2021.107006.

[384] Sharma A, Jampani VSR, Lagerwall JPF. Realignment of liquid crystal shells driven by temperature-dependent surfactant solubility. Langmuir 2019;35:11132–40. https://doi.org/10.1021/acs.langmuir.9b00989.

[385] Novoseltseva AA, Ivanov NM, Novikov RA, Tkachev Y V., Bunin DA, Gambaryan AS, et al. Structural and functional aspects of G-Quadruplex aptamers which bind a broad range of influenza A viruses. Biomolecules 2020;10:119. https://doi.org/10.3390/biom10010119.

[386] Kimura-Suda H, Petrovykh DY, Tarlov MJ, Whitman LJ. Base-dependent competitive adsorption of single-stranded DNA on gold. J Am Chem Soc 2003;125:9014–5. https://doi.org/10.1021/ja035756n.

[387] Liu J. Adsorption of DNA onto gold nanoparticles and graphene oxide: surface science and applications. Physical Chemistry Chemical Physics 2012;14:10485. https://doi.org/10.1039/c2cp41186e.

[388] ICH Topic Q 2 (R1) Validation of analytical procedures: Text and Methodology Step 5 Note For Guidance On Validation Of Analytical Procedures: Text And Methodology (Cpmp/Ich/381/95) Approval By Cpmp November 1994 Date For Coming Into Operation 1995.

[389] Shrivastava A, Gupta V. Methods for the determination of limit of detection and limit of quantitation of the analytical methods. Chronicles of Young Scientists 2011;2:21. https://doi.org/10.4103/2229-5186.79345.

[390] Li C, Xu Y, Li X, Ye Z, Yao C, Chen Q, et al. Unexpected dual action of cetyltrimethylammonium bromide (CTAB) in the self-assembly of colloidal Nanoparticles at Liquid–Liquid Interfaces. Adv Mater Interfaces 2020;7:2000391. https://doi.org/10.1002/admi.202000391.

[391] Li J, Zhu B, Zhu Z, Zhang Y, Yao X, Tu S, et al. Simple and rapid functionalization of gold nanorods with oligonucleotides using an mPEG-SH/Tween 20-assisted approach. Langmuir 2015;31:7869–76. https://doi.org/10.1021/acs.langmuir.5b01680.

[392] Sutter E, Zhang B, Sutter P. Single-strand DNA-nanorod conjugates tunable anisotropic colloids for on-demand self-assembly. J Colloid Interface Sci 2021;586:847–54. https://doi.org/10.1016/j.jcis.2020.11.009.

[393] Das U, Sahoo A, Haldar S, Bhattacharya S, Mandal SS, Gmeiner WH, et al. Secondary structure-dependent physicochemical interaction of oligonucleotides with gold nanorod and photothermal effect for future applications: A new insight. ACS Omega 2018;3:14349–60. https://doi.org/10.1021/acsomega.8b00969.

[394] Brown KA, Park S, Hamad-Schifferli K. Nucleotide−surface interactions in DNA-modified Au−nanoparticle conjugates: Sequence effects on reactivity and hybridization. The Journal of Physical Chemistry C 2008;112:7517–21. https://doi.org/10.1021/jp711869p.

[395] Hurst SJ, Lytton-Jean AKR, Mirkin CA. Maximizing DNA loading on a range of gold nanoparticle sizes. Anal Chem 2006;78:8313–8. https://doi.org/10.1021/ac0613582.

[396] Parak WJ, Pellegrino T, Micheel CM, Gerion D, Williams SC, Alivisatos AP. Conformation of oligonucleotides attached to gold nanocrystals probed by gel electrophoresis. Nano Lett 2003;3:33–6. https://doi.org/10.1021/nl025888z.

[397] Peng B, Liu Z, Jiang Y. Aggregation of DNA-grafted nanoparticles in water: The critical role of sequence-dependent conformation of DNA coating. J Phys Chem B 2022;126:847–57. https://doi.org/10.1021/acs.jpcb.1c09450.

[398] Athira ET, Satija J. Plasmonic nanoparticle etching-based optical sensors: Current status and future prospects. Analyst 2023;148:6188–200. https://doi.org/10.1039/d3an01244a.

[399] Steenken S, Jovanovic S V. How easily oxidizable is DNA? One-electron reduction potentials of adenosine and guanosine radicals in aqueous solution. J Am Chem Soc 1997;119:617–8. https://doi.org/10.1021/ja962255b.

APPENDICIES

A. Reduction Reactions of Gold

A1. Reaction of Seed Solution

$$HAuCl_4 + NaBH_4 \rightarrow Au + BH_4 + HCl + NaCl_3 \quad (Eq.\,A1)$$

A2. Reactions of Growth Solution

Where H_2A is ascorbic acid, $HA\cdot$ is ascorbic acid radical, and A is dehydroascorbic acid.

$$CTA^+ + AuCl_4^- \rightarrow AuCl_4 - CTA \quad (Eq.\,A2)$$

$$H_2A + AuCl_4 - CTA \rightarrow HA\cdot + AuCl_3 - CTA + HCl \quad (Eq.\,A3)$$

$$HA\cdot + AuCl_3 - CTA \rightarrow A + AuCl_2 - CTA + HCl \quad (Eq.\,A4)$$

$$AuCl_2 - CTA + H_2A \rightarrow Au^0 + HA\cdot + HCl + CTACl \quad (Eq.\,A5)$$

B. DLS Experiment Analyses

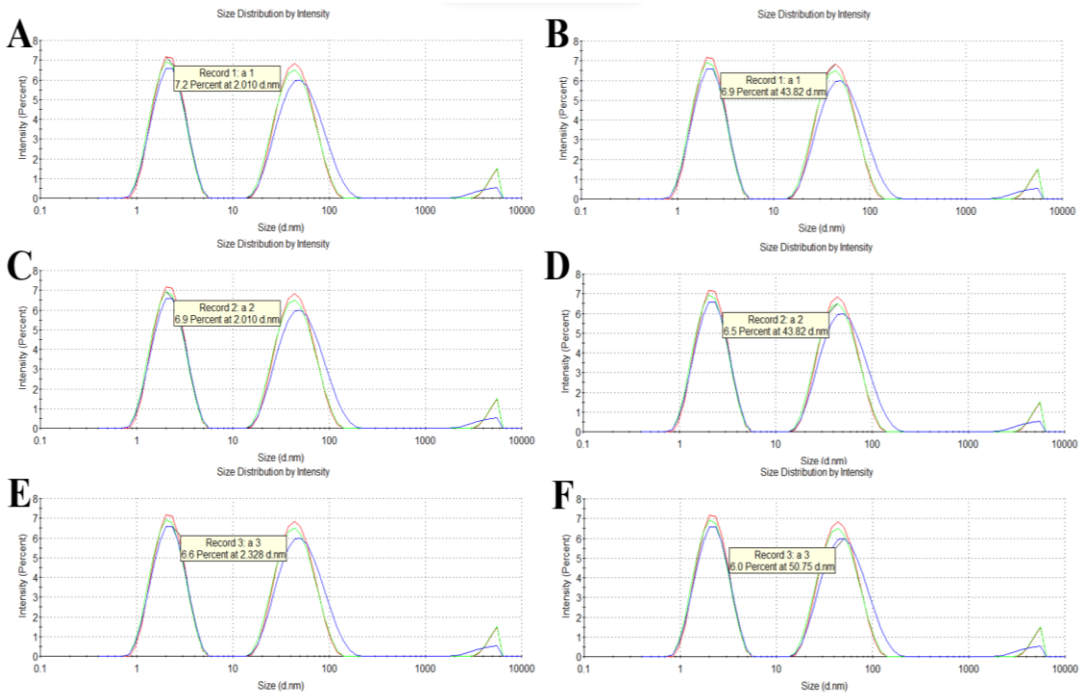


Figure B 1. Size distribution of GNRs by intensity. (Same sample recorded 3 times .) A: the first peak of Record 1, B: the second peak of Record 2, C: the first peak of Record 2, D: the second peak of Record 2, E: the first peak of Record 3, F: the second peak of Record 3.

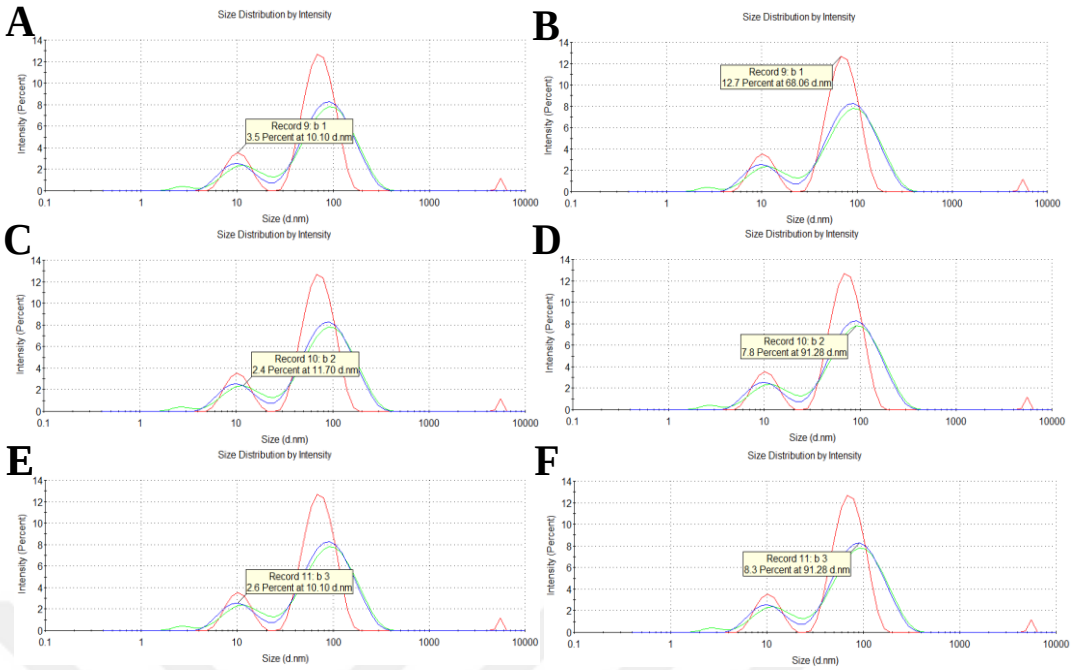


Figure B 2. Size distribution of GNRs by intensity after 6 min incubation under optimized conditions. (Same sample recorded 3 times.) A: the first peak of Record 1, B: the second peak of Record 2, C: the first peak of Record 2, D: the second peak of Record 2, E: the first peak of Record 3, F: the second peak of Record 3.

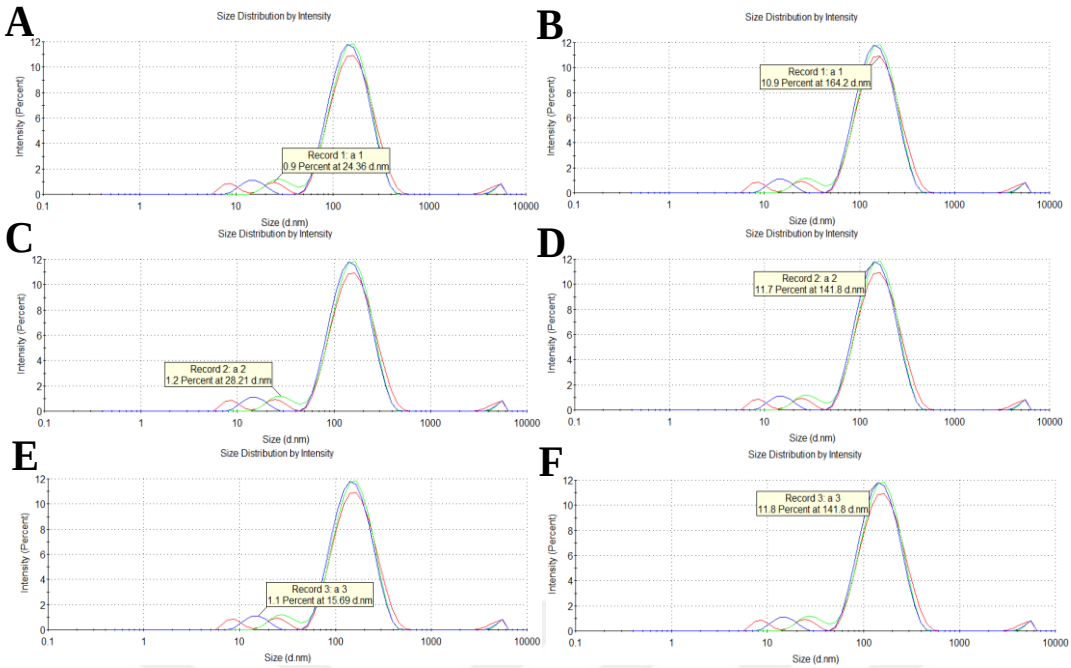


Figure B 3. Size distribution of GNRs by intensity after 10 min incubation under optimized conditions. (Same sample recorded 3 times.) A: the first peak of Record 1, B: the second peak of Record 2, C: the first peak of Record 2, D: the second peak of Record 2, E: the first peak of Record 3, F: the second peak of Record 3.

Table B 1. Size distribution of GNRs by intensity of 0 min, 6 min and 10 min of incubation under optimized conditions.

	Peak 1	**Peak 2**	**Peak 1 Average**	**Peak 1 RSD**	**Peak 2 Average**	**Peak 2 RSD**
0 min-1	2.01	42.82	2.12	0.18	46.13	4.00
0 min-2	2.01	43.82				
0 min-3	2.33	50.75				
6 min-1	10.10	68.06	10.63	0.92	83.54	13.41
6 min-2	11.70	91.28				
6 min-3	10.10	91.28				
10 min-1	24.36	164.20	22.75	6.41	156.73	12.93
10 min-2	28.21	164.20				
10 min-3	15.69	141.80				

C. Thermal Denaturation Studies

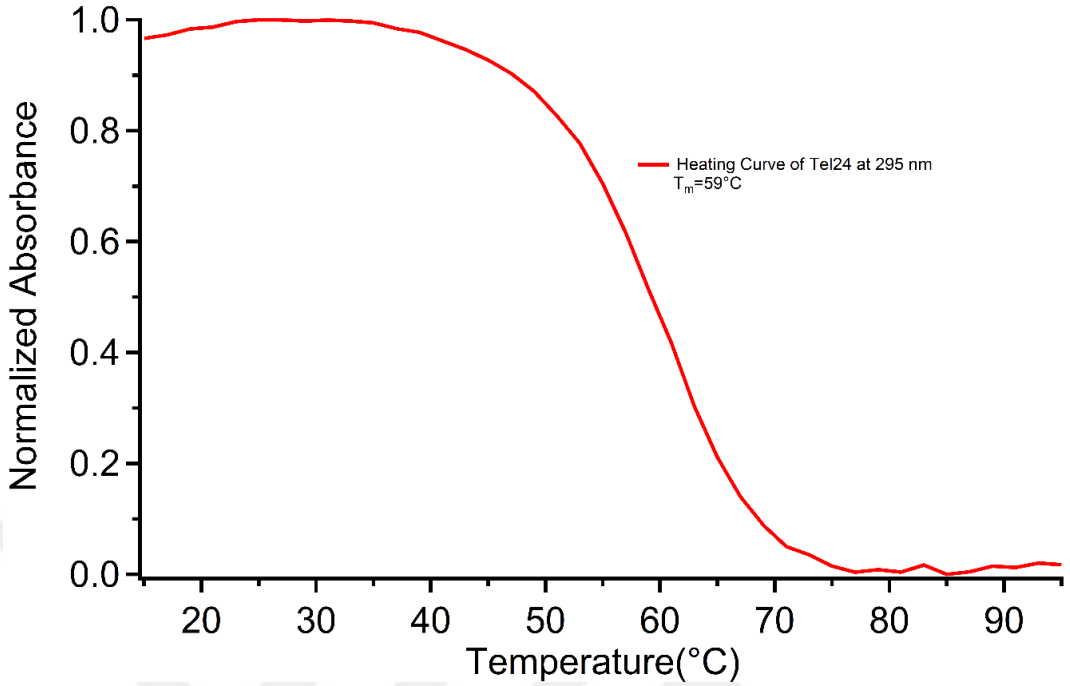


Figure C 1. UV-Vis thermal denaturation profile of 2.0 µM of Tel24.

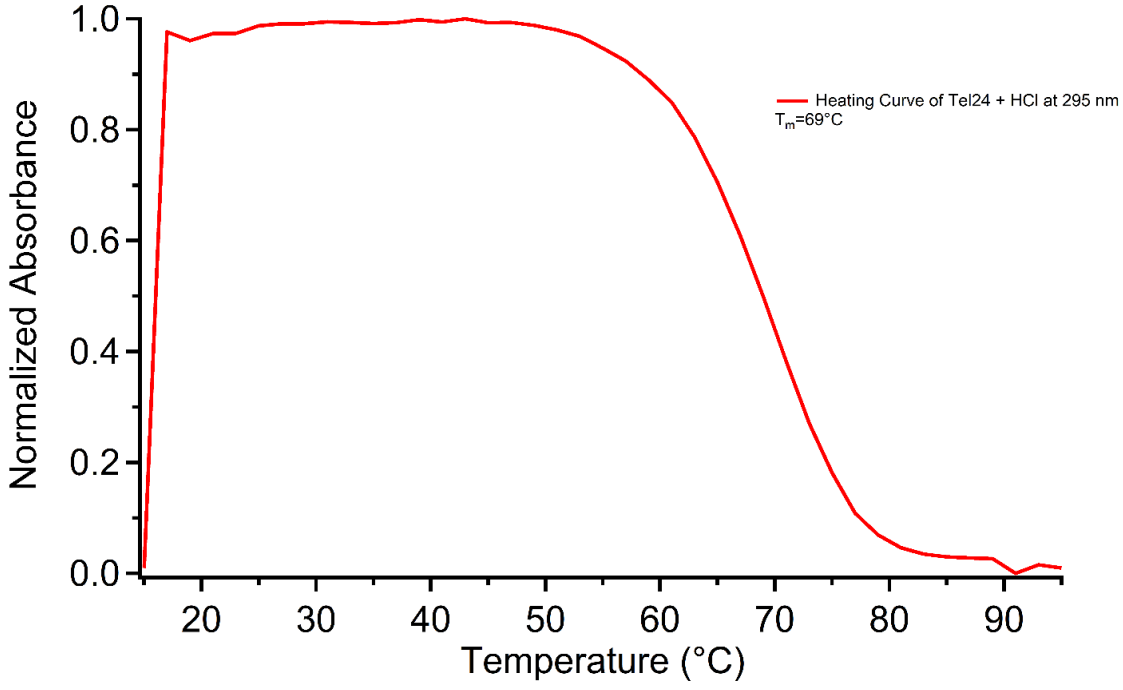


Figure C 2. UV-Vis thermal denaturation profile of 2.0 µM of Tel24 in the presence of 28 mM HCl.

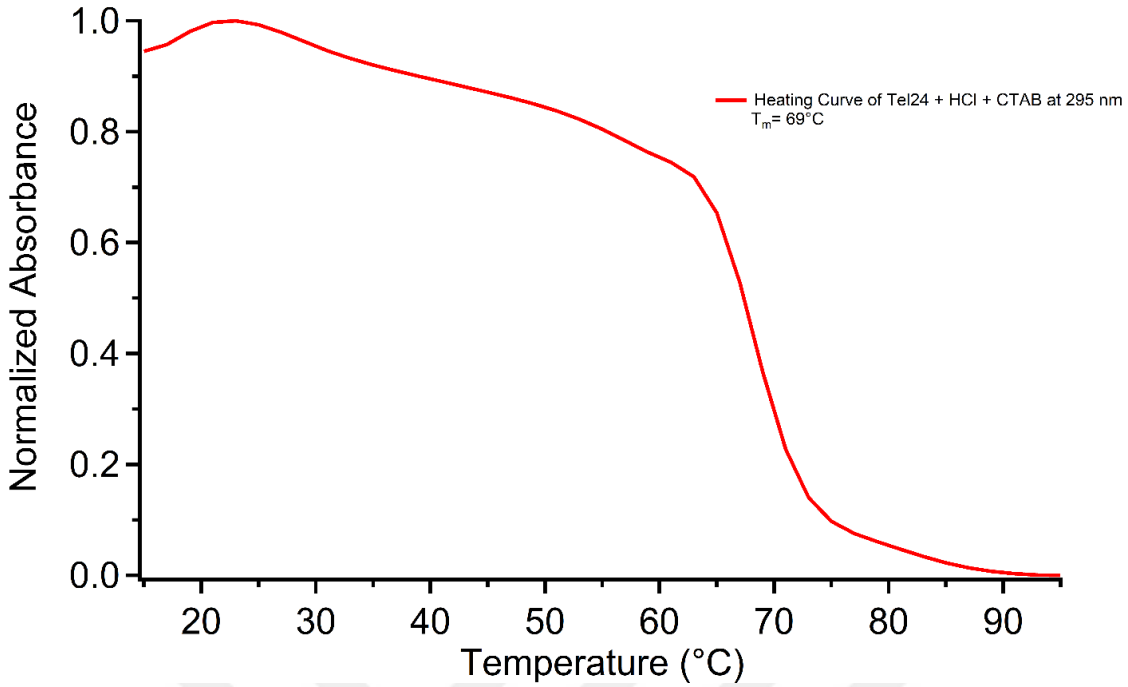


Figure C 3. UV-Vis thermal denaturation profile of 2.0 μM of Tel24 in the presence of 28 mM HCl and 0.01 M CTAB.

Table C 1. Melting temperatures of Tel24, Tel24+HCl and Tel24+HCl+CTAB.

Sample	**Melting Temperature (°C)**
Tel24	59
Tel24+HCl	69
Tel24+HCl+CTAB	69

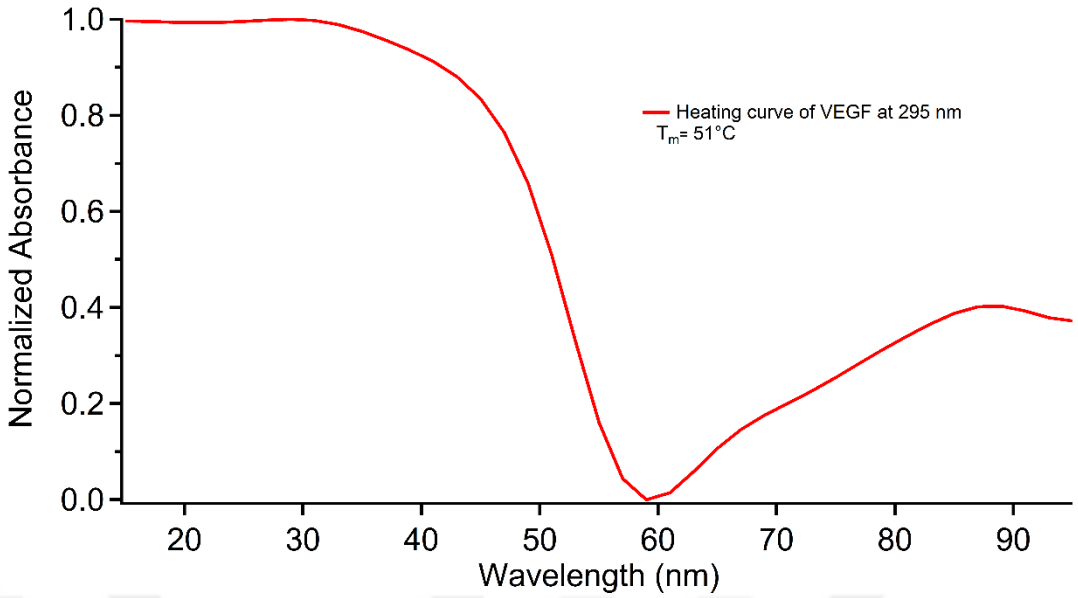


Figure C 4. UV-Vis thermal denaturation profile of 2.0 µM of VEGF.

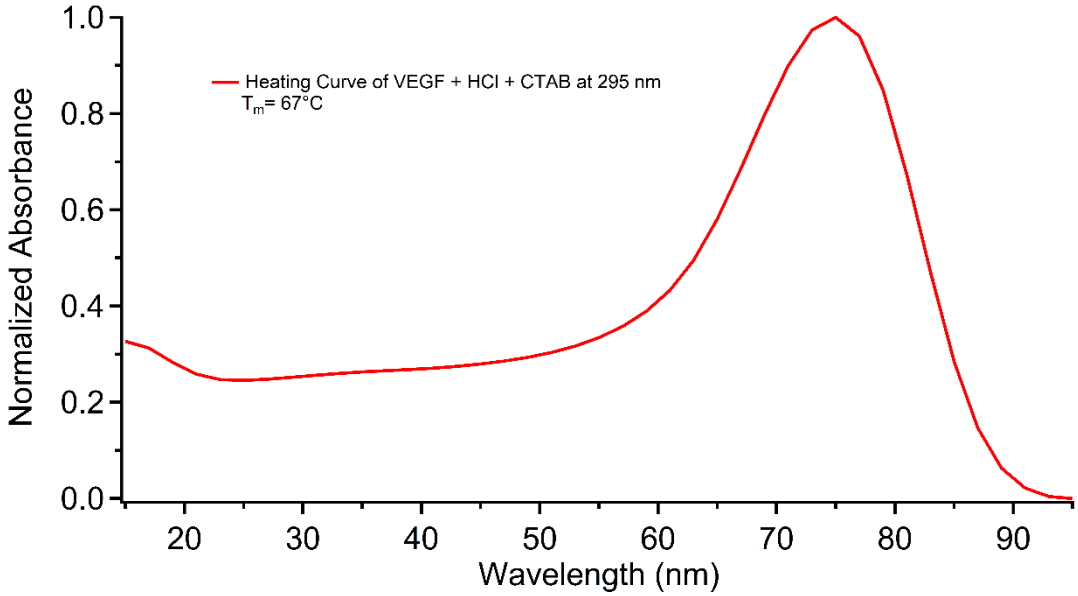


Figure C 5. UV-Vis thermal denaturation profile of 2.0 µM of VEGF in the presence of 28 mM HCl and 0.01 M CTAB.

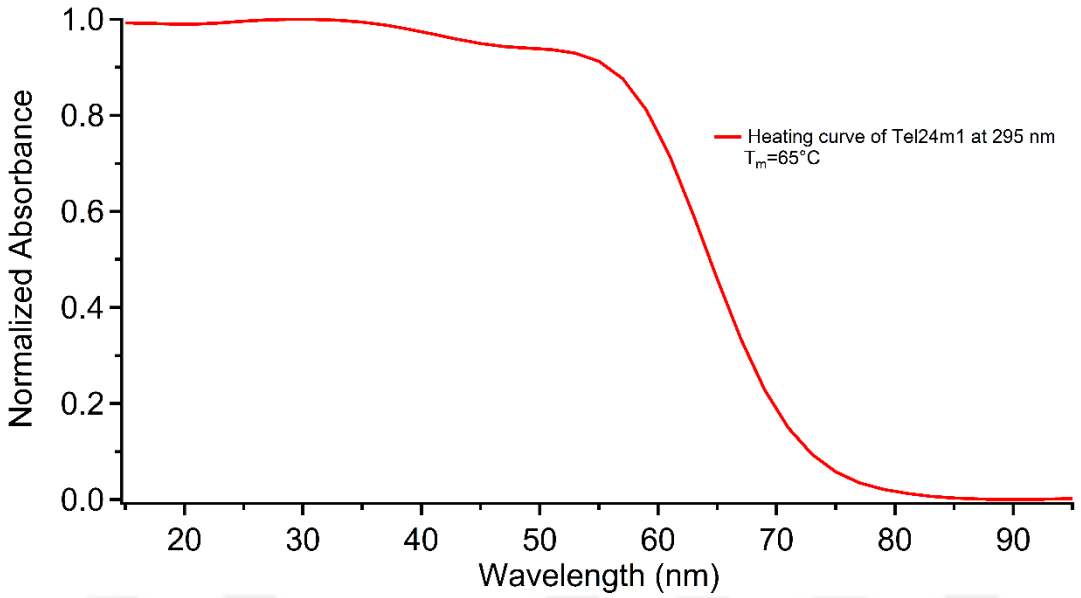


Figure C 6. UV-Vis thermal denaturation profile of 2.0 µM of Tel24m1.

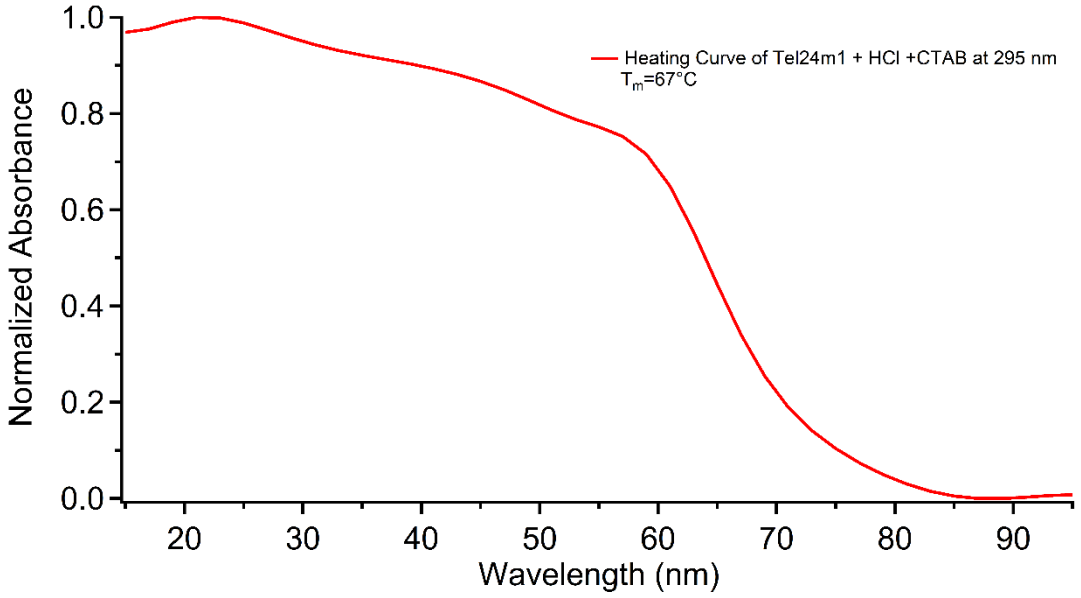


Figure C 7. UV-Vis thermal denaturation profile of 2.0 µM of Tel24m1 in the presence of 28 mM HCl and 0.01 M CTAB.

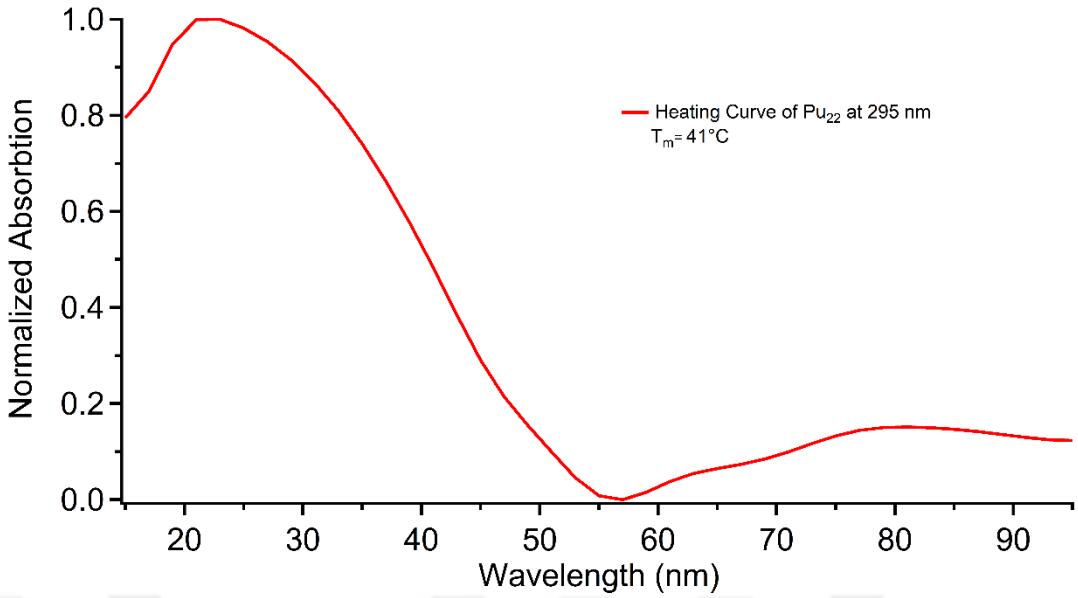


Figure C 8. UV-Vis thermal denaturation profile of 2.0 μM of Pu_{22}.

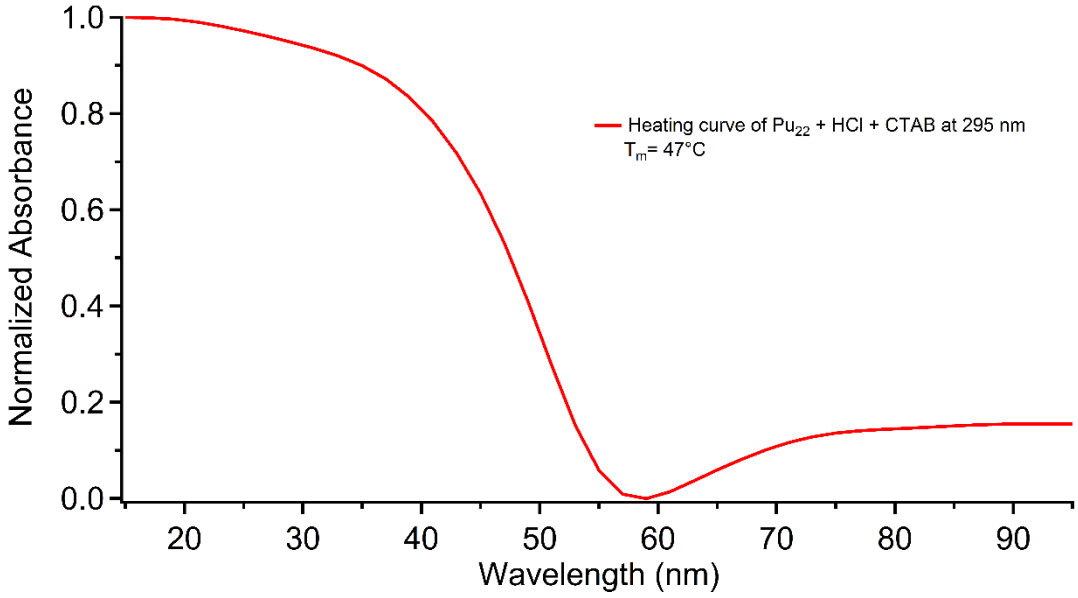


Figure C 9. UV-Vis thermal denaturation profile of 2.0 μM of Pu_{22} in the presence of 28 mM HCl and 0.01 M CTAB.

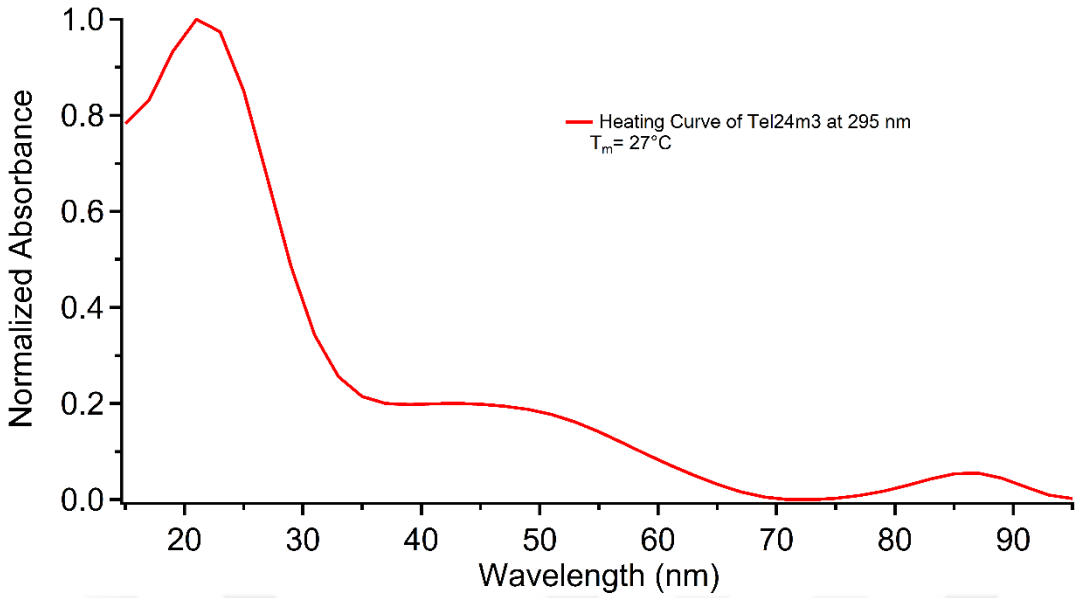


Figure C 10. UV-Vis thermal denaturation profile of 2.0 µM of Tel24m1.

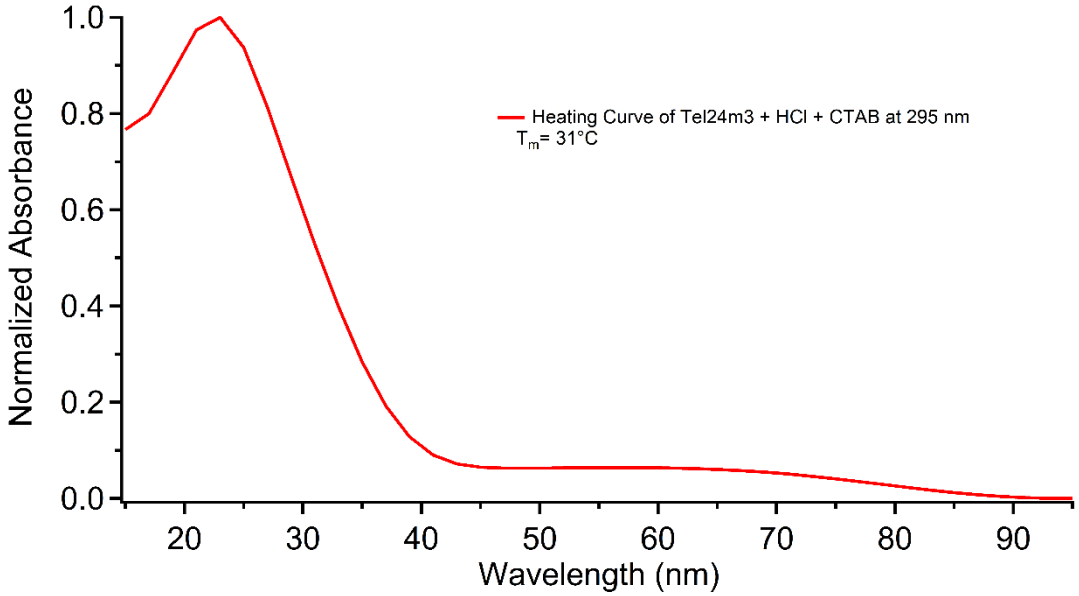


Figure C 11. UV-Vis thermal denaturation profile of 2.0 µM of Tel24m3 in the presence of 28 mM HCl and 0.01 M CTAB.

D. Circular Dichroism Studies

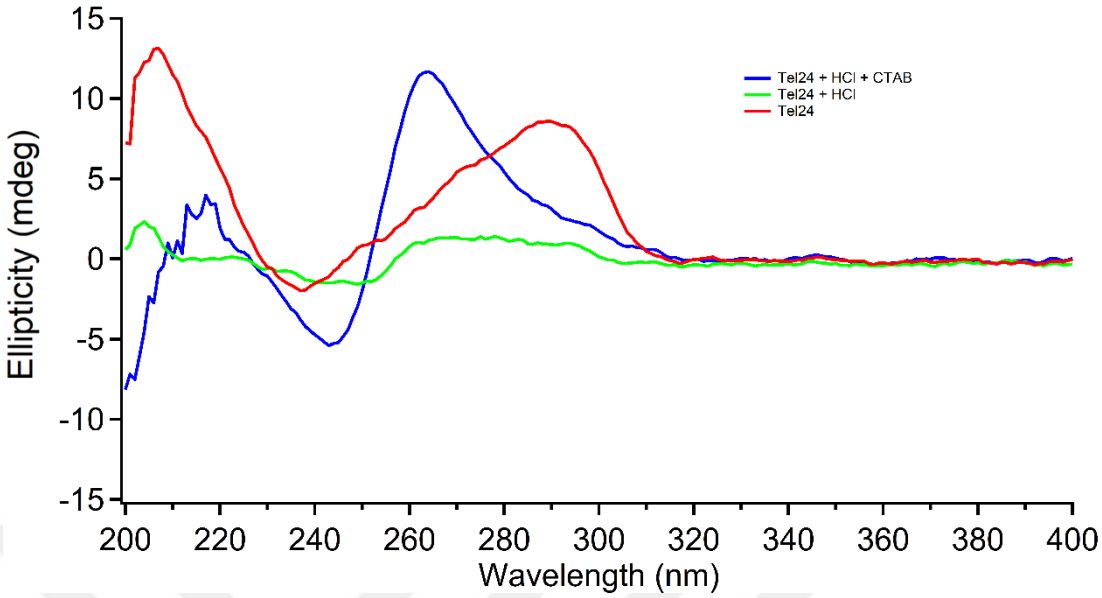


Figure D 1. CD spectra of Tel24, Tel24 + HCl and Tel24 + HCl + CTAB. Experimental conditions: [Tel24]=2.0 μM, [HCl]=28 mM, [CTAB]=0.01 M.

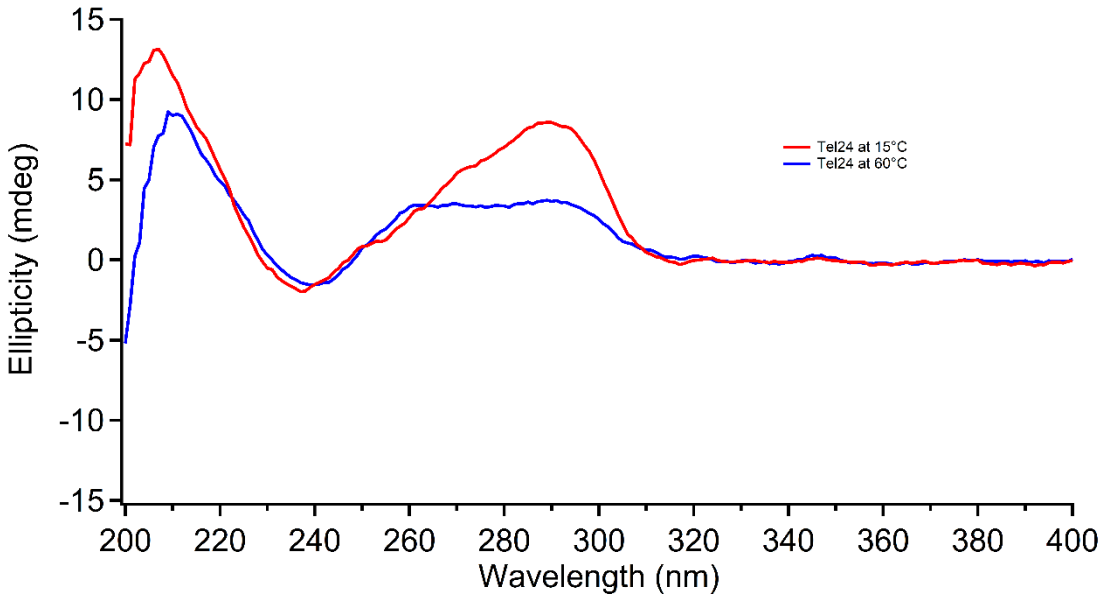


Figure D 2. CD spectra of Tel24 at 15°C, 60°C and 80°C.

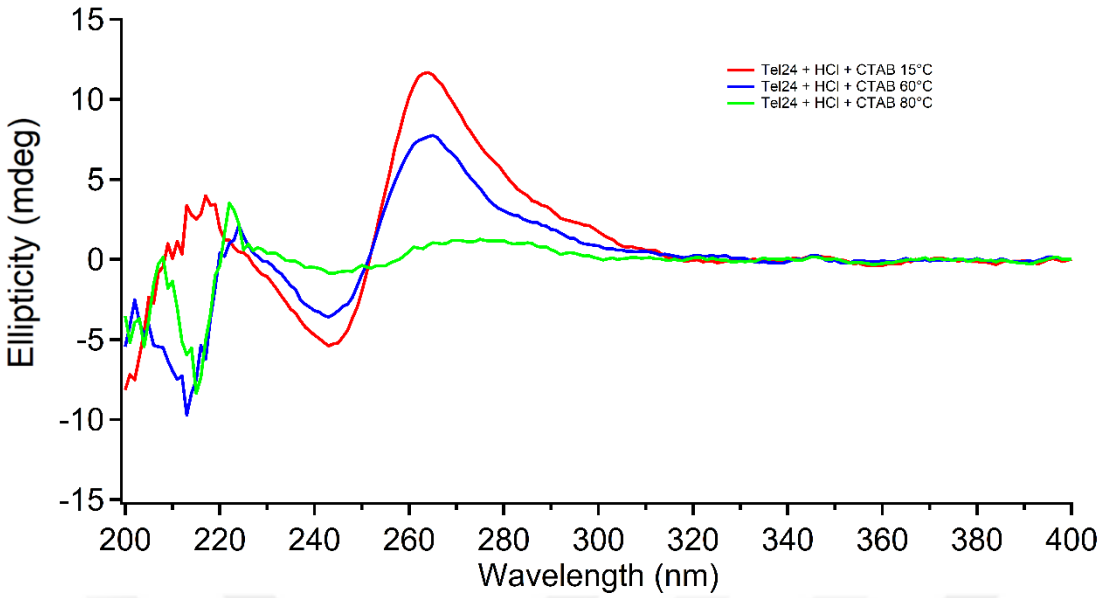


Figure D 3. CD spectra of 2 μM Tel24 in the presence of HCl and CTAB at 15°C, 60°C and 80°C. Experimental conditions: [Tel24]=2.0 μM, [HCl]=28 mM, [CTAB]=0.01 M.

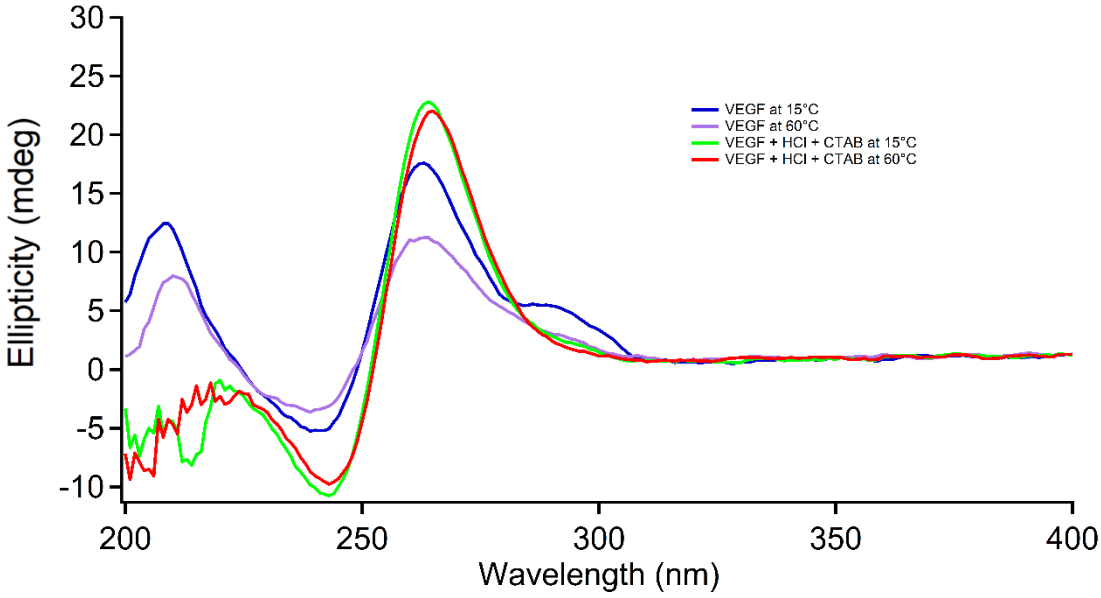


Figure D 4. CD spectra of VEGF, VEGF + HCl and VEGF + HCl + CTAB. Experimental conditions: [VEGF]=2.0 μM, [HCl]=28 mM, [CTAB]=0.01 M.

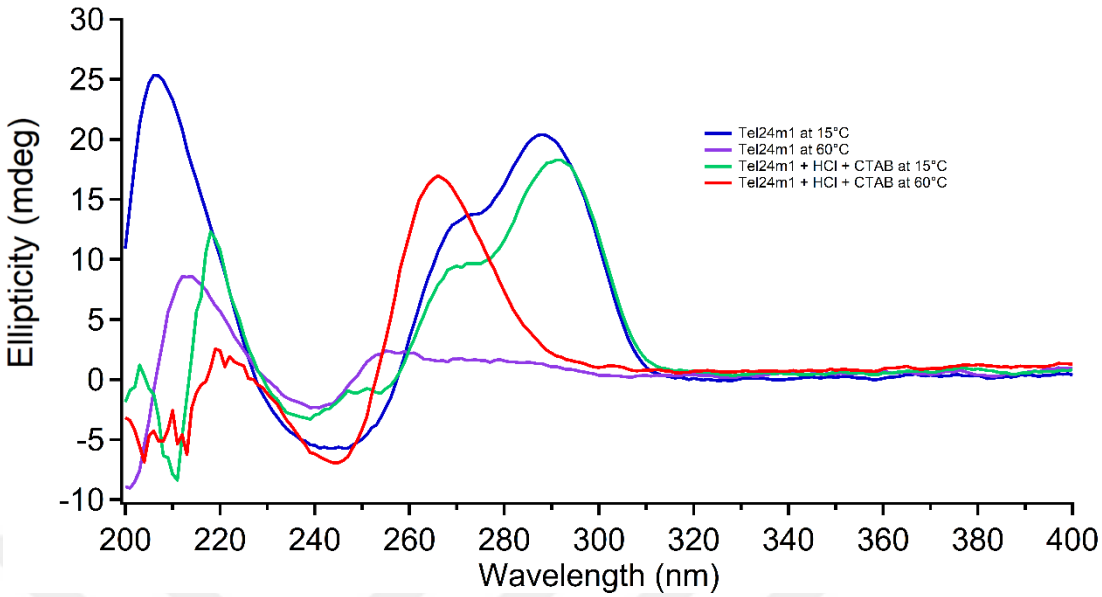


Figure D 5. CD spectra of Tel24m1, Tel24m1 + HCl and Tel24m1 + HCl + CTAB. Experimental conditions: [Tel24m1]=2.0 μM, [HCl]=28 mM, [CTAB]=0.01 M and Measurement temperature=15°C.

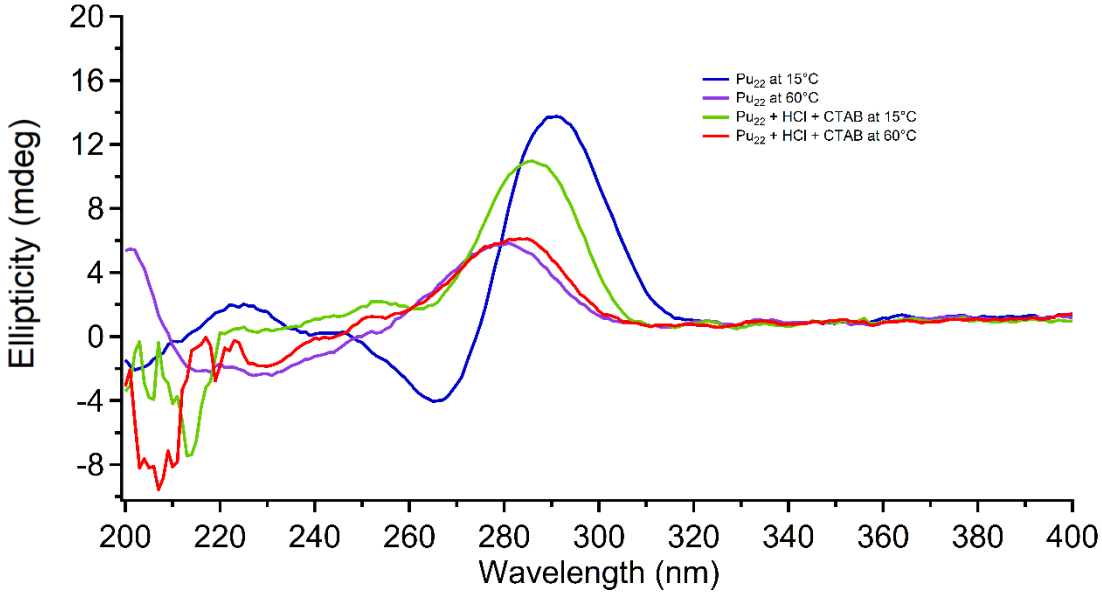


Figure D 6. CD spectra of Pu_{22}, Pu_{22} + HCl and Pu_{22} + HCl + CTAB. Experimental conditions: [Pu_{22}]=2.0 μM, [HCl]=28 mM, [CTAB]=0.01 M and Measurement temperature=15°C.

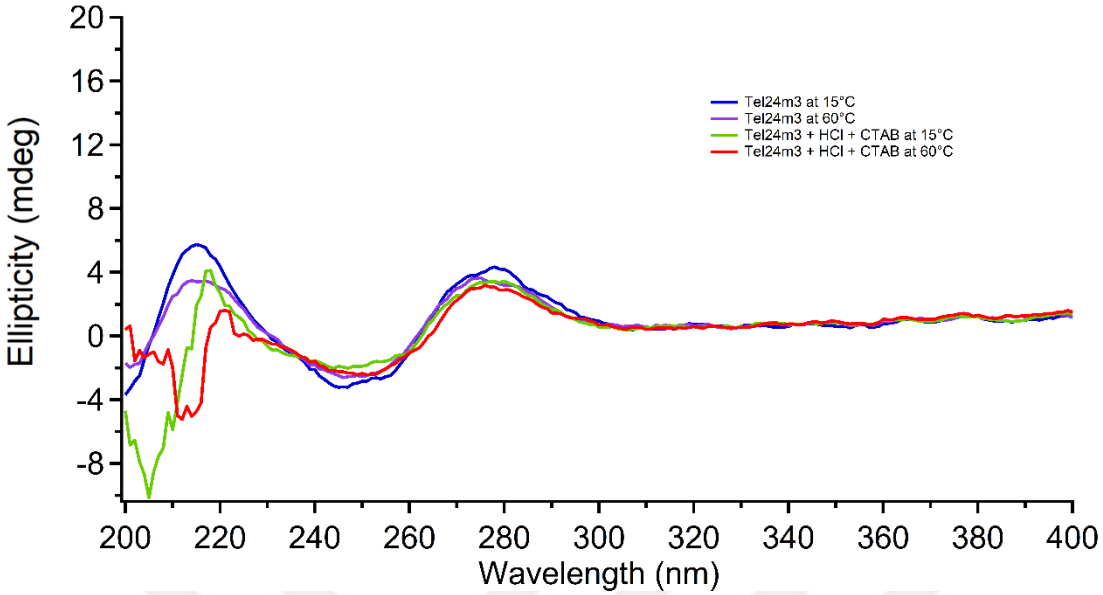


Figure D 7. CD spectra of Tel24m3, Tel24m3 + HCl and Tel24m3 + HCl + CTAB. Experimental conditions: [Tel24m3]=2.0 µM, [HCl]=28 mM, [CTAB]=0.01 M and Measurement temperature=15°C.

E. UV-Vis Spectra

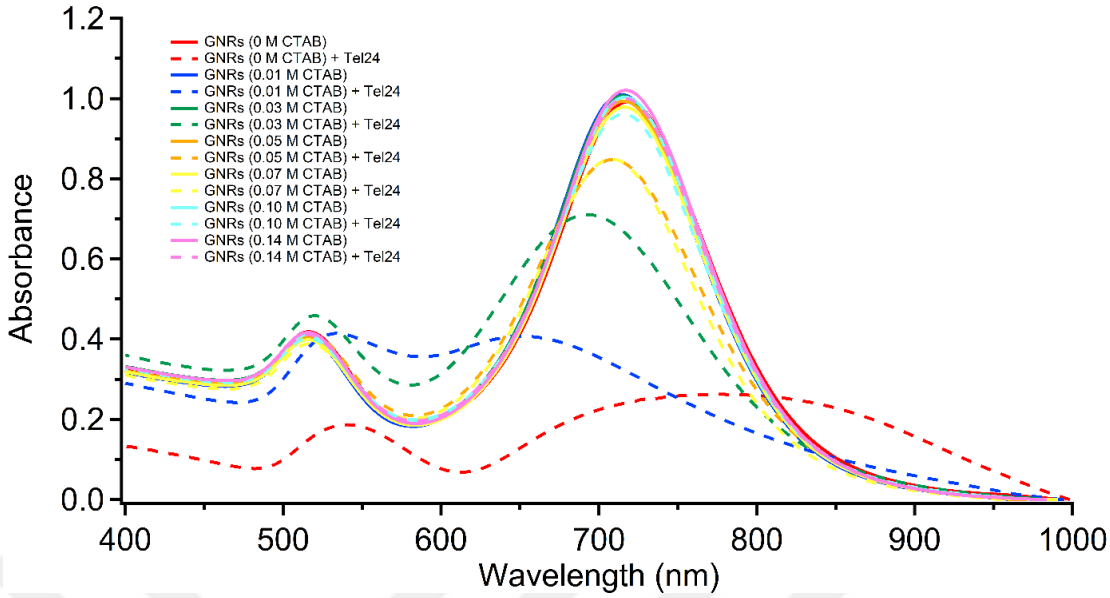


Figure E 1. UV-Vis absorption spectra of the GNRs upon the addition of Tel24 with different concentrations of CTAB (0 – 0.14 M). Experimental conditions: [HCl]=28 mM, [Tel24]=0.64 µM, Temperature: 60°C, after 10 min of mixing.

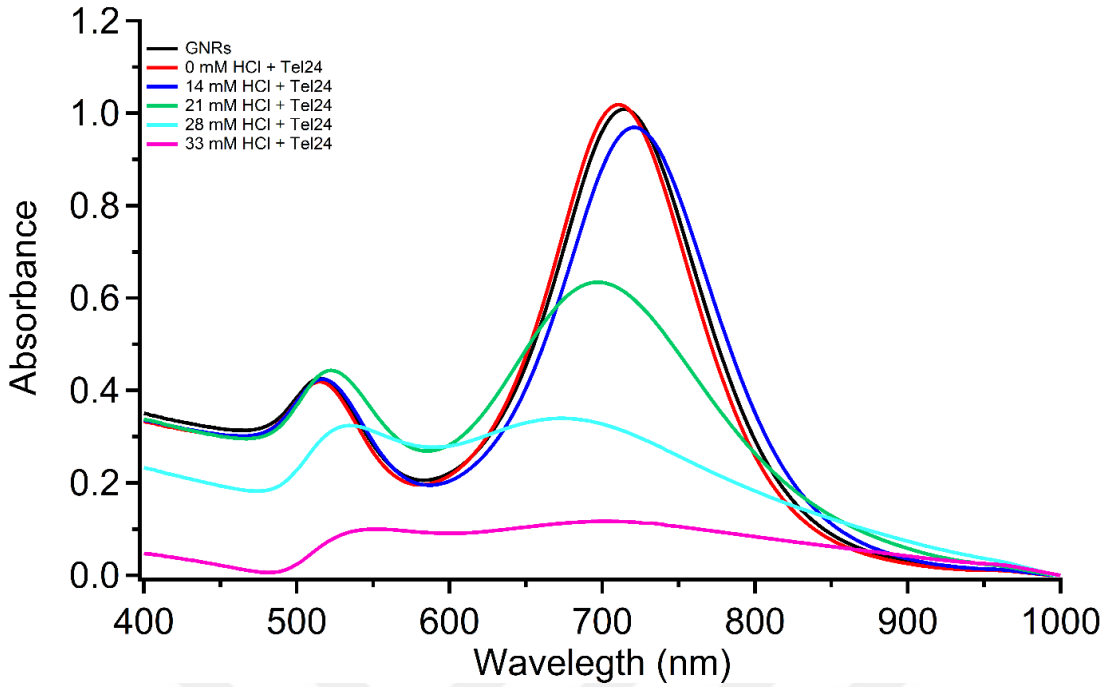


Figure E 2. UV-Vis absorption spectra of the GNRs upon the addition of Tel24 with different concentrations of HCl (0 – 33 mM). Experimental conditions: [CTAB]=0.01 M, [Tel24]=0.64 µM, Temperature: 60°C, after 10 min of mixing.

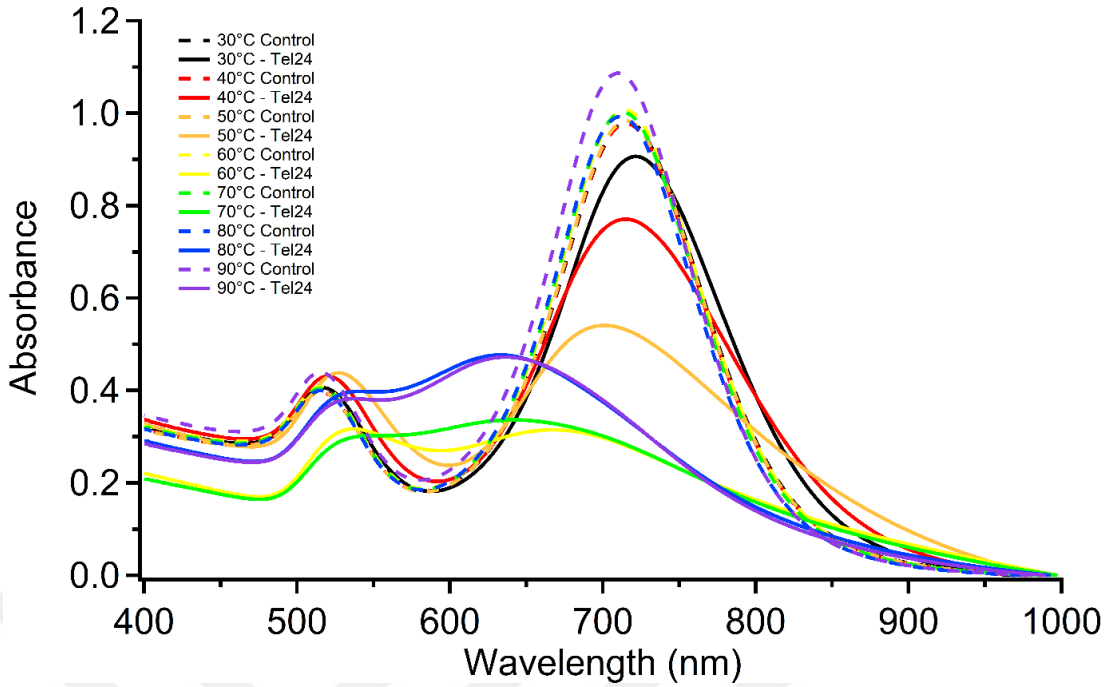


Figure E 3. UV-Vis absorption spectra of the GNRs upon the addition of Tel24 at different temperatures (30.0-80.0°C) Experimental conditions: [Tel24]=0.64 μM, after 10 min.

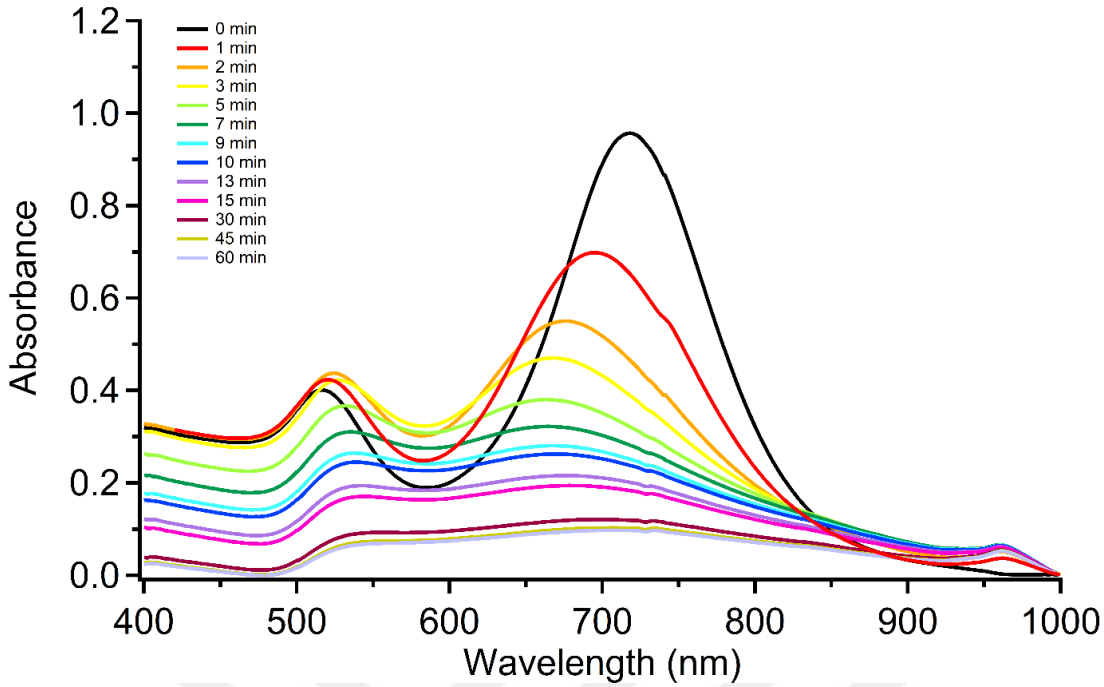


Figure E 4. UV-Vis absorption spectra of the GNRs upon the addition of the target analyte for 0-60 min. Experimental conditions: [CTAB]=0.01 M, [HCl]=28 mM, [Tel24]=0.64 μM, Temperature: 60°C.